# DURABILITY OF WET-BOND BETWEEN HYBRID FRP LAMINATE AND CAST-IN-PLACE CONCRETE

by

**Li Li**

October 2007

**Department of Civil Engineering and Applied Mechanics**
**McGill University, Montreal, Canada**

A thesis submitted to the Faculty of Graduate and Postdoctoral Studies and Research
in partial fulfillment of the requirements of the degree of
**Master of Engineering**

# Abstract

Wet-bond of hybrid carbon and glass fibre reinforced polymer (FRP) composites to cast-in-place concrete has been developed for a steel-free reinforced concrete structure. The prefabricated FRP is to serve as both stay-in-place form and external reinforcement, and the carbon and glass hybrid to provide suitable ductility in reinforcement. FRP formwork and cast-in-place concrete are connected through a fresh epoxy resin for a composite action. Since the new structure is solely dependent on the bond between FRP and concrete, a durable bond is of paramount importance. The purpose of this study is to examine the durability of wet-bond in comparison with dry-bond, which employs hardened concrete as substrate to evaluate their bond strength, bond mechanism and durability capacity. It was found that carbon-glass hybrid made significant contribution to ductility of composite materials. The curing of epoxy in the presence of fresh concrete had no negative effect on degree of curing (DOC) and glass transition temperature (Tg) of epoxy. The moisture in concrete, however, introduced water bubbles at epoxy surface that made the adhesive interface more porous and was responsible for relatively weak adhesion between epoxy and concrete in wet-bond samples. Bond strength of wet-bond is largely dependent on the mechanical interlock between the adhesive and aggregates. Of the varied environmental exposures: freeze-thaw cycling, continuous low temperature, wet-dry cycling and continuous hot moist conditions, the wet-bond technology is best suited to cold climate environments. Three typical failure modes of bond between hybrid FRP and concrete were modeled and the prediction was compared with experimental results.

# Résumé

Le composites hybrides faits de polymère renforcé de fibres de verre et de carbone (PRP) peuvent être utilisés comme renforcement externe et comme coffrage permanent avec du béton sans armature interne. Le béton est coulé en place en contact avec un époxy frais. Le comportement du composite hybride et la performance de l'adhésion de l'époxy frais au béton frais sont étudiés afin d'explorer la faisabilité de cette technique. L'utilisation de PRF hybride renforcé de fibres de carbone et de fibres de verre vise à fournir une ductilité appropriée au renforcement externe, alors que l'usage d'une adhésion époxy frais et béton frais (ou adhésion humide) vise à lier le PRF et le béton pour créer une action composite. L'importance d'une adhésion durable entre le PRF et le béton est primordiale pour la viabilité de la nouvelle structure. L'objectif de cette étude est d'examiner la durabilité dune adhésion humide en comparaison avec une adhésion sèche qui utilise le béton durci comme substrat, pour évaluer pour chaque cas la force d'adhésion, les mécanismes d'adhésion, et la durabilité. On a constaté pour le composite hybride carbone-verre a une contribution significative à la ductilité du composite. La cure de l'époxy en présence du béton frais, de l'époxy n'a aucun effet sur le degré de séchage et la température de transition du verre. Cependant, l'humidité du béton a causé le développement de bulles d'eau qui ont rendu l'interface plus poreuse, causant ainsi des réiens chimiques plus faibles dans le cas d'adhésion humide. La force de adhésion humide dépend largement des imbrications mécaniques entre l'adhésif et les granulats. Considérant de exposition environnementale comme les cycles de gel-dégel, les basses températures permanentes, les cycles humidification-séchage, et les conditions climatiques chaudes et humides, la technologie des adhésion humide convient mieux aux climats froids. Trois modes typiques de défaillance de l'adhésion entre le PRF hybride et le béton ont été modélisés, et les prédictions numériques ont été comparées aux résultats expérimentaux.

# Acknowledgements

The author would like to express her gratitude to Professor Yixin Shao for his support, recommendations and his contribution of expertise in the fascinating field of the new technology in civil engineering. His invaluable guidance, time and effort throughout this project are greatly appreciated. Thanks are also extended to Professor Zhishen Wu of Ibaraki University in Japan for his guidance, support and the supply of glass and carbon fibres, and to Dr. William D. Cook for his assistance on troubleshooting of the data acquisition system. The author would like to acknowledge the help by Professor Pascal Hubert and Mr. Jonathan Laliberté of Mechanical Engineering Department for their support in conducting the epoxy experiments; by Professor Charles Manatakos for his useful comments and suggestions; by Mr. Joe Solomon of Specialty Construction Products LTD. in Winnipeg for providing the epoxy resin; by Mr. Ron Sheppard, Mr. Marek Przykorski, Mr. John Bartczak and Mr. Damon Kiperchuk for their assistance in the laboratory test setup design and modification.

The author would like to thank the office staff of the Department of Civil Engineering and Applied Mechanics at McGill University who made the completeness of this research possible.

Thanks are extended to Mr. Nabil Saliba for the French translation of the abstract.

Finally, the author would like to thank the continued support from her parents, her brother and her good friends.

# List of symbols

| | | |
|---|---|---|
| $A_{frp}$ | area of cross section of hybrid FRP laminate | $mm^2$ |
| $A_{con}$ | area of cross section of concrete block | $mm^2$ |
| $b$ | width of hybrid laminate | mm |
| $b_{frp}$ | width of FRP sheet | mm |
| $b_{con}$ | width of concrete | mm |
| $f'_{con}$ | compressive strength of concrete | MPa |
| $E_{frp}$ | modulus of FRP sheet | MPa |
| $E_{con}$ | modulus of concrete | MPa |
| $E_{ca}$ | modulus of carbon fiber | MPa |
| $E_{gl}$ | modulus of glass fiber | MPa |
| $E_{ma}$ | modulus of matrix | MPa |
| $E_{adh}$ | modulus of adhesive | MPa |
| $E_1$ | modulus of hybrid FRP laminate before carbon fiber fracture | MPa |
| $E_2$ | modulus of hybrid FRP laminate after carbon fiber fracture | MPa |
| $G_{adh}$ | shear modulus of adhesive | MPa |
| $G_f$ | interfacial fracture energy | N/mm |
| $L_e$ | effective bond length | mm |
| $L$ | total bond length | mm |
| $P_d$ | initial debonding load | N |
| $P_1$ | carbon fracture load | N |
| $P_2$ | load at glass fiber elongation | N |
| $P_3$ | load after temporal dropping | N |
| $P_4$ | ultimate pullout load | N |
| $P_u$ | ultimate bond strength | kN |
| $t_{ca}$ | thickness of carbon fiber ply | mm |

| | | |
|---|---|---|
| $t_{gl}$ | thickness of glass fiber ply | mm |
| $t_{max}$ | thickness of matrix in FRP laminate | mm |
| $t_{frp}$ | thickness of hybrid laminate or FRP sheet | mm |
| $t_{adh}$ | thickness of adhesive | mm |
| $t_1$ | thickness of hybrid laminate before carbon fracture | mm |
| $t_2$ | thickness of hybrid laminate after carbon fracture | mm |
| Tg | glass transition temperature | |
| $\sigma_{gl}^1$ | tensile stress of glass fiber when carbon fiber crack | MPa |
| $\sigma_{gl}^2$ | tensile stress of glass fiber after carbon fiber crack | MPa |
| $\varepsilon_{ca}$ | ultimate strain of carbon fiber | $\mu\varepsilon$ |
| $\varepsilon_{gl}$ | ultimate strain of glass fiber | $\mu\varepsilon$ |
| $\varepsilon_{frp}(x)$ | strain of hybrid laminate at x mm from load end | $\mu\varepsilon$ |
| $\varepsilon_{con}$ | strain of concrete block | $\mu\varepsilon$ |
| $\varepsilon_d$ | tensile strain of hybrid laminates at debond load $P_d$ | $\mu\varepsilon$ |
| $\varepsilon_1$ | tensile strain of hybrid laminate at $P_1$ | $\mu\varepsilon$ |
| $\varepsilon_2$ | tensile strain of hybrid laminate after glass fiber elongation | $\mu\varepsilon$ |
| $\varepsilon_3$ | tensile strain of hybrid laminate at $P_3$ | $\mu\varepsilon$ |
| $\varepsilon_4$ | strain of hybrid laminates at ultimate load | $\mu\varepsilon$ |
| $\tau(x)$ | bond stress at x mm from load end | MPa |
| $\gamma(x)$ | shear strain of adhesive at x mm from load end | $\varepsilon$ |

# Table of Contents

# List of Figures

# List of Tables

# Chapter 1 Introduction

## 1.1 Background

Deterioration of reinforced concrete structures due to corrosion has become a serious concern in North America as the structures approach their design life and their service conditions become more severe. In Canada, repair of concrete bridge decks damaged by deicing salt alone costs billions of dollars (Canadian Council, 2005). New technology and advanced materials systems are urgently needed for durable design of both new and renovated structures. Among the potential solutions is the use of fibre reinforced polymer (FRP) composites as internal or external reinforcement for concrete structures, because FRP has shown excellent corrosion resistance. Other properties of FRP, such as its lightweight, fast construction, high tensile strength and designable ability are also advantageous to their uses.

## 1.2 Hybrid FRP composites

Although fibre reinforced polymer has been identified as an attractive candidate material, the adaptation of FRP to civil infrastructure has been slow, especially in concrete reinforcements. This can be attributed to high material costs, lack of a proven trace record, low modulus of elasticity and lack of ductility.

Ductility is the ability of materials, members or structural systems to undertake large inelastic deformation without significant loss of strength (Park and Paulay, 1976). For civil engineering, in the extreme event of a structure loaded to failure, ductility design is necessary to give forewarning and to prevent catastrophic failure (Harris et al., 1998).

As is well known, FRP is a non-yielding material and fails in a brittle manner; thus, the flexural response of FRP reinforced concrete beams and slabs exhibits little ductility. Without any failure warning in advance, conventional single FRP material breaks suddenly. Thus, there is a need to develop ductile FRP composite material that can show yielding-type of stress strain behaviour. Another challenge for FRP is the low modulus of elasticity if only glass fibre is used as reinforcement. To tackle this problem, hybrid composite may offer an economic solution.

The term “hybrid composite” is employed to describe an FRP composite containing more than one type of fibre materials, which can be an attractive structural alternative for the following reasons: 1) It provides designers with the freedom of tailoring composites and achieving properties that cannot be realized in conventional systems containing only one type of fibre dispersed in matrix; 2) It combines expensive fibres such as carbon and boron with less expensive fibres such as glass and aramid; and 3) Hybrid composites may potentially achieve a balance of stiffness, strength and increased elongation to failure.

In addition, hybrid materials also demonstrate lighter weight, reduced notch sensitivity, improved fracture toughness, long fatigue life if a suitable combination of different fibres is selected (Chou et al., 1980). Current hybrid composites application employs boron, carbon, glass and aramid fibres in aerospace and defence industries and in civil engineering field. During past decades, hybrid fibre reinforcing bars for concrete have also been developed to provide a post-peak ductility (Belarbi et al., 1996). Hybrid composites were also used for external strengthening in structural rehabilitation (Wu, et al., 2006).

## 1.3 Wet-bond technology

Stand alone all-composite structures provide an ideal option for corrosion resistant design. However, due to the low stiffness of FRP materials with all-glass fibre reinforcement, its design is challenged by a relatively large deformation. The problem can be solved if all-carbon fibre reinforcement is used. Nevertheless high brittleness of carbon fibre reinforcement causes failure without any warning. Besides, the solution is unpractical since the cost is high. The other option is to use hybrid FRP composites with filled concrete to have a composite structure, which is similar to conventional steel-concrete composites construction. It can be concrete-filled FRP beams, decks and columns etc. In all of these FRP-concrete components, the main function of concrete is to take compressive load and improve the stiffness of the overall structure while the FRP to carry the tensile load and serve as permanent formwork.

FRP stay-in-place formwork concept has been developed for more than 10 years. Conventional connection between concrete and FRP formwork is done by shear keys, around which bond strength is concentrated and failure is basically caused by delamination cracks and loss of composite action. In this case, carbon fibre was under utilized because of inadequate shear transfer (Hall and Mottram, 1998).

It is necessary to exploit other methods to improve the performance of FRP-concrete system. Wet-bond technology has been developed for hybrid FRP-concrete composite system using hybrid FRP profiles as stay-in-place formwork and external reinforcement. The wet-bond technology was studied to achieve the adhesive bond between prefabricated FRP sheet and cast-in-place concrete (Shao et al., 2005). It was found that the type of resin played a critical role in achieving bond strength. Fresh concrete cast directly to fresh resin could result in sufficient curing in both materials and establish a bond equivalent to fresh concrete cast to cured resin with imbedded aggregates. Wet-bond technology provides an easy tool to design innovative FRP-concrete composite structures using conventional formwork concept and on-site cast-in-place concrete.

## 1.4 Objectives of research

The system employing hybrid laminates bonded to cast-in-place concrete will be investigated in this research to understand wet-bond technology and the contributions by hybrid laminate to structural design. The objectives are four-fold:

### (1) To study hybrid laminate behaviour

The advantage of hybrid laminate over single FRP is that it can provide more ductility as is required by a structure to prevent brittle failure. Understanding of hybrid laminate is essential to study the bond between hybrid laminate and cast-in-place concrete.

### (2) To understand wet-bond mechanism

Wet-bond technology differs from dry-bond in that in wet-bond fresh concrete is cast over fresh epoxy adhesive while in dry-bond fresh epoxy is applied on hardened concrete surface. The challenge of wider use of FRP and cast-in-place concrete is based on whether the bond between prefabricated FRP and cast-in-place concrete can be secured after hardening of the concrete and the epoxy. The bond between prefabricated laminate and cast-in-place concrete was rarely studied before. This project is to examine the possibility of using epoxy adhesive technology to achieve a wet-bond capacity. Single lap pullout tests will be conducted to evaluate wet-bond properties and compare wet-bond with conventional dry-bond.

### (3) To examine wet-bond durability

Structural performance of FRP-concrete composite system is dependent on bond properties between concrete and FRP materials, which could be significantly impeded due to the introduction of various environmental exposures. Bond along the FRP/concrete interface region plays a critical role in such premature failures. In particular, moisture and temperature effects have been identified as important environmental deterioration agents promoting premature failures. While the durability of dry-bond behaviour between FRP and hardened concrete has been extensively studied, research regarding the durability of wet-bond is rare.

In this project, wet-bond capacity will be compared with conventional dry-bond that are accomplished with hardened concrete strengthened by FRP laminates using the same epoxy adhesive experiencing four different environmental exposures: freeze-thaw cycling, wet-dry cycling, continuous cold temperature and continuous hot moisture conditions.

**(4) To evaluate fracture energy of wet-bond**

Interfacial fracture energy is used as a bond property criterion to evaluate wet-bond and dry-bond. Comparison of the quality of wet-bond and dry-bond is based not only on their bond strength, but also on interfacial fracture energy release. The expression of fracture energy of bond between hybrid laminate and concrete is desired. Moreover analytical modeling will be performed.

## 1.5 Structure of the thesis

A comprehensive literature review will be summarized in Chapter Two and followed by Chapter Three on experimental program, including the introduction of fabrication of carbon and hybrid laminates, wet-bond and dry-bond techniques. In addition, set up of single lap pullout tests and different durability environmental exposure conditions are discussed. Experimental results and discussions are presented in Chapter Four where the wet-bond is compared with dry-bond. In Chapter Five, analytical modeling is performed to describe behaviour of hybrid laminate and corresponding bond failure process. Conclusions are drawn in Chapter Six with recommended future works.

# Chapter 2 Literature Review

This chapter presents a literature review of previous research on the behaviour of FRP composites bonded with concrete, including FRP materials, hybrid FRP composite laminates, concrete effect, epoxy adhesive, durability exposure and interface fracture energy.

## 2.1 FRP materials

The most commonly used fibres in structural applications are glass and carbon fibres. There are different types of glass fibres and carbon fibres, which vary in terms of elastic modulus, strain and thermal expansion etc.

### 2.1.1 Glass fibre

Glass fibres exhibit the typical glass properties of hardness, corrosion resistance, and inertness. Furthermore, they are flexible, lightweight, and inexpensive. These properties make glass fibres the most common type of fibre used in low-cost industrial applications. All glass fibres have similar stiffness in a range of 50-85 GPa, but different strength values and different resistance corresponding to environmental degradation. A commonly used glass fibre for continuous FRP reinforcement in civil engineering is E-glass fibre. Its maximum tensile strength measured in single fibre tests (ASTM D3379, American Society for Testing and Materials) may high up to 3.5 GPa, but the value can’t be realized in a composite because damage during the various stages of processing can reduce fibre strength to as low as 1.75 GPa. The reduction of fibre strength in composite with respect to the strength of virgin fibre is also caused by other factors, such as residual stresses, elevated temperature or chemical corrosion. To account for these effects, a safety ratio of 3.5 is used in the design of glass-reinforced composites (Barbero, 1999).

### 2.1.2 Carbon fibre

Carbon fibres are lightweight and strong fibres with excellent chemical resistance. Unlike glass fibres, carbon fibres are available with a broad range of stiffness values from 200 GPa to 700 GPa. The properties of carbon fibres depend on the raw material and its manufacturing process. Being stiffer than glass fibres, carbon fibres provide better fatigue characteristics to the composite by reducing the amount of strain in the polymer matrix for a given load. Also, the stress corrosion (static fatigue) phenomenon is less marked for carbon fibres.

The major limiting factor for the application of carbon fibres is the cost. Carbon fibres are lighter and stiffer than glass fibres, but it is difficult to show an economic advantage when all-carbon fibre composite structures are built substituting a conventional material such as steel in structures that are not weight critical.

### 2.1.3 Fracture of unidirectional single fibre composite

Failure process of single fibre composite was observed by electron microscopy technology. It shows that the whole process is in the following order: fibre breakage begins to occur at a load of about 60% of its failure load; as the applied load is increased, plastic deformation occurred first from the broken fibre tip along the fibre sides, followed by final matrix cracking in the plastic region; just before failure, local debonding between fibre and matrix occurred, originating from fibre breakage and matrix cracking; finally a catastrophic crack propagation occurred from the crack area, leading to composite failure (Sato et al, 1986).

## 2.2 Hybrid FRP composite

To overcome the shortcoming of non-yielding FRP materials, Mufti et al. (1996)

suggested the design of reinforced concrete sections using FRP be based on the concept of deformability and ductility that is commonly used in steel-reinforced concrete sections. Belarbi (1996) concluded that a hybrid composite consisting of several brittle fibres of different stiffness and ultimate strains could be made to behave as a pseudo ductile material. Starting with the observation of braided aramid fibre around steel core in an epoxy matrix, hybrid FRP rebar has been developed over more than 10 years (Nanni et al. 1994). The creation of hybrid FRP composite laminate by combining more than one different reinforcing fibre to produce a ductile stress-strain behaviour is one of the subjects of this research project.

### 2.2.1 Hybrid effect

Hybrid effect is related to the ratio of two different fibres with different ultimate strain and their dispersion on the matrix. Hybrid laminates usually fail starting from failure of the lower elongation fibre. It is noted that the failure strain of low elongation fibre is increased but that of the high elongation fibre is decreased if compared with their respective ultimate strain obtained from individual tests (Manders and Bader, 1981). When the concept is extended to hybrid laminate studied herein, it implies that the failure strain for carbon fibres increases while the failure strain of glass fibres decreases.

Basic mechanical properties of hybrid FRP materials can be estimated if the properties of the constituent materials (fibres and matrix) and their volume fraction are known. This may be accomplished by applying the “rule of mixture” simplification as follows:

$$E_{frp} = E_{fiber}V_{fiber} + E_{matrix}V_{matrix} \tag{2.1}$$

$$f_{frp} \approx f_{fiber}V_{fiber} + f_{matrix}V_{matrix} \tag{2.2}$$

Where:

$E_{frp}$= young’s modulus of hybrid FRP in fibre direction

$E_{fibre}$, $E_{matrix}$ = Young’s modulus of fibres and matrix

$V_{fibre}$, $V_{matrix}$ = volume fraction of fibres and matrix

$f_{frp}$= tensile strength of hybrid FRP in fibre direction

$f_{fibre}$, $f_{matrix}$ = tensile strength of different fibres and matrix

It is noted that in the above equations $V_{fibre}+V_{matrix}=1$. Also, typical values for the volume fraction of different fibres in prefabricated strips are in the order of 0.5-0.65.

### 2.2.2 Hybrid behaviour

An idealized stress-strain curve of a hybrid composite containing both high elongation and low elongation fibres is shown in Figure 2.1. There are three important features which include the elastic behaviour indicated by OA, where point A is the fracture of low elongation fibre at its ultimate strain $\varepsilon_{le}$; the plateau AB indicating the load transfer from low elongation fibre to high elongation fibre causing the stretch of high elongation fibres to $\varepsilon_B$; finally continuous reloading at reduced slope BC until the ultimate strain of the higher elongation fibre of $\varepsilon_{he}$ (Chou et al.1980).

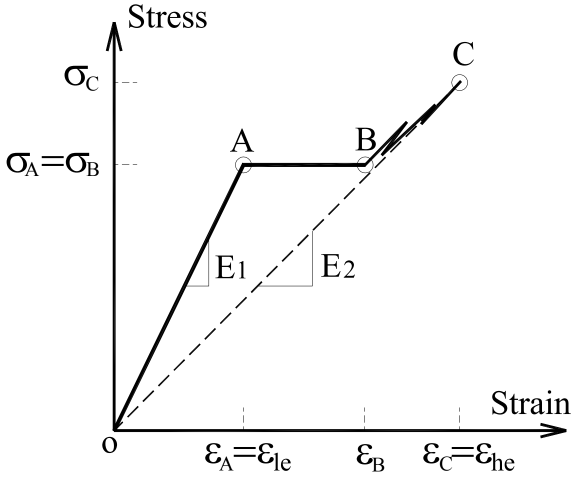

**Fig. 2.1: Ideal stress-strain curve of a hybrid composite material**

Note: $\varepsilon_{le}$ = ultimate strain of low elongation fibre
$\varepsilon_{he}$ = ultimate strain of high elongation fibre

The load originally carried by the low elongation fibre has to be transferred to the high elongation fibre after the first cracks. The shifted loads can be estimated by the difference of the two different fibres' stress at fracture point. After cracking, it is noted that the initial fracture in the low elongation fibre does not totally propagates across the high elongation fibre far from fracture plane and load can be progressively diffused back into the low elongation fibre temporarily because the rest well-bonded part is still strong enough to take the load. Load sharing is proved from multiple fractures in well-bonded hybrid composite and by the bursts of acoustic emission accompanied with the repeated load drops on stress-strain curve (Chou et al.1980). The first crack of low elongation fibre is the most obvious and predominant one, the following multiple fractures have not much effect. In addition, Razaqpur and Ali (1996) tested hybrid reinforcement (high density polypropylene and carbon fibre) in reinforced concrete beams, besides glass fibre elongation, a temporary load drop was also observed at first CFRP fracture in their results although they were not able to measure it.

## 2.3 FRP bonded with concrete

Extensive research has been conducted on bond behaviour of FRP laminates to hardened concrete, which is referred as dry-bond, and mainly used in structural repair and upgrade. The success of FRP materials in structural repair is mainly dependent on the bond between FRP laminates and concrete, which is the medium to transfer load from concrete to FRP materials. Any factors causing debonding may lead to brittle failure and expected composite action can't be achieved. Generally, the anchorage failure between FRP and concrete interface are due to: poor distribution or lack of adhesive; existence of wider flexural cracks or shearing cracks in concrete; coarse concrete surface; fatigue loading etc. The other factors that can also affect quality are epoxy property, moisture, temperature, and stiffness of FRP materials.

This renovation technique can also be used in new structure construction, in which FRP material serves as stay-in-place formwork and external reinforcement. Composite bridge deck made of FRP formwork and cast-in-place concrete is the typical new constructed composite structure with better corrosion resistance capacity and longer service life than conventional structure and has been used for many projects during the past decade (Hall and Mottram, 1998). More researches are still needed to understand the system.

### 2.3.1 Wet-bond by epoxy adhesive

There are two methods to bond FRP with cast-in-place concrete: shear key method and adhesive method. Shear key method mainly depends on mechanical anchorage. Research showed that shear keys brought stress concentration and failure was basically induced by the local bearing crack at FRP, which caused the loss of complete composite action. Since shear transfer was inadequate, composite materials are underutilized (Bayasi and Kaiser, 2003). If the number of shear keys was increased, stress concentration was raised due to the need to provide holes in FRP sheets for shear connection to concrete. A better load transfer mechanism was recommended to fully utilize the composite system (Burgueno et al. 2004).

Wet-bond method is comprised of prefabricated FRP profiles, made by either hand lay-up or pultrusion, and cast-in-place concrete as a core. The bond between the prefabricated FRP and cast-in-place concrete is realized through an epoxy adhesive that is coated on the inner surface of FRP profiles. Research was done on wet-bond behaviour using standard JSCE (Japan Society of Civil Engineers) pullout tests and also compared to conventional dry-bond using hardened concrete strengthened by FRP laminate. It was found that the load displacement curves, the strain distributions in FRP and the interfacial fracture energy of dry-bond and wet-bond specimens were closely comparable, suggesting that an appropriate bond was achieved by casting concrete directly to composite profile via a fresh epoxy adhesive. The wet-bonding technology is crucial to the development of cast-in-place concrete structures using FRP composite profiles as externally bonded reinforcements. (Shao et al., 2005)

Wet-bond technology was also applied to full scale FRP-concrete composite beam tests using FRP U-shape profiles as stay-in-place formwork and external reinforcement. It was found that the type of resin played a critical role in achieving bond strength. Fresh concrete cast into FRP formwork through fresh resin could obtain sufficient curing in both materials and establish a bond equivalent to hardened concrete beam reinforced by the same FRP materials and the same type of adhesive (Shao et al., 2005). Compared to an RC beam of 1.5% reinforcement ratio, the fabricated composite beams using wet-bond showed an excellent enhancement in first crack strength, yielding strength, ultimate loading capacity and post-yielding ductility, although the improvement in flexural stiffness was not apparent. Wet-bond technology provides an easy tool to design innovative FRP-concrete composite structures using conventional formwork concept and on-site cast-in-place concrete. Such concrete structures do not require internal steel reinforcement and can fully depend on the external FRP profile. It is believed that the design will eventually lead to the establishment of corrosion resistant and maintenance-free concrete structures which are best suited to the harsh marine environment (Shao et al., 2005).

### 2.3.2 Bond failure modes

Efforts (most on FRP with hardened concrete) have been made to understand the debonding failure of dry-bond, such as peel debonding and lap shear debonding. Three materials (FRP, adhesive, concrete) and two interfaces (FRP/adhesive and adhesive/concrete) are involved in debonding behaviour and five distinct debond modes are possible. They are, namely: (1) FRP delamination; (2) FRP/ adhesive separation; (3)

adhesive de-cohesion; (4) adhesive/concrete separation; and (5) concrete substrate fracture. Failure modes (1), (3) and (5) are considered material de-cohesion, while (2) and (4) are considered interface fracture. Research has shown that most experimental joints failed in the concrete a few millimeters beneath the concrete/adhesive interface and other failure models are rare (Maeda et al.1997).

### 2.3.3 Anchorage strength and effective bond length

The tension in laminates is transferred to concrete mainly via bond stress in the adhesive in a short length nearest to the loaded end. With the increase of loading, more force is transferred from the FRP laminate to the concrete until micro-cracks develop in the substrate of concrete. The cracking of concrete substrate near load end causes a shift of the active bond zone to new areas further away from the load end, and only part of the bond is effective. The implication is that the anchorage strength cannot always increase with an increase in the bond length, and ultimate tensile strength of laminate may never be reached however long the bond length is. This leads to the important concept of effective bond length, beyond which any increase in bond length cannot increase the anchorage strength, as confirmed by many experimental studies (Chajes et al. 1996; Maeda et al. 1997; Tajsten 1997) and fracture mechanics analyses (Yuan and Wu, 2001). But longer bond length provides larger bond area for active zone to shift, which may improve the ductility of the failure process (Chen and Teng, 2001).

Various debond models for FRP sheets adhesed to hardened concrete have recently been proposed, which can be classified into three categories — empirical models (Maeda et al. 1997) which are based directly on the regression of test data, fracture mechanics models (Blaschko et al., 1997), and design models (Brosens and Gemert, 1998) that generally make use of some simple assumptions for certain materials and situation. A practical simple model is proposed by Chen and Teng (2001):

$$P_u = 0.427\beta_{frp}\beta_L\sqrt{f_{con}'}b_{frp}L_e \tag{2.3}$$

$$L_e = \sqrt{\frac{E_{frp}t_{frp}}{\sqrt{f_{con}'}}} \qquad \beta_L = \begin{cases} 1 & if\ L \geq L_e \\ \sin\frac{\pi L}{2L_e} & if\ L \leq L_e \end{cases} \qquad \beta_{frp} = \sqrt{\frac{2 - b_{frp}/b_{con}}{1 + b_{frp}/b_{con}}}$$

Where:

$P_u$ = ultimate debond load, kN
$L_e$, L = effective bond length and total bond length, mm
$b_{frp}$, $b_{con}$ = the width of FRP sheet and concrete, mm
$E_{frp}$ = modulus of FRP sheet, MPa
$t_{frp}$ = thickness of FRP sheet, mm
$f'_{con}$ = compressive strength of concrete, MPa

### 2.3.4 Bond stress-slip behaviour

The behaviour of interface between FRP and concrete is the key factor controlling bond failures in FRP-strengthened RC structures. In particular, a reliable local bond–slip model for bond interface is of fundamental importance for accurate modeling and understanding of bond failures. It should be noted that the term “interface” is used to refer to the interfacial part of the FRP-to-concrete bonded joint, including the adhesive and a thin layer of the adjacent concrete substrate, responsible for the relative slip between the FRP plate and the concrete prism, instead of any physical interface in the joint.

Research has shown that typical bond–slip curves should consist of an ascending branch with continuous stiffness degradation to the maximum bond stress and a curved descending branch reaching zero bond stress at a finite value of slip shown in figure 2.2:

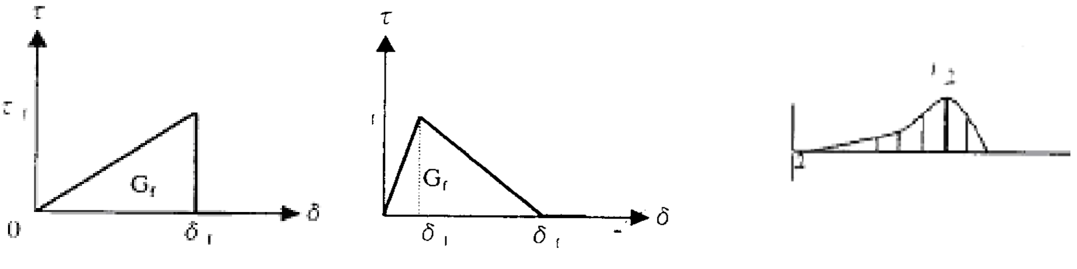

**(a) Linear ascending model** **(b) Linear ascending and descending model** **(c) Typical stress-strain curve**

**Fig. 2.2: Simplified local shear stress-slip relations (Lu et al. 2005)**

While a precise bond–slip model should consist of a curved ascending branch and a curved descending branch, a bilinear model can be used as a good approximation. An accurate bond–slip model should provide close predictions of both the shape and fracture energy (area under the bond–slip curve) of the bond–slip curve. But none of the existing bond–slip models provides accurate predictions of both the shape and the interfacial fracture energy as found from tests (Lu et al., 2005).

## 2.3.5 Fracture energy

The initiation and propagation of interfacial cracks along FRP-concrete interface may affect the concrete cracking behaviour, load-carrying capacities and stiffness characteristics. The fracture mechanics based on energy is considered to be appropriate for evaluating the interfacial fracture resistance and other composite behaviour of the FRP-strengthened structures. The debonding load can be expressed by two synthetic parameters: stiffness of FRP laminates and interfacial fracture energy, as follows (Dai and Ueda, 2003):

$$P_u = b_{frp}\sqrt{\frac{2E_{frp}t_{frp}G_f}{1+\alpha}} \qquad \alpha = E_{frp}A_{frp} / E_{con}A_{con} \qquad (2.4)$$

Where:

$E_{frp}$, $E_{con}$ = modulus of hybrid FRP sheet and concrete, MPa

$A_{frp}$ = bond area of FRP sheet, $mm^2$
$A_{con}$ = area of concrete block, $mm^2$
$G_f$ = interfacial fracture energy

## 2.3.6 Influencing factors on bond

### 2.3.6.1 Concrete

Concrete surface properties play an important role for dry-bond quality. Many experimental studies show that most failure of externally bonded FRP laminates to concrete specimens typically occurs at the interface between the FRP laminates and the concrete surface. The effect of surface roughness and surface cleanness on the pull-off strength seems to be significant. Results show that surface treatment by water jet produces a better bonding strength than surface treatment by sander (Toutanji and Ortiz, 2001).

The concrete composition also has some influence on bond strength. Theoretical analysis indicates that the shear stress distribution along FRP-concrete interface is partially affected by concrete components, especially where cracking has already occurred in the concrete substrate and aggregate interlock action is leading to ultimate load level. Furthermore, surface tensile strength of concrete instead of whole concrete block strength dominates the bond capacity. Research results show that increasing aggregate content can improve ultimate bond capacity as well as reduce the bond softening behaviour. (Leuing et al, 2005)

### 2.3.6.2 Epoxy

In civil engineering applications, epoxy adhesive is used to repair concrete structures. Water, alkalis, and other contaminants on the concrete surface may interact with the epoxy adhesive, thus influencing the epoxy curing reaction, including both curing rate and degree of cure. Another important parameter to consider is glass transition temperature, Tg, which is a measure of mobility of the molecular chains in the polymer network as a function of temperature. Due to the restrictions of on-site processing, only a low glass transition temperature (Tg) of epoxy can be obtained during curing, which limits the service temperature and increases the sensitivity of epoxy adhesive to environmental exposures, such as humidity, temperature etc. In addition, mechanical properties and durability of epoxy adhesives are greatly affected by its degree of cure (Petrie, 2006).

Some kinds of epoxy adhesives are cured in the presence of water. They are different from those cured without moisture in curing reaction, mechanical properties and durability. A small amount of water can accelerate the curing rate, increases the degree of cure, flexural modulus and the bonding strength, while it decreases water uptake and the rate of degradation of the flexural modulus (Wu, et al. 2004).

### 2.3.7 Durability of bond

While short-term bond behaviour has been extensively studied, durability of bond is not well explored. A recent experimental work (Grace, 2004) showed that structural performance of FRP retrofitted systems could be significantly impeded due to the introduction of various environmental effects, and bond in the FRP/concrete interface region played a major role in such premature failures. In particular, moisture and temperature effect has been identified as important environmental deterioration mechanisms promoting premature FRP composite system failures. Research work (Grace, 2004) were conducted for an array of tests on 78 large-scale retrofitted RC beams using CFRP plates and fabrics which were subjected to various environmental exposures, including water, saltwater, freeze-thaw, dry heat, and alkalinity. After 10,000 hours of respective continuous exposure, it was concluded that moisture could do the most damage in terms of ultimate beam strength, resulting in a 30% and 10% respective reduction for

CFRP plate and CFRP sheet bonded beams. Debonding was observed as the primary failure mode, although details of such failures were not described explicitly.

#### 2.3.7.1 Moisture

Research shows that the effect of moisture on debonding is a complex phenomenon that involves physical changes in the bond as well as in its constituent materials. Karbhari and Zhao (1998) observed micro-cracking in the GFRP laminate in retrofitted cement mortar beams that were mechanically tested to failure under a four-point loading configuration. After 120 days of continuous moisture exposure, a 40% reduction in flexural strength was observed. Interface fracture analysis indicates that this kind of interfacial debond mode is attributed to an interfacial material toughening and an interface weakening mechanism as a consequence of water diffusion (Ching and Oral, 2006).

#### 2.3.7.2 Temperature

Epoxy adhesive used to form the bond between carbon fibre reinforced polymer (CFRP) and concrete is sensitive to temperature variations. In general the bond properties deteriorate rapidly with exposure to high temperatures. Rapid loss of strength was apparent when epoxy temperature increased beyond $60^oC$. At low temperatures, CFRP strengthened concrete specimens failed at similar loads as in room temperature. This indicates that the adhesive bond strength between CFRP sheet and concrete is not adversely affected by low temperature. Furthermore, long term constant freezing at $-17.8^oC$ exposure results in a minor increase in flexural strength of samples over time (Wu et al. 2006).

#### 2.3.7.3 Wet and dry cycling

Reduction in ultimate strength and stiffness due to wet/dry cycling was generally observed. Chajes (1996) showed a 36% decrease in ultimate strength for glass fibre retrofitted samples that were subjected to 100 wet/dry cycles, while a 19% reduction was shown for carbon fibre bonded samples. On the other hand, a strength reduction that ranged from 3% to 33% was observed on specimens made of various epoxy and FRP systems that were subjected to 300 wet/dry cycles in salt water (Toutanji and Gomez 1997). Debonding mode failure was reported and generally took place near the FRP/concrete interface. Mukhopadhyaya et al. (1998) found similar degradation trends on GFRP double-lap shear specimens that were subjected to comparable wet/dry conditioning. The reduction in strength may be attributed to the degradation of the epoxy, which led to the weakening of the bond between concrete specimens and FRP sheets (Houssam et al. 1997).

#### 2.3.7.4 Freeze/thaw cycling

Based on freeze/thaw cycle analysis of FRP bond with concrete structure, it was found that failure surface changes with increasing number of freeze-thaw cycles. Failure surface occurs mostly at substrate of concrete. The most reasonable explanation is that the adhesive was affected by freeze-thaw exposure, reducing shear stresses transferred to the concrete. But for load carrying capacity of joint between concrete and FRP laminates, freeze-thaw cycling does no significant influence (Green et al., 2005).

Tests conducted by Dutta and Hui showed that freeze-thaw exposure in dry air between 4.4 and -17.8$^{o}$C resulted in minor changes in flexural strength, storage modulus and loss factor regardless of cycle length. Thus thermal cycling in dry air shows no appreciated damage (Wu et al. 2006). On the contrary, combined with moisture, freeze-thaw cycling was seen to result in mechanisms of brittleness, matrix micro-cracking, and fibre-matrix debonding with the effects being more prominent on strength rather than modulus. The moisture uptake is also seen to result in a decrease in glass transition temperature (Abanilla et al., 2005).

# Chapter 3 Experimental Program

Two different tests were conducted to study the behaviour of hybrid laminates and wet-bond of these laminates to cast-in-place concrete. The first one was uni-axial tensile test of hybrid laminates to examine pseudo-ductility of hybridization and the second one was pull-out test to quantify wet-bond behaviour and compare with it dry-bond which has been mostly practiced. Durability of wet-bond was evaluated for freeze-thaw cycling, wet-dry cycling, continuous hot moisture and continuous freezing condition. For comparison, dry-bond control samples were examined under the same exposure.

## 3.1 Materials

### 3.1.1 Concrete

Concrete mixture includes Type 10 Portland cement, water, river sand, silica fume, crushed limestone aggregate with a maximum size of 6 mm. In order to reduce moisture influence, water to cement ratio was fixed to 0.32 with the help of super plasticizer. The mixture proportion of concrete is given in Table 3.1.

**Table 3.1: Mixture proportion of concrete**

| Item | Portland cement | Silica fume | Water | S.P(ml) | 6 mm crushed lime stone | River sand |
|---|---|---|---|---|---|---|
| Mass | kg/ m$^3$ | kg/m$^3$ | kg/m$^3$ | ml/m$^3$ | kg/m$^3$ | kg/m$^3$ |
| | 450 | 50 | 145.7 | 19800 | 1050 | 689 |
| Volume ratio | 14.3% | 2.38% | 14.6% | 1.98% | 39.0% | 26.0% |
| Weight to cementitious material ratio | 1.00 | | 0.32 | 0.015 | 2.11 | 1.38 |

### 3.1.2 FRP fibre and resin

Both carbon and glass fibre sheets were used in making hybrid FRP laminates.

Mechanical properties of carbon fibre and glass fibre provided by the manufacturer are shown in Table 3.2. Carbon fibre used is a high modulus fibre with an ultimate strain of 0.35% and it is expected to enhance system in linear elastic range and to break at its ultimate strain to provide ductility. E-glass fibre used has a larger ultimate strain and expected to carry load after carbon breaks.

Epoxy resin used was in two-component adhesive with high modulus, high strength and room temperature curing, and half hour quick hardening to concrete bond. The properties of epoxy resin are shown in Table 3.3.

**Table 3.2: Mechanical properties of fibre sheets (manufacturer data)**

| Type of material | Thickness (mm) | Tensile Strength (MPa) | Modulus (GPa) | Maximum strain % |
|---|---|---|---|---|
| Carbon fibre (C7) | 0.143 | 1900 | 540 | 0.35 |
| E-glass fibre (EG) | 0.118 | 1790 | 80 | 2.2 |

**Table 3.3: Properties of epoxy resin**

| | |
|---|---|
| Mixing ratio (Parts A:B) by volume | 1:1 |
| Pot life (a gal unit) min. | 15-25 |
| Gel time, min. | 30 |
| Viscosity (mixed), cps | 4250-4750 |
| Ultimate tensile strength (14 days) | 50 MPa |
| Elongation at break, % | 2.5 |
| Modulus | 3 GPa |
| Heat deflection temperature | 51$^{o}$C |
| Linear coefficient of shrinkage | 0.3% |
| Water absorption (7 days, 24 h immersion) % | 0.23 |

## 3.2 Sample preparation

### 3.2.1 Concrete

Cast-in-place concrete blocks for wet-bond sample were 75 mm × 75 mm × 280 mm in dimension and concrete prisms of the same size were prepared for dry-bond control samples. During casting of all samples, concrete was vibrated on a vibration table to make solid compaction. Inner surface of formworks was brushed with oil for easy removing. Fresh concrete was covered with plastic sheet immediately for at least 24 hours to avoid shrinkage. Two days later, concrete blocks or prisms were removed and cured in air at room temperature for 2 weeks before durability exposure. For each batch, three cylinders (50 mm in diameter × 100 mm in height) were cast for concrete compression strength test (ASTM C39-86). The average 28 days compressive strength of concrete is 58.3 MPa ± 6.76 MPa.

### 3.2.2 Fabrication of hybrid FRP laminates

The FRP laminates used in this project were fabricated at McGill University, which were 300 mm long, 25 mm wide and 1.8 mm thick. The total length included 200 mm for bond and 100 mm extensions for gripping.

Hybrid laminates were made of three different materials: carbon fibre, glass fibre and epoxy resin. Hybrid laminate consisted of 5 plies with overall thickness of 1.8 mm, including four glass fibre plies and one carbon fibre ply. Two different kinds of all-carbon laminates were also fabricated, which were two plies laminate and four plies laminate respectively. Laminates were wet-lay up one by one in fibre direction. For hybrid laminates fabrication, four glass fibre plies were put together next to carbon fibre ply. The epoxy matrix for laminates fabrication was the same one used for composite-concrete joint. Thickness of laminate was controlled by the amount of epoxy used in each ply and the weight used to squeeze the residual resin. After 2 days curing, hardened hybrid FRP laminate was cut into strips with 25 mm × 300 mm in dimension. Hybrid FRP laminates properties are shown in Table 3.4.

**Table 3.4: Properties of coupon laminates for uni-axial tensile test**

| Specimen reference number | Type of material | Number of plies | Thickness t (mm) | Width b (mm) | Durability exposure condition |
|---|---|---|---|---|---|
| CC1 | Carbon | 2C | 0.9 | 25 | — |
| CC2 | | 4C | 1.8 | 25 | — |
| CH1 | Hybrid | 1C+4G | 1.8 | 25 | — |
| CH2 | | 1C+4G | 1.8 | 25 | — |
| CH3 | | 1C+4G | 1.8 | 25 | — |
| CH4 | | 1C+4G | 1.8 | 25 | low temp. at -25°C |
| CH5 | | 1C+4G | 1.8 | 25 | 100 cycles of freeze/thaw between -17 °C and 4°C |
| CH6 | | 1C+4G | 1.8 | 25 | hot water at 35°C |
| CH7 | | 1C+4G | 1.8 | 25 | 50 cycles wet/dry |

Note: CC = coupon of carbon fibre laminate; CH = coupon of hybrid laminate

C = carbon fibre; G = glass fibre; 1C+4G = 1 ply carbon plus 4 plies glass

### 3.2.3 Wet-bond samples

For wet-bond samples, laminates were fabricated at least 3 days before concrete casting to ensure hardening of epoxy within laminates. Then laminates were placed on bottom of formwork with carbon fibre facing up (Figure.3.1a) and two plastic spacers were placed at two sides of FRP sheets to prevent FRP sheets from being embedded in concrete. In this way, carbon fibre was bonded directly to concrete and the levelling of FRP laminate will be comparable to dry-bond samples. The schematic drawing of detail of levelling of the FRP laminate is shown in Figure 3.1b. After laminate for wet-bond was uniformly coated by adhesive epoxy, concrete was immediately cast with 2 minutes vibration. All wet-bond samples have the same bond area as dry-bond, which is 25 mm wide × 200 mm long. When concrete was hardened, the two plastic spacers were removed. The finished wet-bond sample is shown in Figure 3.1c. It is noted that at load end, a plastic tape was used on laminate to create a 5 mm notch to prevent epoxy squeezed out on bearing plane (Figure 3.3).

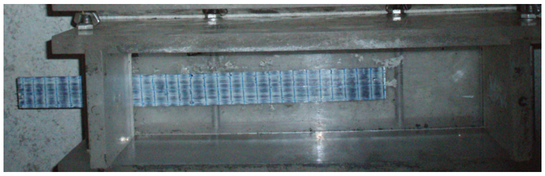

**(a) before concrete casting**

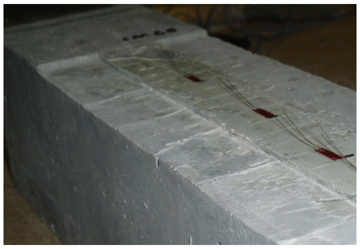

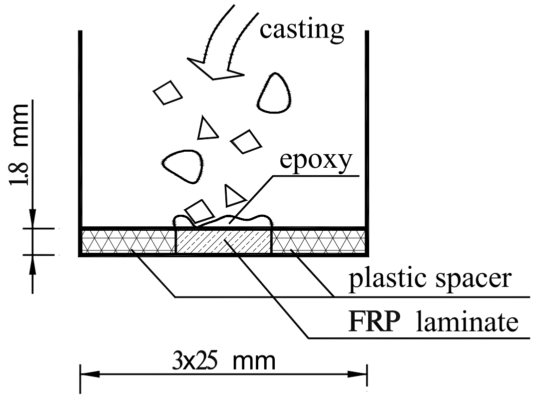

**(c) finished wet-bond sample**

**(b) levelling of FRP laminate**

**Fig. 3.1: Preparation of wet-bond samples**

### 3.2.4 Dry-bond samples

For dry-bond samples, bond surface of hardened concrete was mechanically sand blasted and cleaned. Bonded laminates were fabricated layer by layer before bonding. When laminates were semi-hardened, they were cut to uniform strips with the same size of wet-bond laminates (300 mm × 25 mm). Meanwhile, primer layer of epoxy on bond area was applied and laminates were bonded on concrete with carbon fibre indirect contact with concrete (Figure. 3.2a). It is worth to mention that the method to prepare dry-bond samples with semi-hardened laminates is better preferable to the alternative method consisting in placing half hardened fibre ply directly on concrete layer by layer because it is hard to control the size and thickness of laminates. In addition, to prevent three-dimensional cracking of concrete at loaded end and to avoid epoxy being squeezed on the bearing plane, the load end was cover by plastic tape and bond area started at 5 mm from concrete end (Figure 3.3).

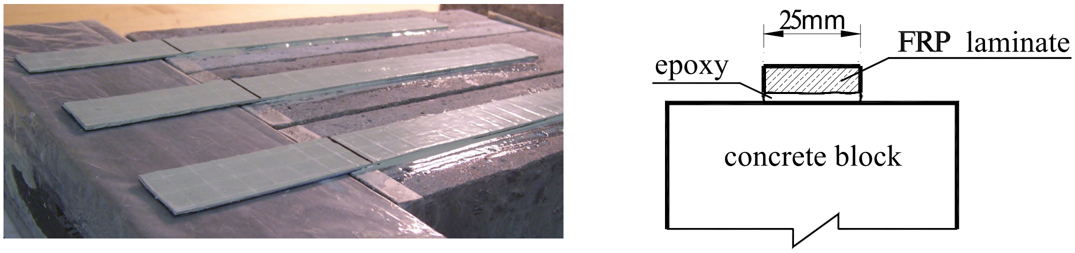

**(a) finished dry-bond sample** **(b) leveling of FRP laminate**

**Fig. 3.2: Dry-bond samples preparation**

It is worth to mention that the volume of epoxy adhesive was controlled to 60 ml for each group and the theoretical thickness of the adhesive layer was 2 mm ($60000\ mm^3 = 200\ mm \times 25\ mm \times 2\ mm \times 6$). Experimentally, the thickness of wet-bond and dry-bond sample were different because most fresh epoxy was squeezed into concrete resulting serrated surface in wet-bond while partial fresh epoxy was squeezed out at two sides of laminate and forming relative smooth interface between epoxy resin and concrete in dry-bond.

### 3.2.5 Arrangement of strain gauges for pull-out test

The arrangement of strain gauges is shown in Figure 3.3. Along the bonded length of FRP laminates, there were three strain gauges placed along the centreline of laminates at various spacing. Considering the strain gauges' size effect, the distance of strain gauges from load end are 2 mm, 40 mm and 80 mm respectively.

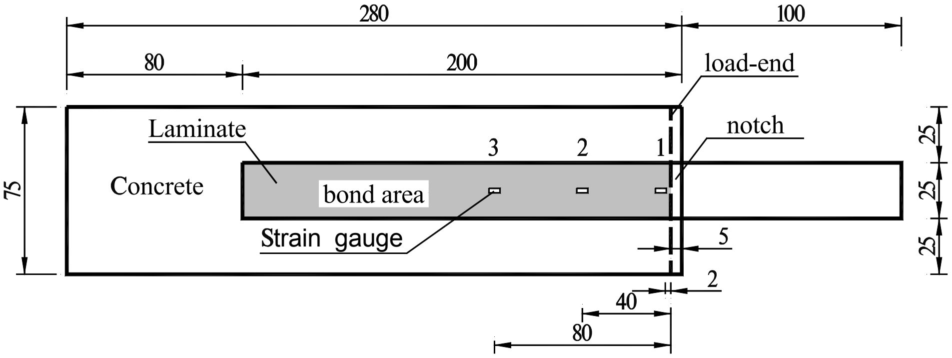

**Fig. 3.3: Arrangement of strain gauges**

## 3.3 Uni-axial tensile tests of FRP laminates

Uni-axial tensile tests were conducted for hybrid laminates properties study. Coupon samples included both all-carbon fibre laminates and hybrid FRP laminates described in Table 3.4. Two strain gauges were used to monitor deformation of laminates and examine the effect of carbon cracking on load-strain curves. In order to control carbon fibre crack position, width was reduced to introduce stress concentration at the middle of laminate. At two ends, there was 50mm long area for clamping in a grip, which was enhanced by edge reinforcement (Figure 3.4).

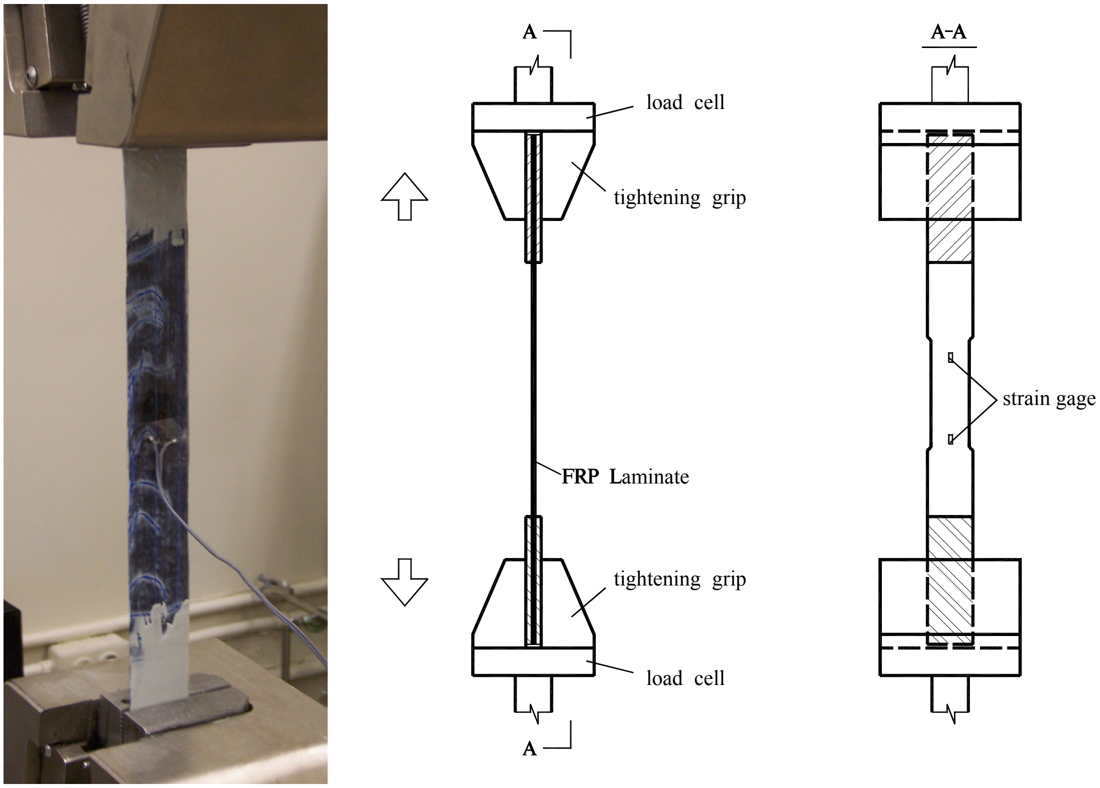

**(a) Photo of test** **(b) Schematic drawing of test set up**

**Fig. 3.4: Uni-axial tensile test**

## 3.4 Single lap pull-out tests on wet-bond and dry-bond samples

Pullout tests were conducted to study the influence of wet-bond on bond behaviour. The set up is shown in Figure 3.5. A concrete prism was clamped in a specially designed loading frame, which consisted of a 50 mm thick bottom steel plate, a 7 mm thick top steel plate and 6 threaded steel rods (four at corner with 17 mm diameter and two at mid side with 8 mm diameter). The top plate had an open slot of 12 mm wide and 50 mm long to facilitate the FRP laminate to the loading grip.

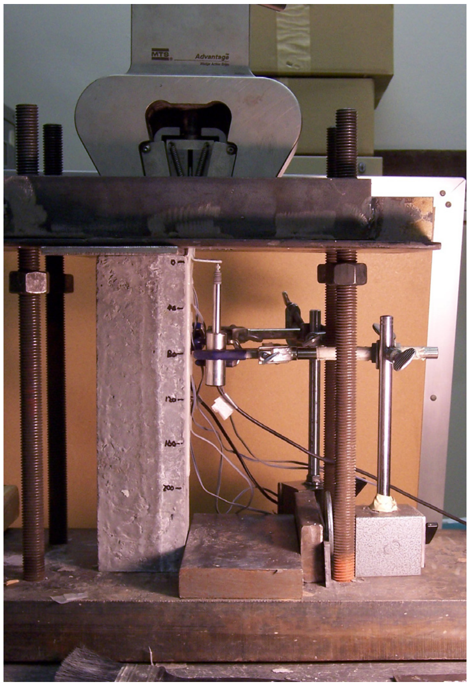

(a) Photo of test set up

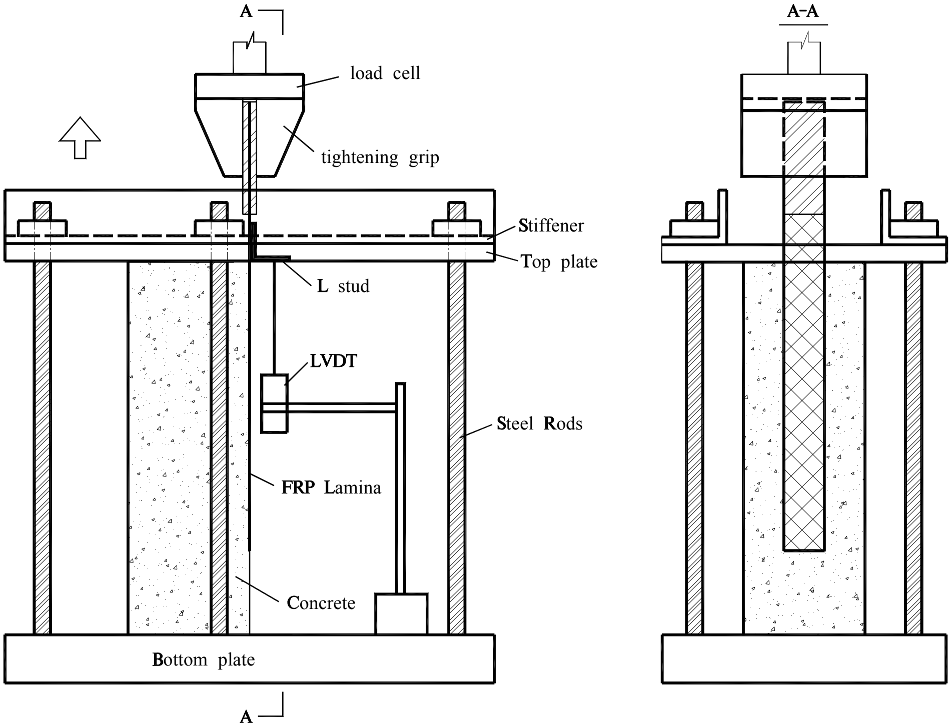

(b) Schematic drawing of test set up

Fig. 3.5: Pullout test

An MTS machine of 150 kN capacity was used to perform the pullout tests with cross head upward moving speed fixed to 0.01 mm per second. Pullout force, strain and slip were recorded by a data acquisition system (Measurement Groups Inc 5100). It was connected with the MTS machine, strain gauges and LVDT described above to record tensile force, tensile strain of laminates and relative slip between laminates and concrete. This system was integrated with operation software — Strain Smart Version 2.21 that allowed data to be converted directly to engineering units, reduced and recorded at an interval of 10 times per second.

In addition, the ultimate debonding load was approximately estimated about 12kN using Eq. 2.1, which implied that only one top steel plate was not strong enough and two L shape stiffeners were added to increase its stiffness (Figure 3.5).

Strain gauges used were from Tokyo sokki kenkyujo Co.Ltd. Japan. Their properties are shown in Table 3.5.

**Table 3.5: Properties of strain gauges**

| Type | FLA-5T-11-3LT |
|---|---|
| Gauge length (mm) | 5 |
| Gauge width (mm) | 1.5 |
| Operating temperature | -20 to +80°C |
| Compensation range | +10 to +80°C |
| Strain limit | 3% (30000×10-6) |
| Resistance (Ω) | 120 |
| Lead wires length | 3-wire 3m |

LVDT is the linear variable differential transformer for displacement measurement. The LVDT used in this project has capacity ranging from 0 mm to 10 mm. A small L-shaped metal stud was bonded to FRP sheet at load end to measure pullout slip using LVDT.

During test, top end of FRP laminate was clamped in grip with protection of edge reinforcement. When FRP laminate was pulled, the upper concrete section came to contact with top bearing steel plate that transmitted resulting pressure to bottom steel plate by six threaded steel rods. The bottom plate was fixed on MTS machine platform. Moreover, the whole debonding process of sample was recorded by video taping in order to better understand the behaviour. Two digital cameras were used simultaneously. One was focused on the interface of bond and the other on the load recorded by the MTS machine to correlate the debonding with its associated load level.

## 3.5 Durability tests

Four durability tests were conducted to study the effect of different environmental exposures on FRP-concrete bond. Each group of test for durability condition include 3 web-bond samples and 3 dry–bond control samples, all of them undergoing the same durability condition. The four exposure conditions included 100 cycles of freeze/thaw between -17$^{o}$C and +4 $^{o}$C at rate of 5 hr/cycle, 50 cycles of wet/dry at a rate of 12 hr/cycle, 25 days at constant low temperature of -25$^{o}$C dry air and 25 days in hot water at +35$^{o}$C. Their condition setups are shown in Figure.3.6.

After durability exposure, the bond behaviour of samples was evaluated by pullout tests. For each group described in Table 3.6, three concrete cylinders and three FRP laminates were also exposed to the same condition to evaluate their durability.

**Table 3.6: Details of durability conditioning of pullout samples**

| Group number | Specimen reference number | Type of bond | Type of FRP materials | Durability exposure | Exposure period |
|---|---|---|---|---|---|
| 1 | B1D | Dry | 4C | Reference | 0 day |
| 2 | B2W | Wet | 1C+4G | Reference | 0 day |
|  | B2D | Dry | 1C+4G |  |  |
| 3 | B3W | Wet | 1C+4G | low temp. at -25$^{o}$C | 25 days |
|  | B3D | Dry | 1C+4G |  |  |
| 4 | B4W | Wet | 1C+4G | freeze/thaw between -17 $^{o}$C and 4$^{o}$C | 100 cycles |
|  | B4D | Dry | 1C+4G |  |  |
| 5 | B5W | Wet | 1C+4G | hot water at 35$^{o}$C | 25 days |
|  | B5D | Dry | 1C+4G |  |  |
| 6 | B6W | Wet | 1C+4G | wet/dry | 50 cycles |
|  | B6D | Dry | 1C+4G |  |  |

Note: B = bonded sample, W = wet-bond, D = dry-bond,

C = carbon fibre ply, G = glass fibre ply

### i) Freeze/thaw cycling

Freeze/thaw exposure was conducted in an ASTM666 automatic freeze/thaw chamber. Samples for freeze/thaw cycling were put into small containers with bond side facing down in tap water (Figure 3.6). One cycle included 3.2 hours freezing at -17.7$^{o}$C and 1.5 hours thawing up to 4$^{o}$C. Freeze/thaw chamber finished a completed freezing-thaw cycle automatically in 4.7 hours. All the samples underwent 100 cycle exposure (Chajes et al., 1995).

### ii) Wet/dry cycling

Wet/dry cycling exposure was done manually by moving samples in and out of water. For this exposure, a single wet/dry cycle consisted of 8 hours in tap water followed by 4 hours in air drying at room temperature. There were two cycles per day. A 100w lamp was used for drying. Fifty cycles were required for wet/dry condition (Chajes et al., 1995).

### iii) Continuous hot water conditioning

Samples for continuous high temperature plus moisture exposure were immerged in tap water at constant 35°C automatically for 25 days in an oven. After exposure, they were dried in air for pull out test. A thermal couple was used to monitor water temperature, which was constant at 35°C ± 2 °C (Haque et al., 1991).

### iv) Continuous low temperature in dry air

Durability exposure of continuous low temperature was done in a freezer. Samples were conditioned in a freezer at a constant temperature of -25°C for 25 days. A thermal couple was used to monitor temperature.

**(a) Freeze/thaw cycle** **(b) wet/dry cycle**

**(a) 35°C hot water** **(b) -25°C cold air**

**Fig. 3.6: Durability conditions**

Pullout tests of all conditioned samples were carried out in room temperature. Table 3.6 summarizes all pullout samples, including the reference without durability exposure. The thickness of laminate is 1.8 mm and bond length is 200 mm for all samples.

## 3.6 Performance test of epoxy adhesive

To understand the contribution of epoxy adhesive to bond properties, degree of curing (DOC) and glass transition temperature (Tg) of epoxy adhesive were determined using differential scanning calorimeters (TA Instruments Q100, DSC). The Q100 is an expandable module with a 50-position intelligent auto-sampler, and digital mass flow controllers equipped with automatic gas switching capability. The Q100 can be used over the temperature range -180 to 725°C, and offers a wide variety of available high performance accessories.

After pullout test, epoxy adhesive was collected from debonded interface of joint using diamond saw and was cut to standard size for DOC and Tg tests. Besides, fresh mixed epoxy samples cured in air and in water for one week respectively were also tested for comparison.

# Chapter 4 Experimental Results and Discussion

This chapter summarizes the experimental results of tests conducted to study the behaviour and durability of wet-bond between hybrid laminates and cast-in-place concrete. Uni-axial tensile tests of hybrid laminates were conducted to investigate the hybrid behaviour of FRP materials and single lap pullout tests to study wet-bond behaviour and its durability. Four groups of specimens underwent different environmental conditions, while one reference group remained without any exposure. For comparison, load-strain and load-slip curves of each sample were obtained from pullout test and typical failure modes were identified.

## 4.1 Tensile behaviour of hybrid FRP laminates

To investigate the response of carbon fibre and glass fibre in hybrid composite, uni-axial tensile tests of two different kinds of laminates were conducted. One was all-carbon fibre laminate and the other was hybrid laminate consisting of carbon fibre and glass fibre. All-carbon fibre laminate coupons were comprised of either two plies or four plies, and hybrid laminate was consisted of one ply of carbon fibre and four plies of glass fibre (Table 3.4). All laminates were fabricated, cured and tested at room temperature to avoid thermal influence.

### 4.1.1 Material properties of hybrid composites

Figure 4.1 shows typical stress-strain curves of carbon and hybrid laminates in tension. The average carbon fracture strain in hybrid composite was 4000 με that was slightly higher than average fracture strain of 3690 με in all-carbon laminate. On the contrary, average fracture strain of glass fibre obtained from laminates was 15800 με, which was 71.8% of its manufacture's data (Table 3.2). It was likely that the ultimate strain was increased for low elongation fibre and decreased for high elongation fibre in a hybrid composite. Experimental results are summarized in Table 4.1.

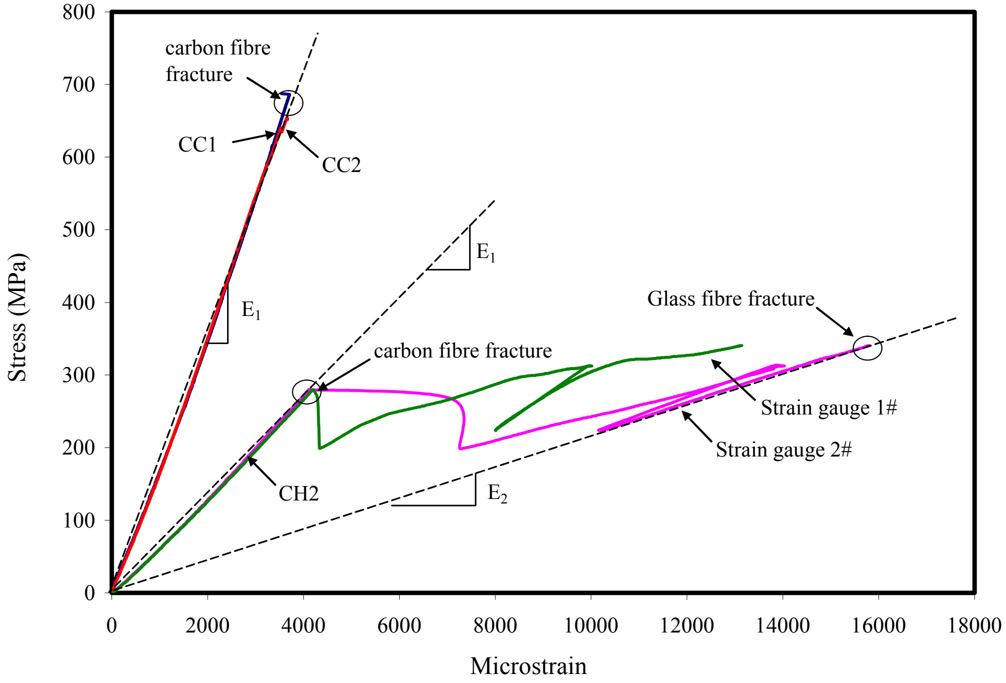

**Fig. 4.1: Tensile behaviour of carbon and hybrid laminates (CC1, CC2 and CH2)**

Note: $E_1$= modulus of laminate before carbon fibre fracture
$E_2$ = modulus of hybrid laminate after carbon fibre fracture.

Figure 4.1 also compares all-carbon laminates with hybrid laminates. It is obvious that modulus of hybrid laminate is only 40% of that of all carbon laminate because of the use of glass fibre (Table 3.2). The comparisons of tests and theoretical calculations by rule of mixture (ROM) are shown in Table 4.1, which illustrates ROM agrees very well with experiments. It is obvious that for all carbon laminate, $E_1$ is constant but for hybrid laminate, $E_1$ was greatly reduced to $E_2$ because of carbon fibre fracture.

Figure 4.1 also shows that behaviour of hybrid composite is more complex than single material. There are three stages representing failure process of hybrid composite, compared to linear elastic behaviour of all-carbon laminate. At first stage, hybrid FRP laminate linearly deformed until ultimate strain of carbon fibre; after carbon fractured, load transferring from carbon fibre to glass fibre caused an instant elongation of glass fibre and induced a temporary load drop; finally, reloading took place and laminate deformed until glass fibre fracture.

**Table 4.1: Properties of carbon and hybrid laminates**

| Sample | Type of laminate | Experiment | | | | | | ROM | |
|---|---|---|---|---|---|---|---|---|---|
| | | $\varepsilon_{ca}$ ($\mu\varepsilon$) | | $\varepsilon_{gl}$ ($\mu\varepsilon$) | | $E_1$ (GPa) | $E_2$ (GPa) | $E_1$ (GPa) | $E_2$ (GPa) |
| | | | Ave. | | Ave. | | | | |
| CC1 | 2C | 3711 | 3690 | - | - | 172 | - | 174 | - |
| CC2 | 4C | 3670 | | - | | 171 | - | 174 | - |
| CH1 | 1C+4G | 4307 | 4000 | 15812 | 15798 | 63.2 | 21.6 | 65.9 | 23 |
| CH2 | 1C+4G | 4114 | | 15806 | | 68.3 | 24.9 | 65.9 | 23 |
| CH3 | 1C+4G | 3578 | | 15776 | | 64.6 | 22.2 | 65.9 | 23 |

Note: $\varepsilon_{ca}$ = ultimate strain of carbon fibre, $\varepsilon_{gl}$ = ultimate strain of glass fibre

### 4.1.2 Post-carbon crack behaviour of hybrid FRP laminate

It was noted that laminate at different points from crack plane was stretched differently after carbon fracture. Three hybrid FRP laminates were examined with each one having two strain gauges glued on glass fibre side spacing 45 mm to monitor tensile strain of glass fibre at different distance from carbon crack. Typical load-strain curves of laminate CH2 are shown in Figure 4.2 and load-time curves in Figure 4.3.

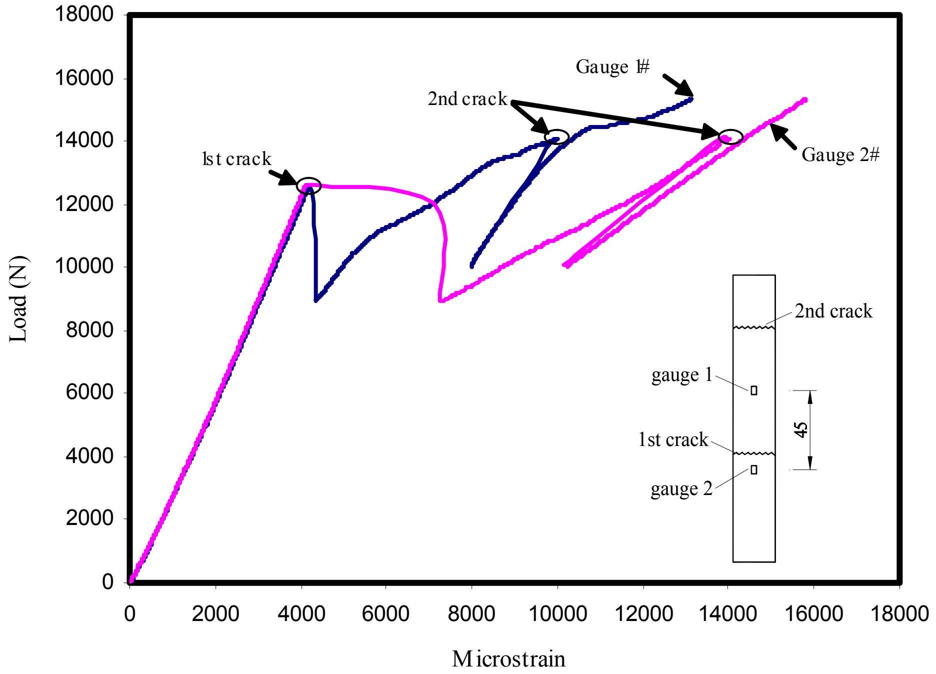

Fig. 4.2: Effect of distance from crack plane on strain (CH2)

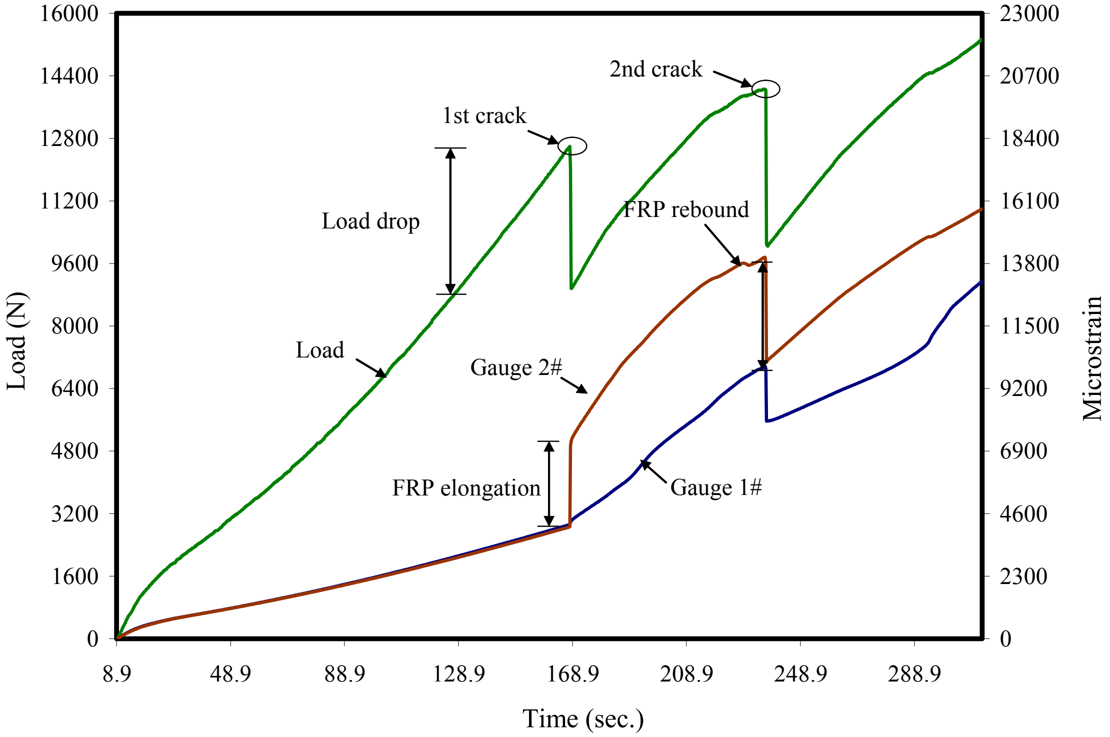

Fig. 4.3: Typical failure process of hybrid laminates (CH2)

Load-strain curves in Figure 4.2 and failure process recorded by time in Figure 4.3 display the whole failure process as well as the tensile strain change in hybrid composite. Firstly, carbon fibre and glass fibre deformed linearly and shared tensile force by ROM until carbon fracture. When deformation of laminate reached carbon strain limit of about 4000με, first crack occurred with the bursts of acoustic emission. At fracture plane, the stress originally carried by carbon fibre was shifted to glass fibre, causing instant elongation of glass fibre, which is shown as a plateau of curve for strain 2 in Figure 4.2 and sudden increase in Figure 4.3. At the same time, strain 1 only experienced a load drop without elongation. Strain 2 recorded the elongation of glass fibre because it was much closer to crack plane than gauge 1 (Figure 4.2).

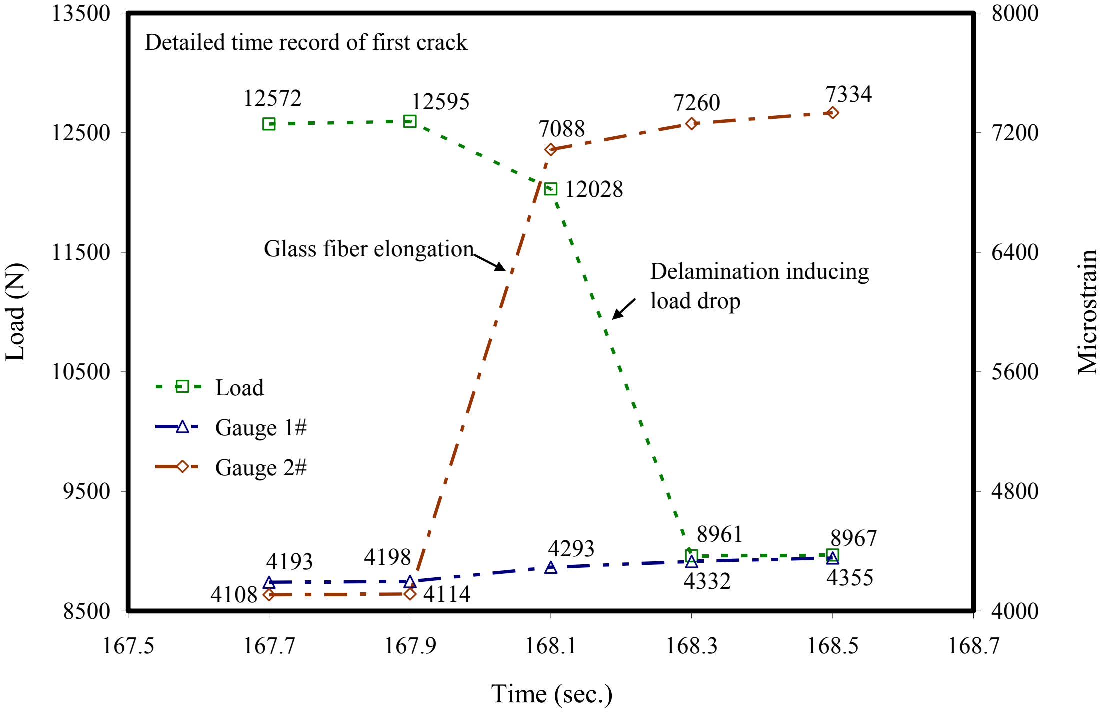

**Fig. 4.4: Instantaneous response of hybrid laminate at first carbon fracture (CH2)**

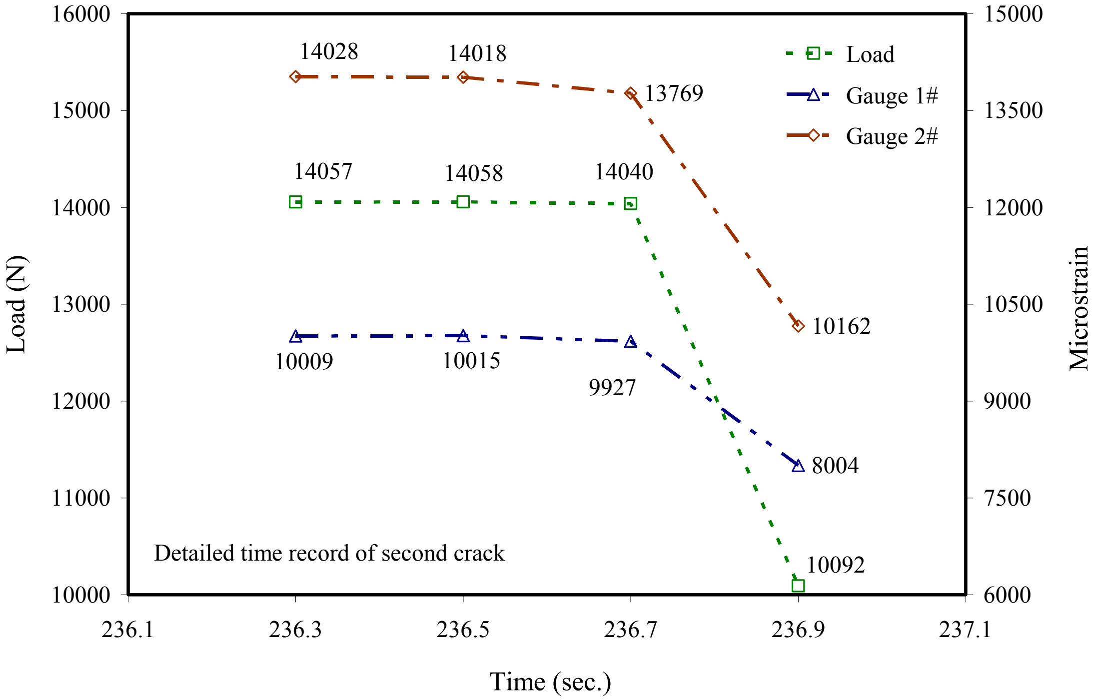

**Fig. 4.5: Instantaneous response of hybrid laminate at second carbon fracture (CH2)**

Because glass fibre elongation and load dropping happened within very short period of time, it is hard to distinguish which one happened first by observation and only data recorded in detail can tell the sequence. Figure 4.4 shows that reading of strain gauge 2 suddenly changed from 4198 to 7088 within 0.2 second followed by load dropped from 12028 N to 8961 N in next 0.2 second.

After first carbon fracture, it was noted that when the load was continued to increase, the second crack of carbon fibre occurred, leading to a multiple cracking. It is worth to mention that carbon fibre between two crack planes had the trend to spring back because it had no constrain at ends. Figure 4.5 is the instantaneous record of hybrid laminates at second carbon fracture, which shows both load and strains were dropped.

## 4.2 Dry-bond behaviour of hybrid laminates to hardened concrete

In order to compare the bond behaviour of hybrid composite and hardened concrete, dry-bond samples were prepared and pullout tests were conducted. Typical load-strain curves of all-carbon laminates and hybrid laminates are plotted in Figure 4.6 and typical load-slip curves are given in Figure 4.7. Experimental results are summarized in Table 4.2.

Figure 4.6 shows that there are no bend over points at load-strain curves of both uni-axial tensile test and pullout test for all-carbon laminate (CC2 and B1D2) while both curves for hybrid laminates have obvious plateaus, which represents load transfer and glass fibre elongation process after carbon fracture and distinguishes the typical behaviour of hybrid composite material.

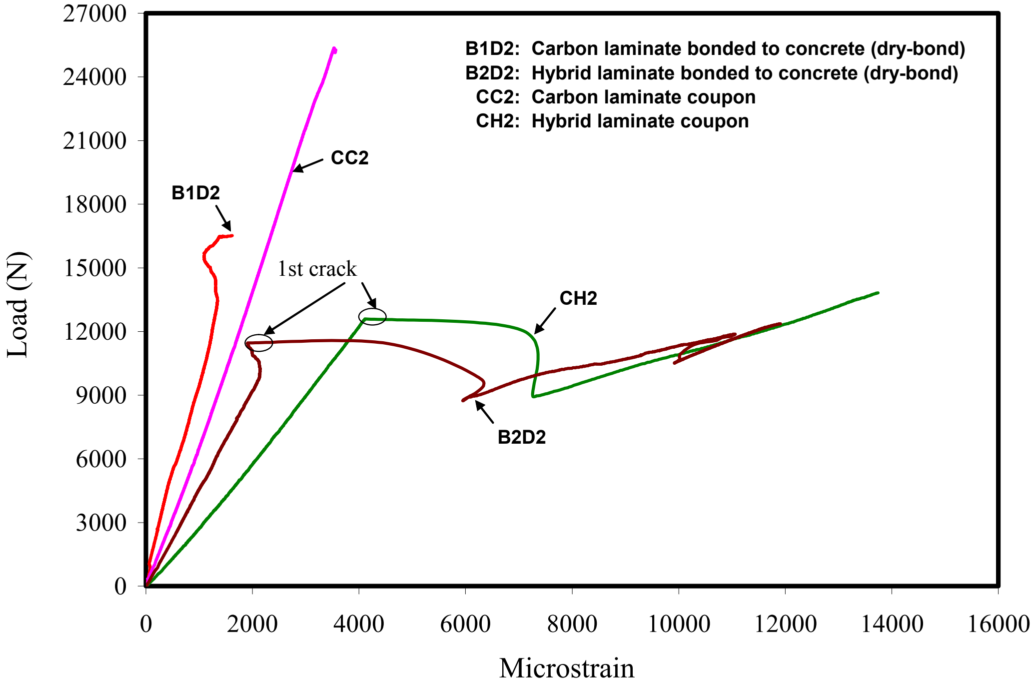

**Fig. 4.6: Comparison of load-strain curves of tensile tests and pullout tests**

It is noted that either for all-carbon laminate (B1D2 & CC2) or hybrid laminate (B2D2 & CH2), the strain of uniaxial tensile test is larger than that of the pullout test under the same load level. The difference is more apparent for hybrid laminate because of the lower modulus and larger deformation of hybrid composite. As regarding the carbon fracture strains of hybrid laminate, it was approximately 4000 με in uniaxial coupon test but only around 2000 με in pullout tests. This could be explained as that for hybrid laminate bonded with concrete, partial pullout force was transferred to concrete by adhesive joint and the tensile strain of bonded laminate was definitely smaller than the one unbonded. It was likely carbon fibre fracture occurred outside bonded area.

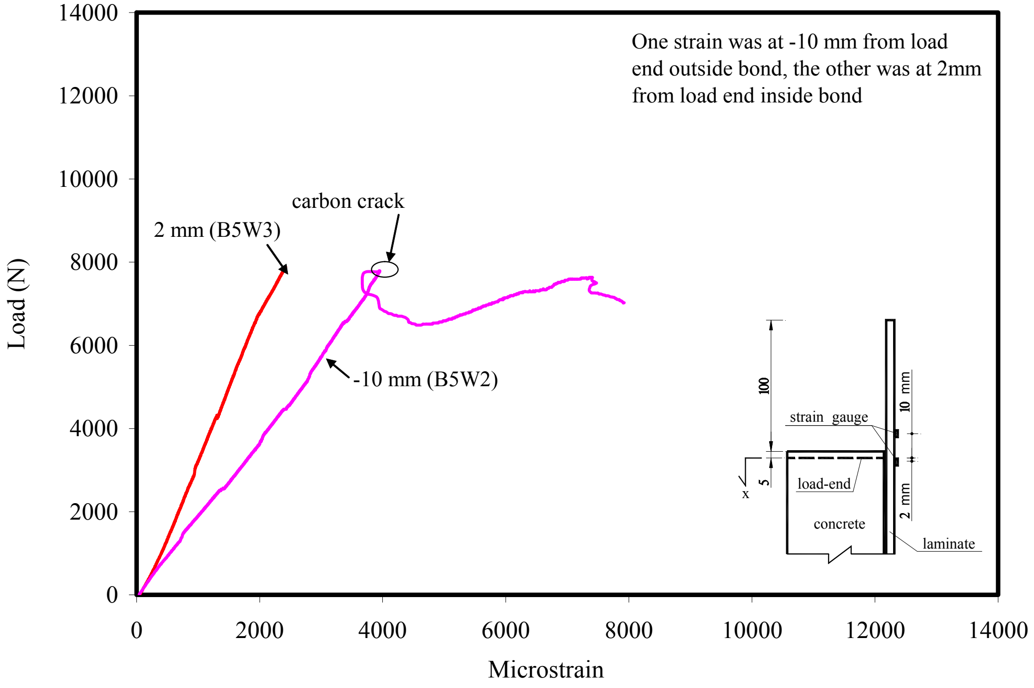

**Fig. 4.7: Comparison of bonded and unbonded behaviour**

To confirm the observation, two more pullout tests with wet-bond from same group (B5W2, B5W3) were carried out with strain gauges placed at different location for comparison. Figure 4.7 shows the strain curves recorded at gauge of 2mm inside bond and of 10mm outside bond from load end respectively. The two curves suggested that the tensile strain of laminate outside bond area was larger than that of inside one from very beginning. When load increased to cause carbon fracture at 4000 με of laminate outside bond (–10mm gauge), the bonded laminate (2 mm gauge) had strain only around 2000 με.

Relative slip between concrete and laminate was measured by LVDT during pullout test. Figure 4.8 compares load slip curves of typical all-carbon fibre with hybrid composite pullout samples. It was apparent that hybrid sample failed at lower load level than all-carbon sample, but its total slip was much larger. Within elastic linear stage, there was not much difference of slips until carbon fracture in hybrid laminate. The sudden increase of slip in hybrid was attributed to glass fibre elongation. In addition, lower modulus of hybrid material could potentially cause larger deformation that facilitated high ductility and energy absorption capacity.

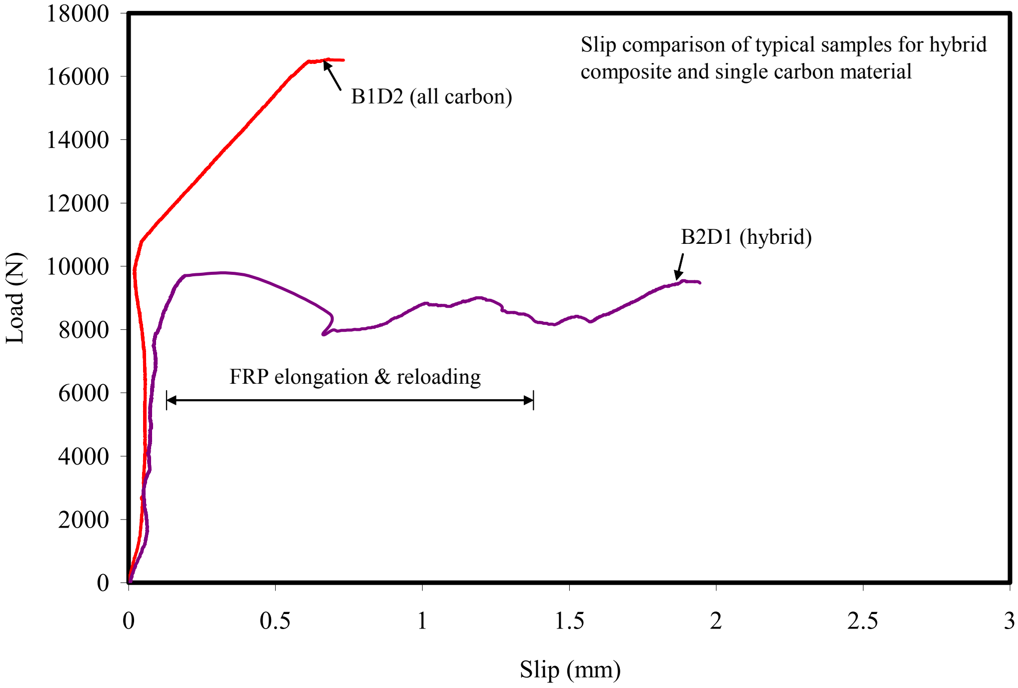

**Fig. 4.8: Typical load-slip curves of carbon and hybrid laminate pullout tests**

**Table 4.2: Comparison of tensile test coupons and pullout dry-bond samples**

| Sample | Materials | Test | Carbon fracture | | Peak load | |
|---|---|---|---|---|---|---|
| | | | Strain (με) | Load (N) | Strain (με) | Load (N) |
| CC | 4C | Tensile | - | - | 3710 | 25931 |
| B1D | 4C | Pullout | - | - | 1704 | 16682 |
| CH | 1C+4G | Tensile | 4114 | 12595 | 15806 | 15328 |
| B2D | 1C+4G | Pullout | 2453 | 9607 | 7550 | 11562 |

Note: the strain and load is the average value

## 4.3 First crack load and failure modes

Most of all previous studies on bond between FRP and concrete were about single FRP materials (either carbon fibre or glass fibre) bonded to hardened concrete. Their typical failure mode was debonding at concrete substrate. In this project, more complex failure modes were observed because of hybrid composite was involved and two different types of bond methods were introduced. In addition, different environmental exposures could also have effect on failure behaviour. Classification of failure modes was based on the load-strain curves at load end (2 mm from load end) and the whole process recorded by video taping. Because debonding always started from load end and propagated toward free end, 2 mm strain gauge was the most sensitive one to detect initial debonding.

According to occurring sequence, there are two key points controlling the failure process based on experimental data and video analysis. First one is called first crack load, which can be carbon fibre fracture load or initial debonding load; the second one is peak load, the highest load of the entire process. It is worth to mention that for some samples, initial debonding point was not very obvious in load-strain or load-slip curves, it was determined in combination with video image visualization. Three failure modes were identified directly from experimental results:

- Failure mode I: carbon fibre fracture followed by glass fibre elongation and total debonding

- Failure mode II: initial debonding between laminate and concrete followed by carbon fibre fracture, glass fibre elongation and total debonding
- Failure mode III: progressive debonding without carbon fibre fracture

Results of wet-bond samples under pull-out test are summarized in Table 4.5 for reference and four environmental conditions while results of dry-bond samples under pull-out tests for same condition are summarized in Table 4.6.

### 4.3.1 Failure mode I

Failure mode I is defined as initial debonding load larger than or equal to carbon fibre fracture load. Schematic failure sequence is shown in Figure 4.9. The failure starts with carbon fibre fracture at ultimate strain of carbon fibre under $P_1$ and followed by a glass fibre elongation to $\varepsilon_2$ accompanied with a load drop to $P_3$ and a reloading until total debonding at $P_4$. All of reference dry-bond samples without environmental exposure failed in this type of mode (Table 4.6).

In this mode, FRP hybrid laminate was well bonded with concrete and bond stress was developed (Chen and Teng, 2001) until carbon fibre fracture. Based on previous research, the tensile force of bonded laminate was distributed nonlinearly along effective length and maximum tensile stress in the FRP laminate occurred outside the bond area. Experiments had shown that almost in all cases of failure mode I, carbon fibre fracture happened in unbonded laminate close to load end (Table 4.6), meanwhile the bonded laminate had much smaller strain because of the contribution of concrete. This phenomena has been discussed in Section 4.2 and it is responsible for first strain gauge's reading of observed approximately 2000 $\mu\varepsilon$ which is much smaller than its ultimate strain of 4000 $\mu\varepsilon$ when carbon fibre fractured.

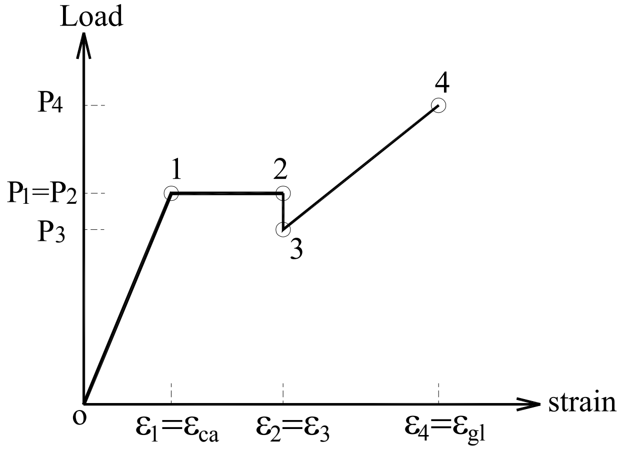

**Fig. 4.9: Schematic sequence of failure mode I**

Note: $P_1$ = carbon fracture load, $P_2$ = load after glass fibre elongation, $P_3$ = load after temporary load drop, $P_4$ = ultimate load, $\varepsilon_{ca}$ = ultimate strain of carbon fibre, $\varepsilon_{gl}$ = ultimate strain of glass fibre, $\varepsilon_d$ = tensile strain of laminates at initial debonding, $\varepsilon_1$ = tensile strain of laminate at carbon fracture, $\varepsilon_2$ = tensile strain of laminate after glass fibre elongation, $\varepsilon_3$ = tensile strain of laminate at load drop, $\varepsilon_4$ = strain of laminate at ultimate load

Carbon fibre cracking caused energy release accompanied with an acoustic emission and sudden elongation of glass fibre and a corresponding large slip and initial debonding were induced within a very short period of time. Since debonding starts after carbon fibre fracture and modulus of hybrid laminate was reduced, there is no obvious bend-over to distinguish the initial debonding point on load-strain curve. During reloading period, debonding propagated and active bond zone shifted to free end. Combined video and time recording, curves of load-strain and load-slip relation clearly display the whole process of failure mode I. Typical curves of load-strain, load-slip and time recording from sample B2D1 are shown in Figure 4.10.

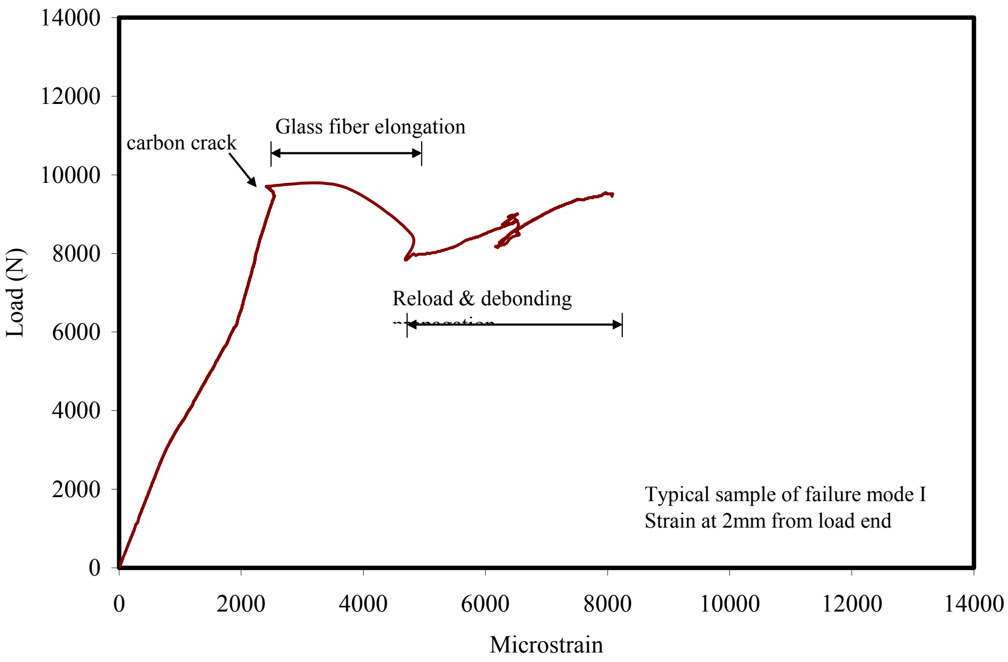

**(a) load-strain curve**

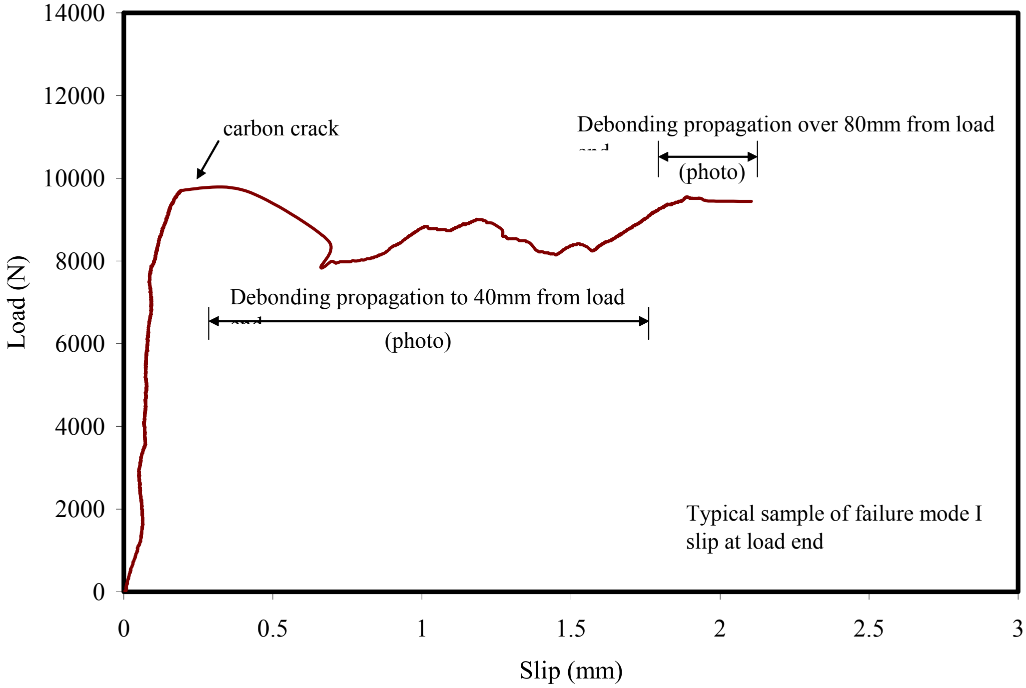

**(b) load-slip curve**

**Fig. 4.10: Typical sample of failure mode I (B2D1)**

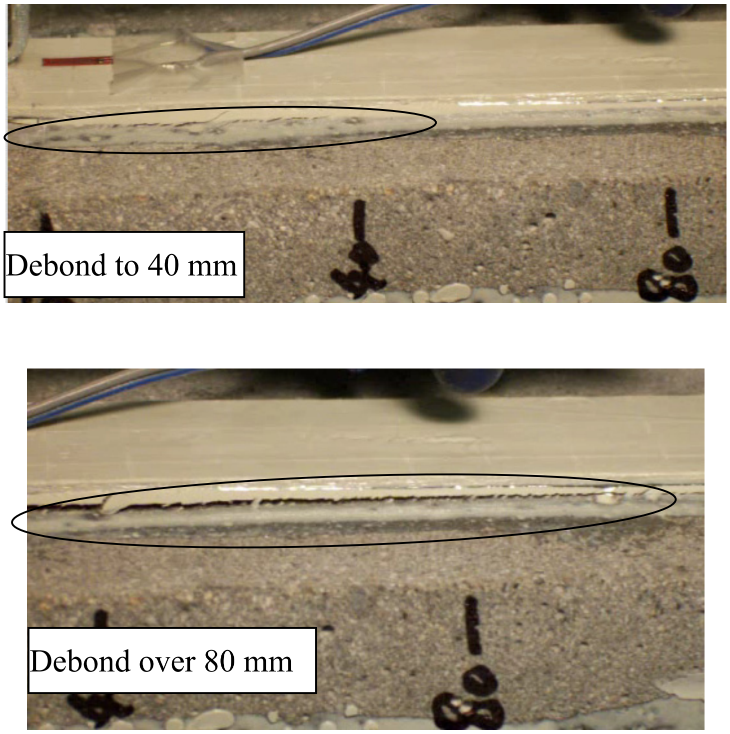

**(c) photos of debonding propagation**

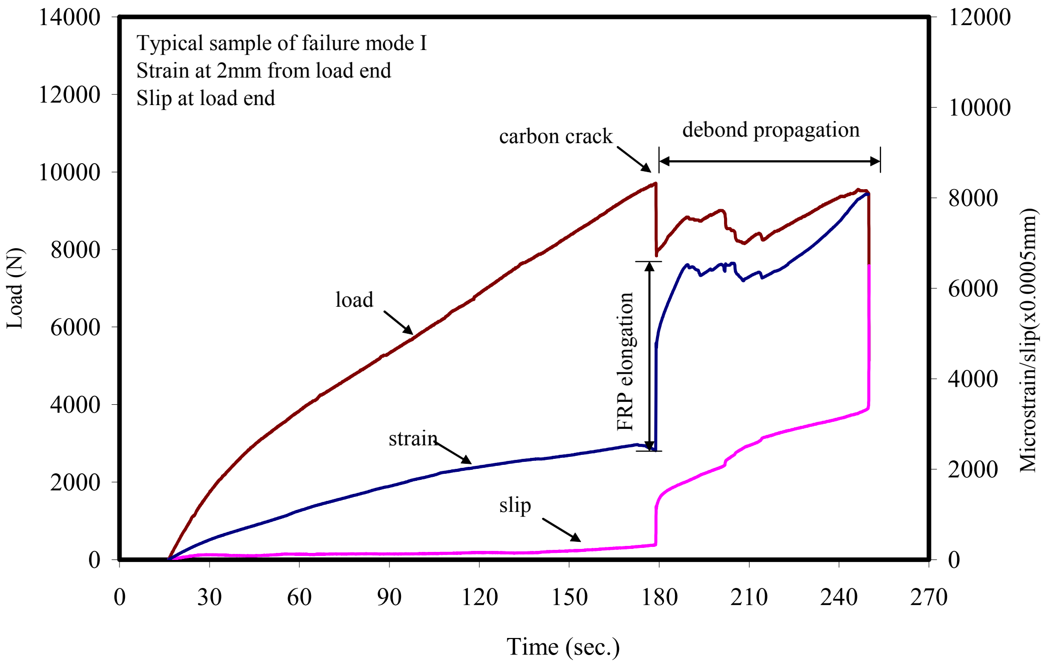

**(d) time recording**

**Fig. 4.10 (con't): Typical sample of failure mode I (B2D1)**

### 4.3.2 Failure mode II

Failure mode II is defined as carbon fibre fracture after initial debonding. Schematic failure sequence is shown in Figure 4.11. In this mode, failure starts with debonding initiation at load $P_d$ followed by carbon fibre fracture at ultimate strain of carbon fibre at $P_1$, glass fibre elongation to $\varepsilon_2$ accompanied by load drop to $P_3$ and total debonding happens at ultimate load $P_4$. Most of samples of wet-bond and dry-bond exposed to continuous low temperature, freeze/thaw cycles, continuous hot water immersion failed in mode II (Table 4.5 and 4.6).

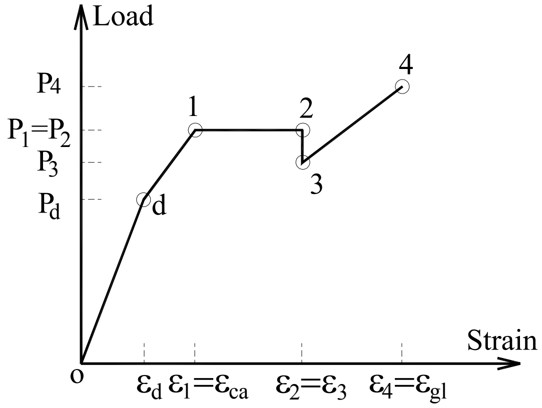

**Fig. 4.11: Schematic sequence of failure mode II**

Note: $P_d$ = initial debond load, $\varepsilon_d$ = tensile strain of laminates at initial debond

Mode II and Mode I have opposite sequence. Mode II undergoes debonding first and carbon fibre fracture after. In mode II, after initial debonding, debonded part of laminate carried the whole force and deformed like a coupon in tension. Load continuously increased causing carbon fibre fracture followed by glass fibre elongation and temporary load drop. During following reloading process, active bond area shifted to free end until total debonding failure.

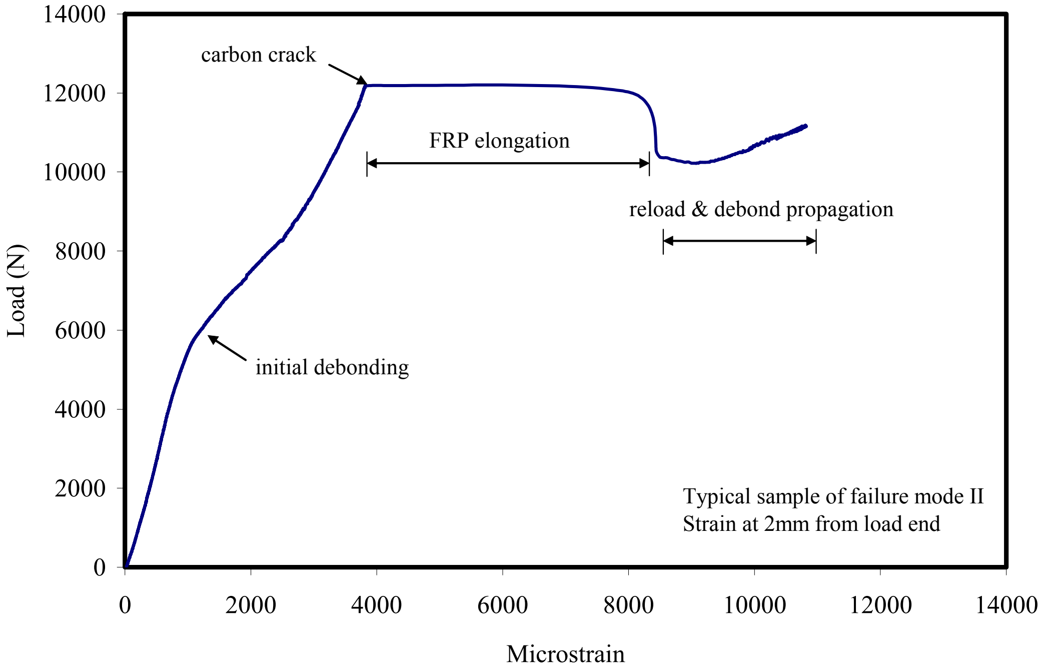

**(a) load-strain curve**

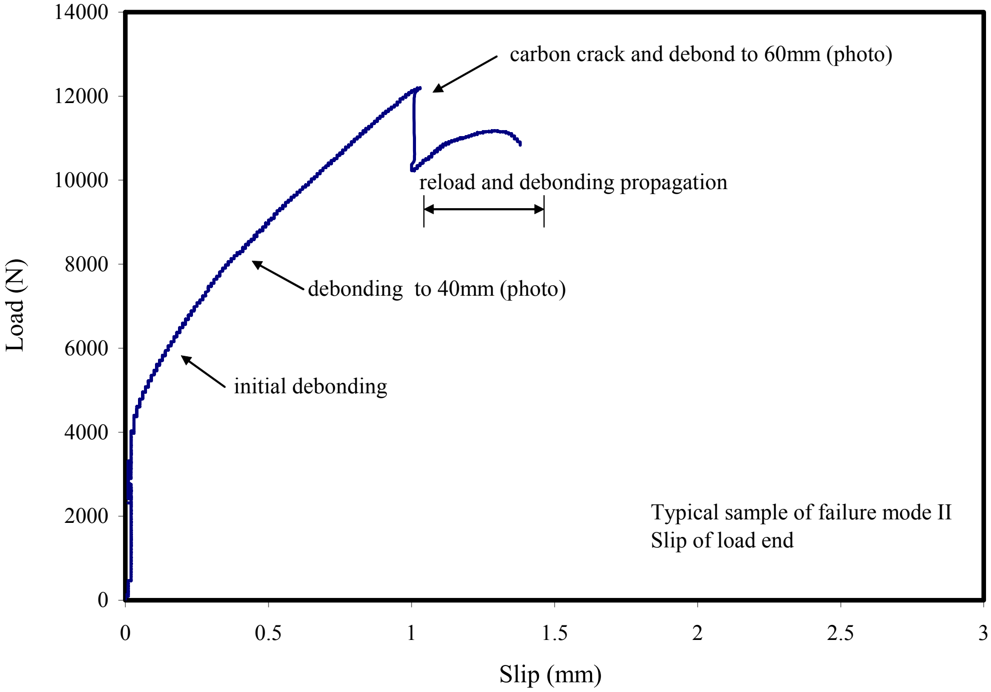

**(b) load-slip curve**

**Fig. 4.12: Typical sample of failure mode II (B4W3)**

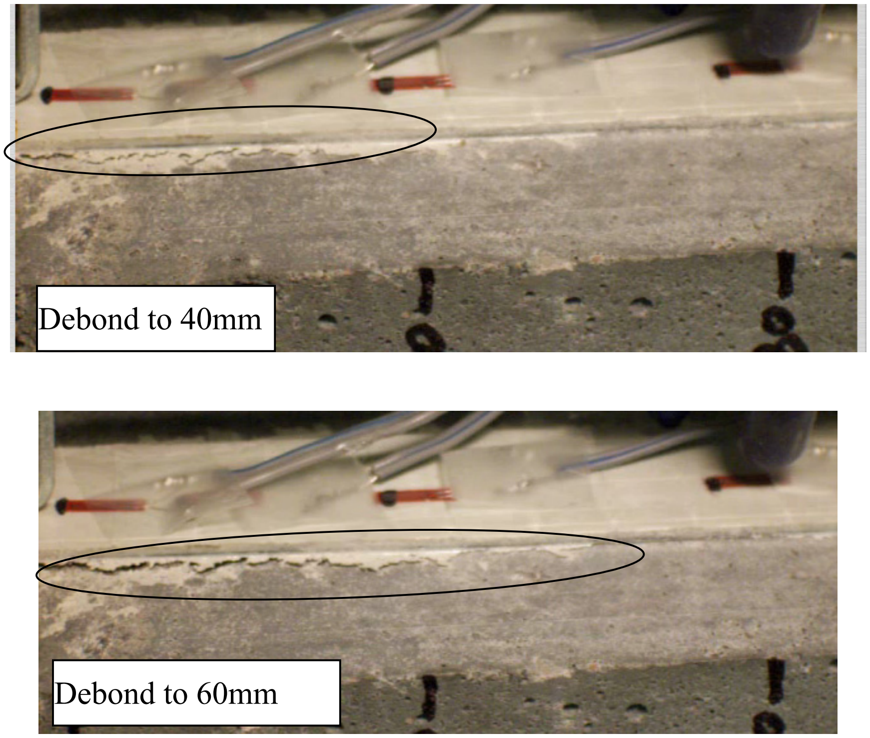

**(c) photos of debonding propagation**

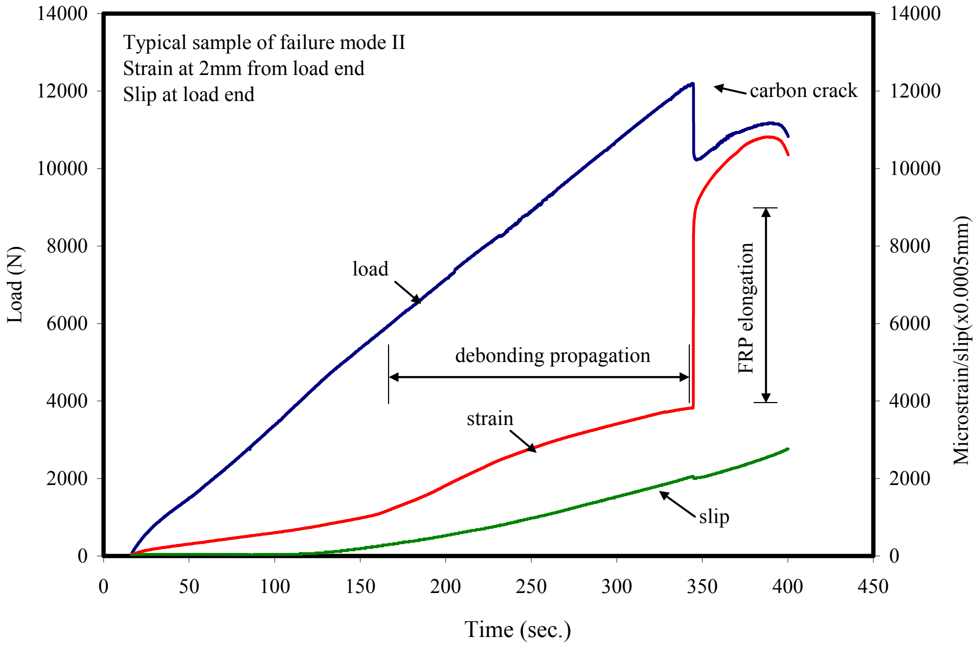

**(d) time recording**

**Fig. 4.12 (con't): Typical sample of failure mode II (B4W3)**

It was noted that because initial debonding occurred before carbon fibre fracture, the position of carbon fibre crack could be within the debonded zone and the ultimate tensile strain of carbon fibre of debonded part was the same as coupon test, which is around 4000$\mu\varepsilon$. Examination of all 20 samples that failed in mode II shows that first carbon fracture was within debonded zone for 17 samples while other samples had crack at load end (Table 4.5, 4.6). Typical curves of load-strain, load-slip, photos of debonding propagation and time recording from sample B4W3 are shown in Figure 4.12.

### 4.3.3 Failure mode III

Failure mode III is the simplest mode because there was no carbon fibre fracture during the whole process and the failure sequence starts with initial debonding at $P_d$ and ends by total debonding at load $P_4$. Most wet-bond samples from reference group and wet-bond samples with 50 wet/dry cycles exposure failed in mode III.

For these cases, the ultimate debonding load was general peak load because bond is not strong enough to cause carbon fibre fracture. Schematic failure sequence is shown in Figure 4.13. At ultimate failure, the total strain developed in the FRP is still smaller than the ultimate tensile strain of carbon fibre. Typical curves of load-strain, load-slip and time recording from sample B2W2 are shown in Figure. 4.14.

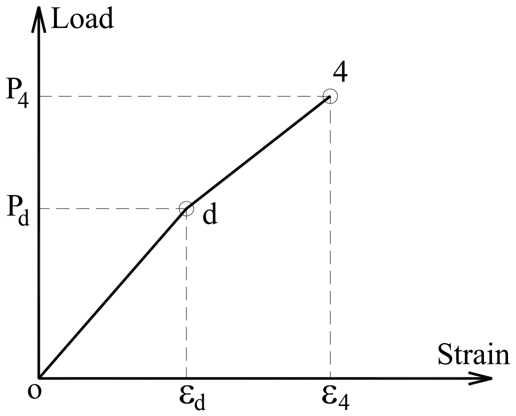

**Fig. 4.13: Schematic sequence of failure mode III**

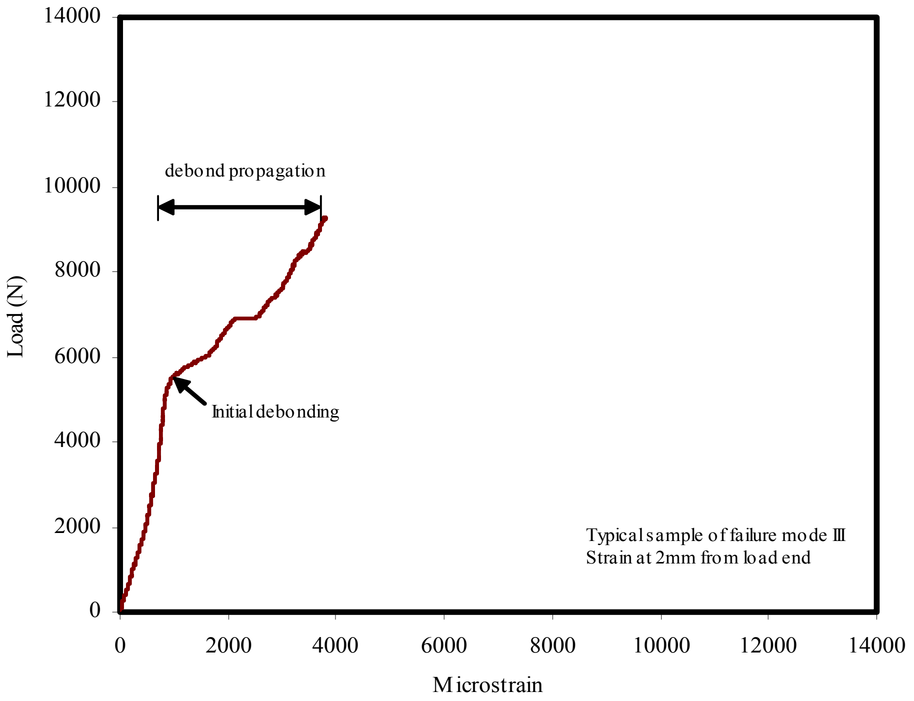

(a) load-strain curve

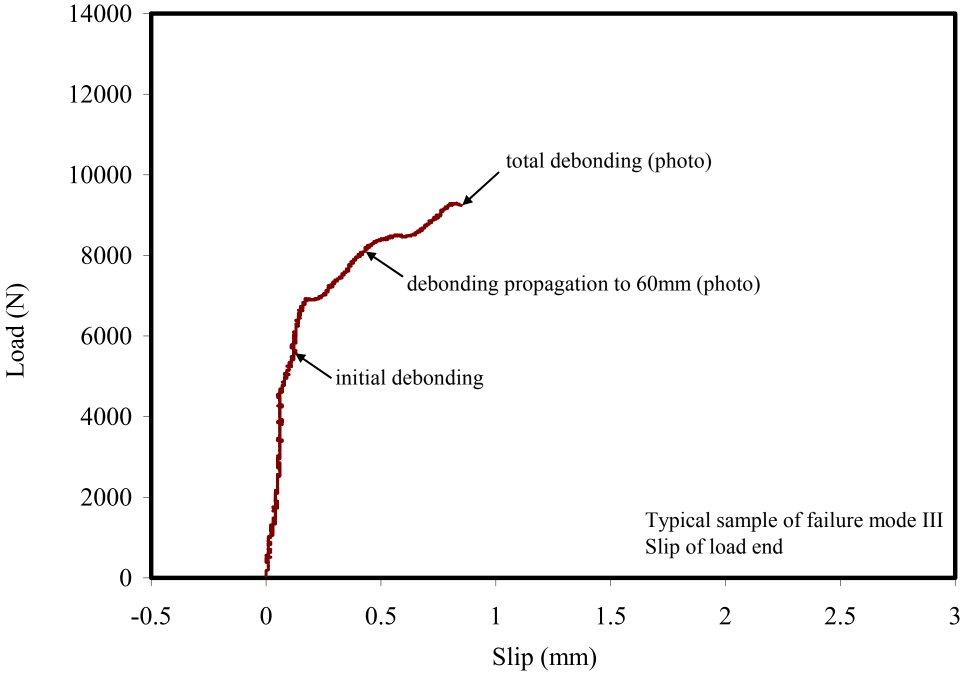

(b) load-slip curve

Fig. 4.14: Typical sample of failure mode III (B2W2)

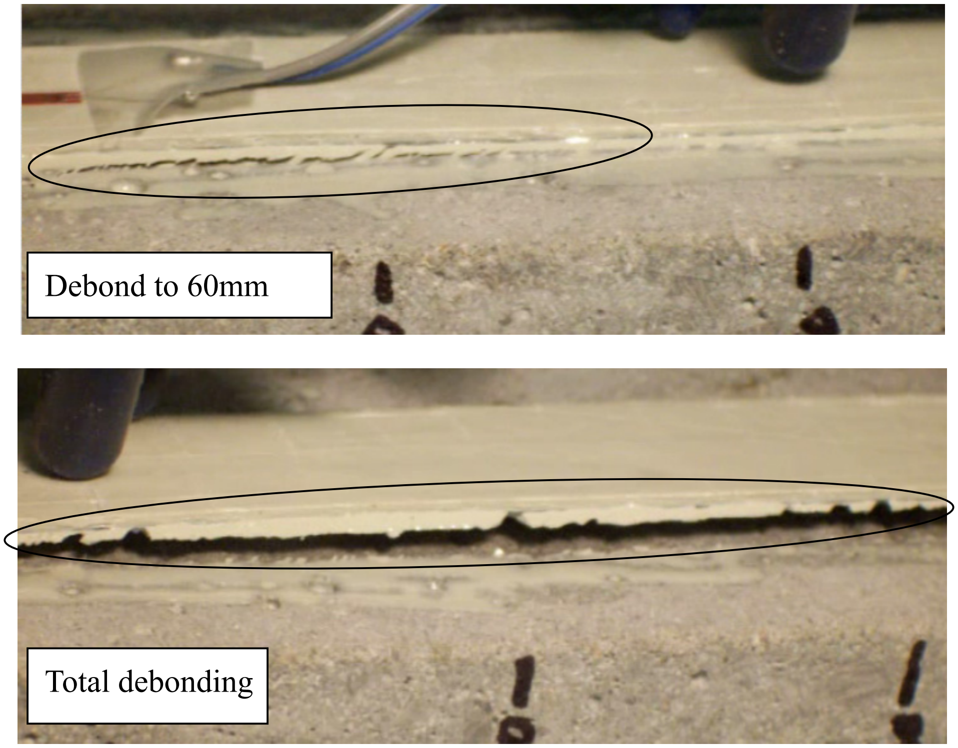

**(c) photo of debonding propagation**

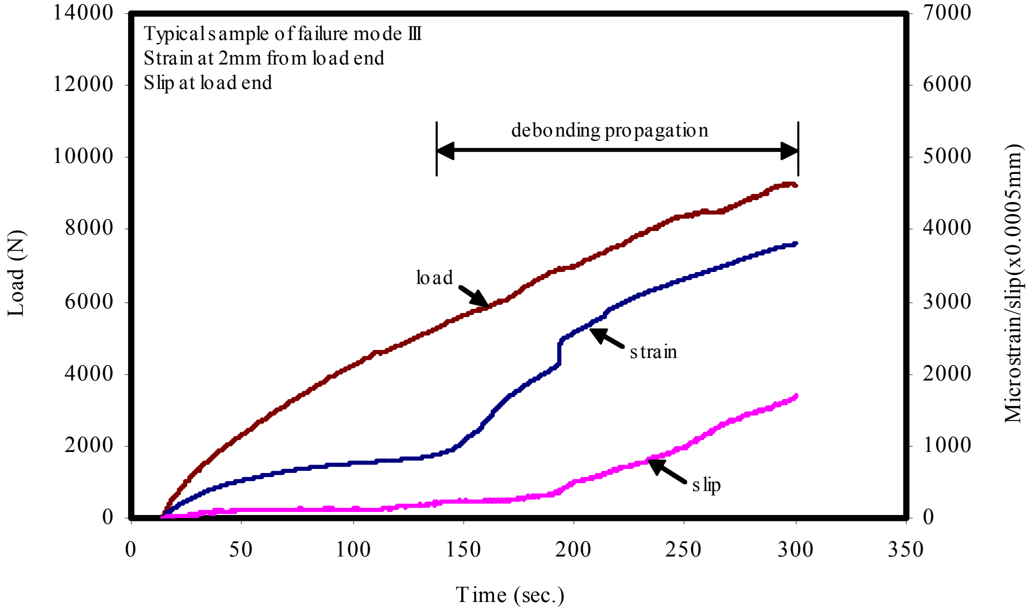

\

**(d) time recording**

**Fig. 4.14 (con't): Typical sample of failure mode III (B2W2)**

## 4.4 Wet-bond of hybrid laminates with cast-in-place concrete

### 4.4.1 Wet-bond behaviour

Figure 4.15 shows load-strain curves at different positions along laminate bonded to cast-in-place concrete (wet-bond B2W2). Figure 4.15 shows that strain near the load end was slightly larger than that at 40 mm away. Related to non-linear tensile distribution along bonded laminate, three strains were distinguished from beginning of loading. When load reached about 6 kN, there was an apparent bend-over at 2 mm curve which indicates debond was likely to occur. Once debonding began, it propagated toward free end and reached 80 mm plane quickly, which is supported by bend-over of 80 mm curve at 7kN. For wet-bond samples without environmental exposure no obvious carbon fracture happening and the sample failed at a strain smaller than ultimate strain of carbon fibre.

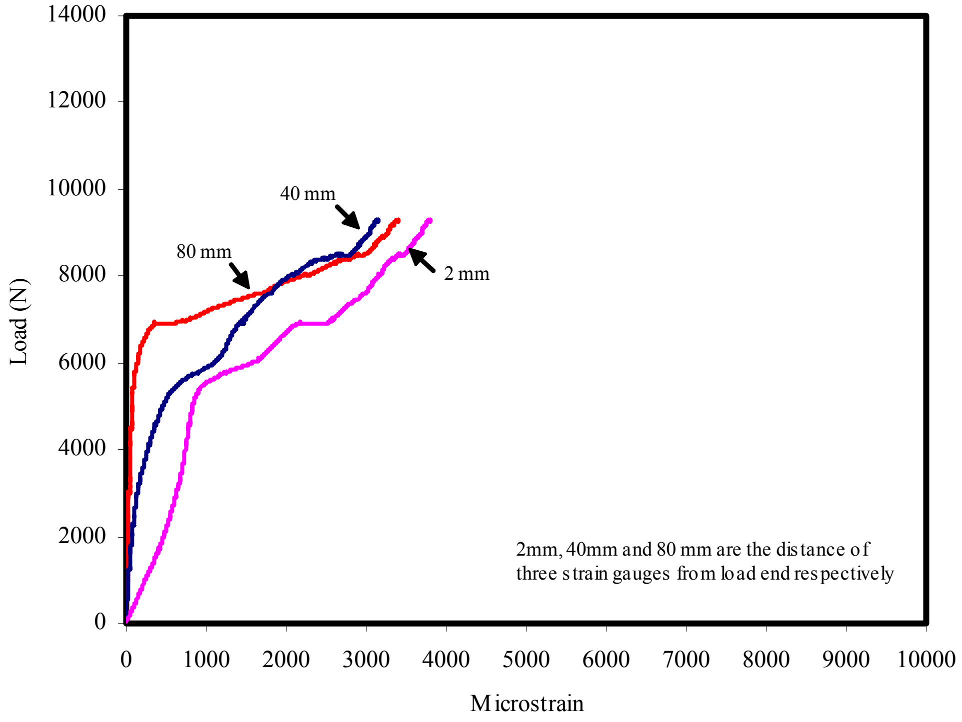

**Fig. 4.15: Typical load-strain curves of wet-bond (B2W2)**

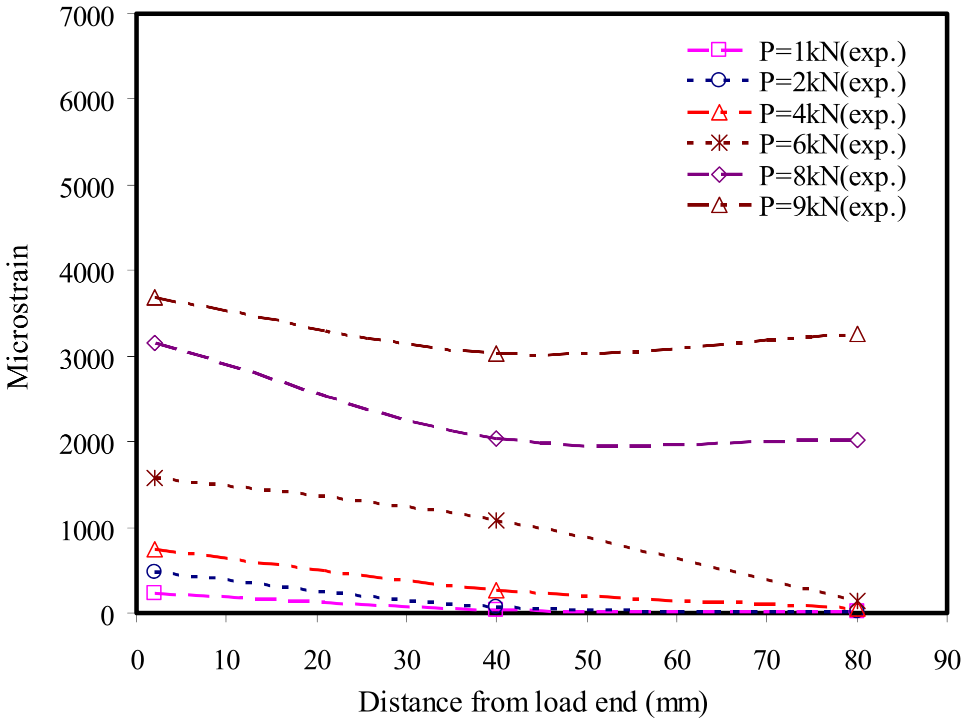

**Fig. 4.16: Typical strain distribution of wet-bond (B2W2)**

Figure 4.16 demonstrates the typical strain distributions of the same wet-bond laminate (B2W2), which shows that tensile strain of hybrid laminates decreased slightly from load end to free end when load level was lower than 6kN. During initial loading period (P ≤ 4kN), tensile strain near load end increased slowly and there was approximately no strain far away from the point from loaded end. When load was up to 6kN, the tensile strain at the 0 mm and 40 mm position augmented significantly, but at 80 mm it still remained about zero, which implies laminate was bonded with concrete very well at load level. On the contrary, fast increasing of strain near load end indicated the initial debonding has passed over 2 mm and propagated to further position. Under higher load level, the strain at 80 mm was almost equal to the one at 40 mm, which clearly illustrates the active zone has likely shifted to the area passing 80 mm point.

### 4.4.2 Wet-bond mechanism

Previous research indicates that dry-bond strength is mainly provided by adhesive bond strength and tensile strength of concrete substrate. In this project, it was discovered that besides the above two bond mechanisms, the bond strength of web-bond is more dependent on mechanical interlock action between adhesive and concrete aggregates. For wet-bond technology, concrete is cast when the adhesive resin is still a viscous state and could displace freely under the gravity load of aggregates. Gravity and vibration caused aggregates to move downwards into the epoxy adhesive and to displace the resin upwards over the aggregates. After epoxy and concrete were hardened, squeezed epoxy adhesive interconnect with embedded aggregates providing an interlocking strength.

The interlock mechanism was illustrated by investigating wet-bond interface after pullout test shown in Figure 4.17. A schematic drawing in Figure 4.18 also shows the fractured interface and bond mechanism of wet-bond. From Figure 4.17, it was likely the bond was separated at the interface between aggregates and epoxy adhesive. Less cementitous materials were attached on the surface of epoxy adhesive, which indicates relative weak adhesive bond between the epoxy adhesive and the concrete. On the contrary, the serrated surface of epoxy illustrated the interlock action between epoxy adhesive and aggregates.

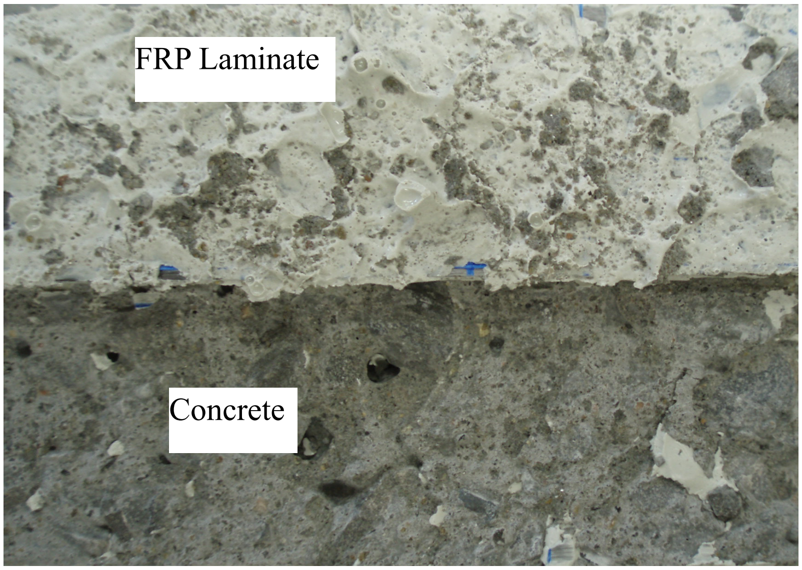

**Fig. 4.17: Typical wet-bond interface (after pullout test)**

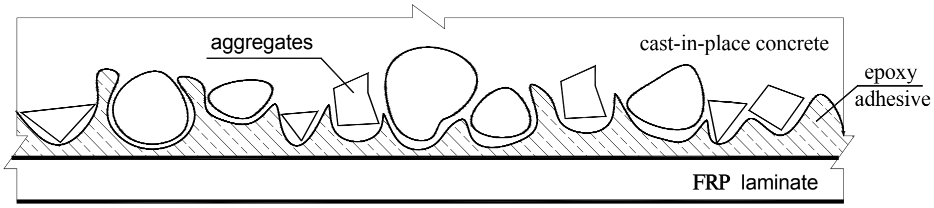

**Fig. 4.18: Schematic wet-bond mechanism**

### 4.4.3 Comparison of wet-bond with dry-bond

**(1) Behaviour of dry-bond**

Figure 4.19 shows load-strain curves at different position along laminate which is bonded to hardened concrete (dry-bond B2D4). It shows that at initial stage, strain reading near the load end (2 mm) was significantly larger than that of the other two strain gauges that indicates good bond between the laminate and the concrete due to the rapid decrease in tensile force. When load increased to around 13 kN, the apparent bend-over of 2 mm curve combined with temporary load drop indicates carbon fibre fracture, which is the typical behaviour of hybrid materials. In addition, load drop was observed only in the curve of 40 mm because it was away from fracture plane (carbon fibre crack at 0 mm). It is noticed that the small change of strain at 80 mm before carbon crack implies good bond at this point. During reloading period, sudden augment of strain at 80 mm demonstrated progressive debonding towards free end.

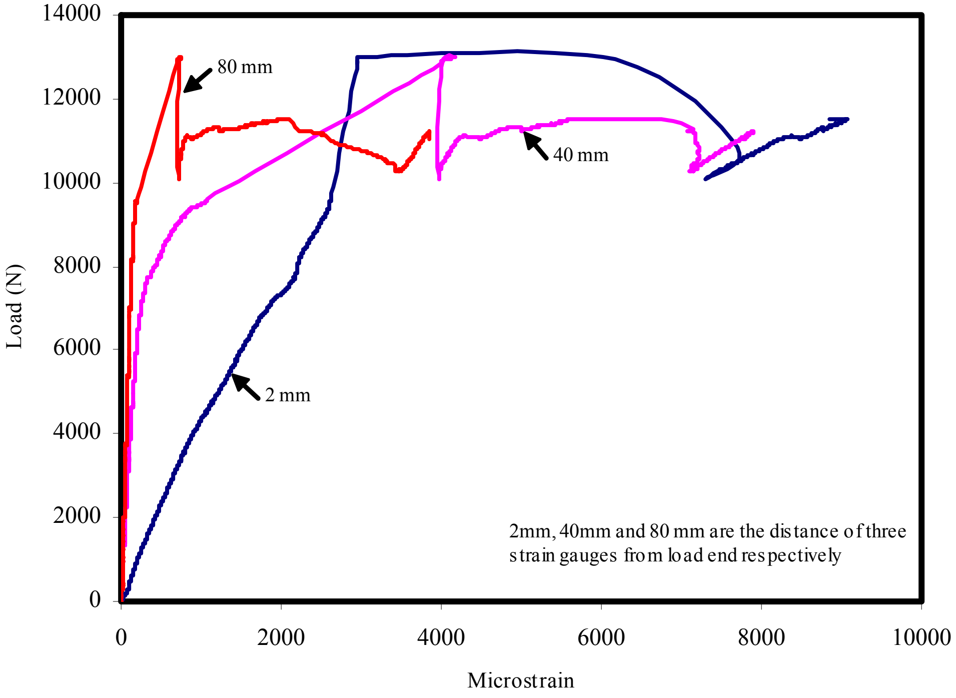

**Fig. 4.19: Typical load strain curves for dry-bond (B2D4)**

Recalling that for typical dry-bond without any environmental exposure, carbon fibre fracture occurred first at about 2000 με of 2 mm strain gauge (failure mode I). Good dry-bond quality not only depends on adhesive strength but also on sound concrete substrate. If the concrete substrate is not strong enough, micro-crack in concrete possibly occurred during loading inducing earlier increase of tensile strain in laminates at weak position.

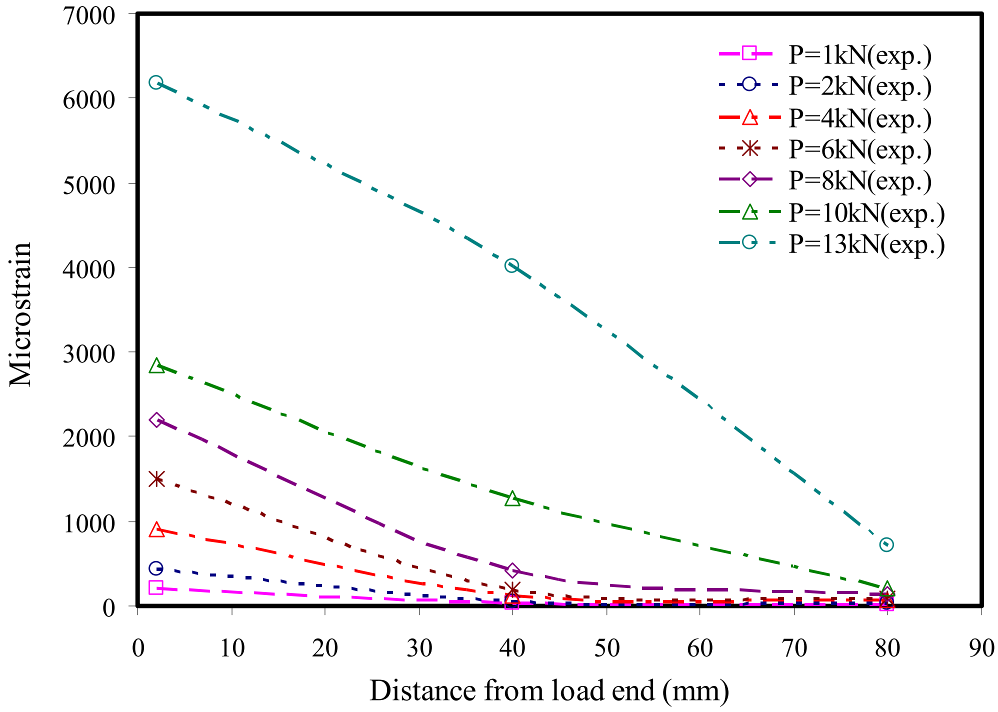

**Fig. 4.20: Typical strain distribution for dry-bond (B2D4)**

Figure 4.20 shows the typical tensile strain distributions at different position of dry-bond (B2D4). Comparing the curves, the tensile strain at load end (2 mm) was always the largest one and it decreased gradually towards free end. Gauge at 80 mm exhibited near zero strain, indicating that shear stress was developed in the vicinity of load end and it reduced quickly along the effective bond length. When load increased from 8 kN to 10 kN, the strain at 40 mm was considerably increased, indicating the micro-crack in concrete substrate had developed. It is necessary to clarify that micro-crack is not the debonding between adhesive and concrete. There was no visible debonding crack monitored by a video taping, until the load reached 13 kN, where carbon fibre fracture occurred, glass fibre stretching and load drop were observed.

It is noted that under load 13 kN, there is a sudden increase in strain at 2 mm and 40 mm caused by carbon fracture and progressive debonding. The shear strain estimated by the tensile strain along laminate became 5000με between gauges at 2 mm and 40 mm and 2500με between 40 mm and 80 mm, which was indicative of debonding propagation and active bond zone shift.

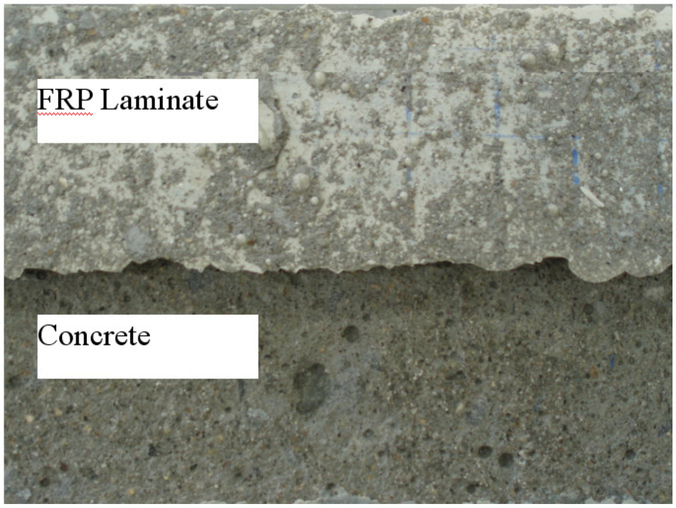

Fig. 4.21: Typical dry-bond surface (after pullout test)

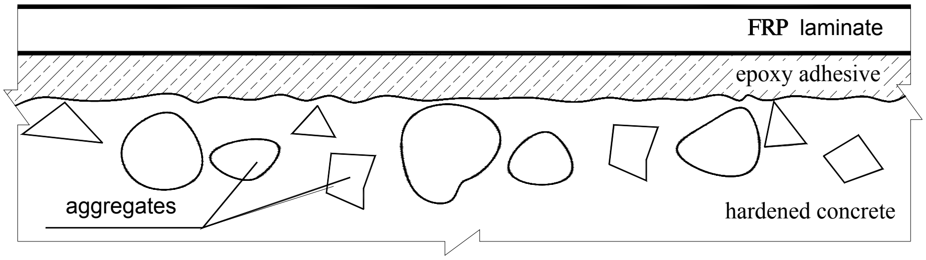

Fig. 4.22: Schematic dry-bond mechanism

Figure 4.21 is the typical failed interface of dry-bond after pullout test. It was evident that a thin layer of cement was attached on laminate, which implies that dry-bond is dominated by adhesive bond and tensile strength of concrete substrate. This was also reported by many other researchers (Gemert, 1980; Maeda et al., 1997). A schematic drawing of bond between laminate and hardened concrete is shown in Figure 4.22.

### (2) Comparison between wet-bond and dry-bond

Figure 4.23 and Figure 4.24 show the typical load-strain and load-slip curves of wet-bond (B2W2) and dry-bond (B2D1) respectively. During early loading stage ($P \leq 4kN$), the difference of tensile strain and accumulated slip between wet-bond and dry-bond was not obvious. Strain curve of wet-bond had an earlier bend-over indicating initial debonding around 1000 με by near 6kN, while dry-bond had a bend-over representing carbon fibre fracture at 2000 με by 10kN, after which the plateau shows the typical glass fibre elongation of hybrid composite. From Figure 4.24, slip of wet-bond was larger than dry-bond under low load level because of earlier debond, but it went to the opposite after carbon fracture where suddenly considerable slip was attributed by glass fibre elongation.

Based on observation of typical failed interface of wet-bond and dry-bond, it is noted that the thickness of adhesive was not uniform in wet-bond compared to that in dry-bond. For estimation of adhesive thickness for wet-bond, measurement was taken at three different locations from the same sample after pullout test. Ten samples from wet-bond were examined and the approximate average thickness is obtained by Equation 4.1 and the results are shown in Table 4.3.

$$t_{adh} = t_{total} - t_{frp} \tag{4.1}$$

Where:

$t_{adh}$, $t_{frp}$ = thickness of adhesive and hybrid laminate
$t_{total}$ = thickness of debonded laminate

Table 4.3 shows that the average thickness of dry-bond is smaller than that of wet-bond. The main reason is that part of epoxy was squeezed out at two sides of laminates for dry-bond while most of the epoxy was extruded into the concrete by gravity of aggregate in wet-bond. The difference of failed interface in Figures 4.17 and 4.21 illustrates this observation.

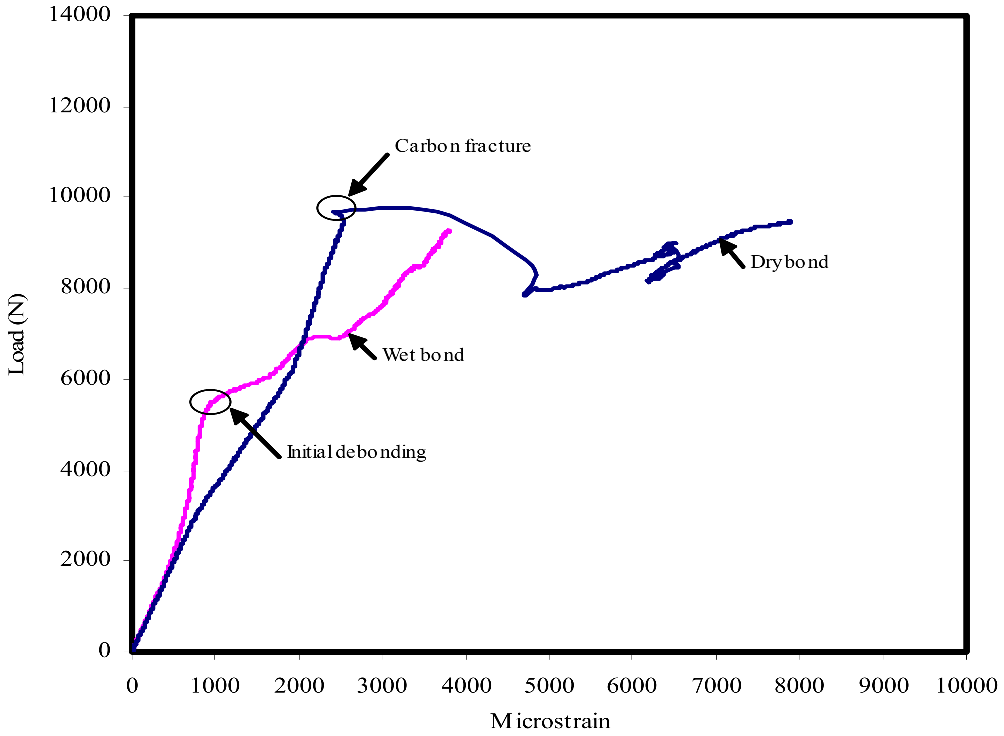

Fig. 4.23: Typical load-strain relation of wet-bond and dry-bond

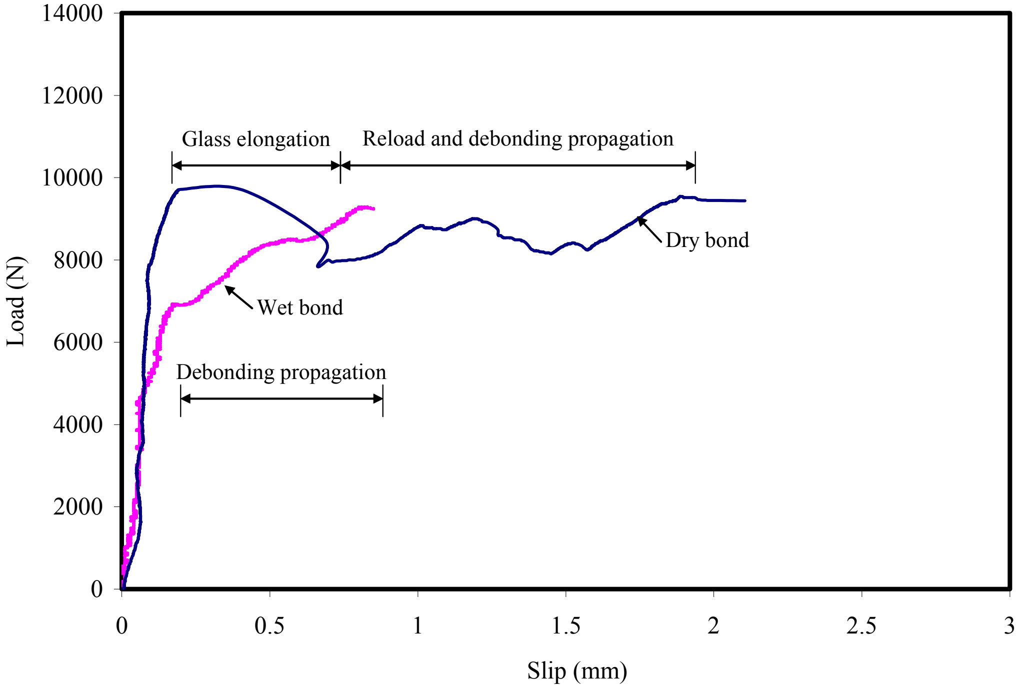

Fig. 4.24: Typical load-slip relation of wet-bond and dry-bond

**Table 4.3: Thickness of adhesive layer**

| Sample No. | Dry- bond (mm) | Wet-bond (mm) | | | |
|---|---|---|---|---|---|
| | | high | medium | low | Av. |
| 1 | 0.99 | 2.86 | 1.41 | 0.94 | 1.74 |
| 2 | 1.08 | 2.35 | 2.27 | 1.53 | 2.05 |
| 3 | 0.87 | 3.08 | 1.72 | 0.52 | 1.77 |
| 4 | 1.18 | 2.65 | 2.45 | 0.54 | 1.88 |
| 5 | 0.85 | 2.81 | 1.42 | 0.64 | 1.62 |
| 6 | 0.70 | 3.25 | 1.75 | 0.73 | 1.91 |
| 7 | 0.55 | 2.62 | 1.27 | 0.46 | 1.45 |
| 8 | 0.92 | 2.22 | 1.52 | 0.83 | 1.52 |
| 9 | 1.27 | 3.04 | 1.44 | 0.70 | 1.73 |
| 10 | 1.02 | 2.60 | 1.05 | 0.75 | 1.47 |
| Average | 0.94±0.2 | 2.75 | 1.63 | 0.76 | 1.71±0.19 |

## 4.5 Durability of wet-bond

Environmental exposures affect service life of FRP composite structures through deterioration of bond between FRP laminates and concrete. While extensive researches have been done on dry-bond properties, very little work was reported about the degradation of wet-bond.

In this project, different environmental exposures were designed to study deterioration of wet-bond, including the influence of materials such as concrete, FRP laminates and epoxy adhesive. Durability of concrete was examined by compression tests and durability of hybrid FRP laminates was determined by uni-axial tensile test. In addition, durability of adhesive was evaluated by differential scanning calorimeter (DSC) test and the overall performance of wet-bond was examined by pullout tests.

### 4.5.1 Durability of concrete

Three concrete cylinders were tested in each groups for average. The compressive strengths of concretes exposed to four severe environments: low temperature at -25$^{o}$C, 100 cycles of freeze/thaw from -17°C to +4°C, immersion in +35°C hot water and 50 cycles of wet/dry exposures, are shown in Fig. 4.25. Compared to reference, the compressive strength of concrete was reduced by 9% in continuous low temperature; by 12% after 100 freeze/thaw cycles; by 13% in 25 days of hot water immersion and by 5% after 50 wet/dry cycles. In pullout test, the maximum compression stress induced by top bearing steel plate was around 2 MPa, 3% of concrete compressive strength and there was no obvious concrete block failure in pull-out test. According to Equation 2.3, concrete compressive strength has certain influence on ultimate bond force. The maximum difference caused by $\sqrt{f'_{con}}$ is 7% within these five groups.

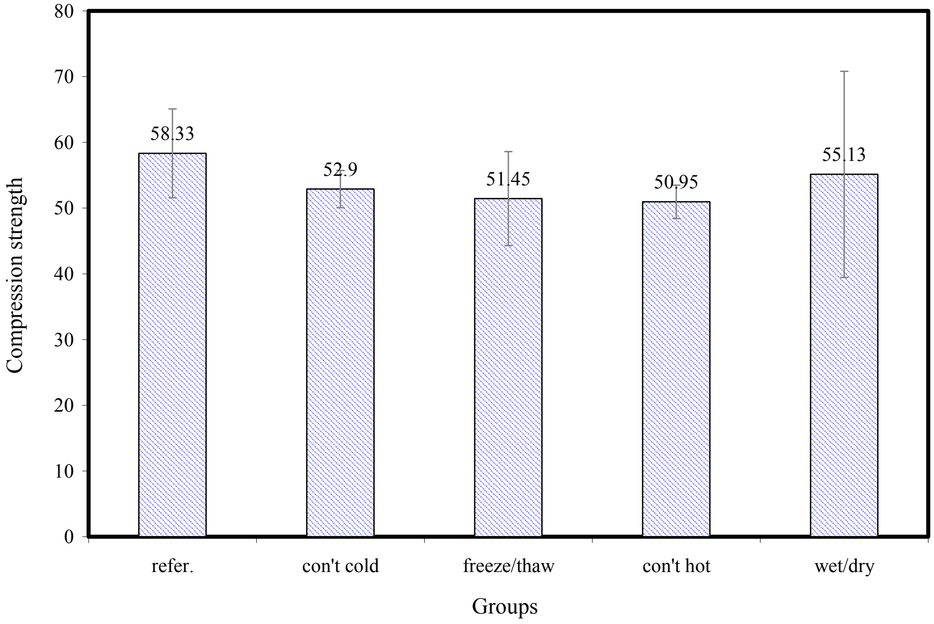

**Fig. 4.25: Durability of concrete**

## 4.5.2 Durability of hybrid FRP laminate

Durability of hybrid FRP laminates may have an effect on the wet-bond durability; it was evaluated by measuring the tensile behaviour under the same environmental exposure used in pullout tests. The typical tensile stress- strain curves are shown in Figure 4.26 and experimental results are summarized in Table 4.4.

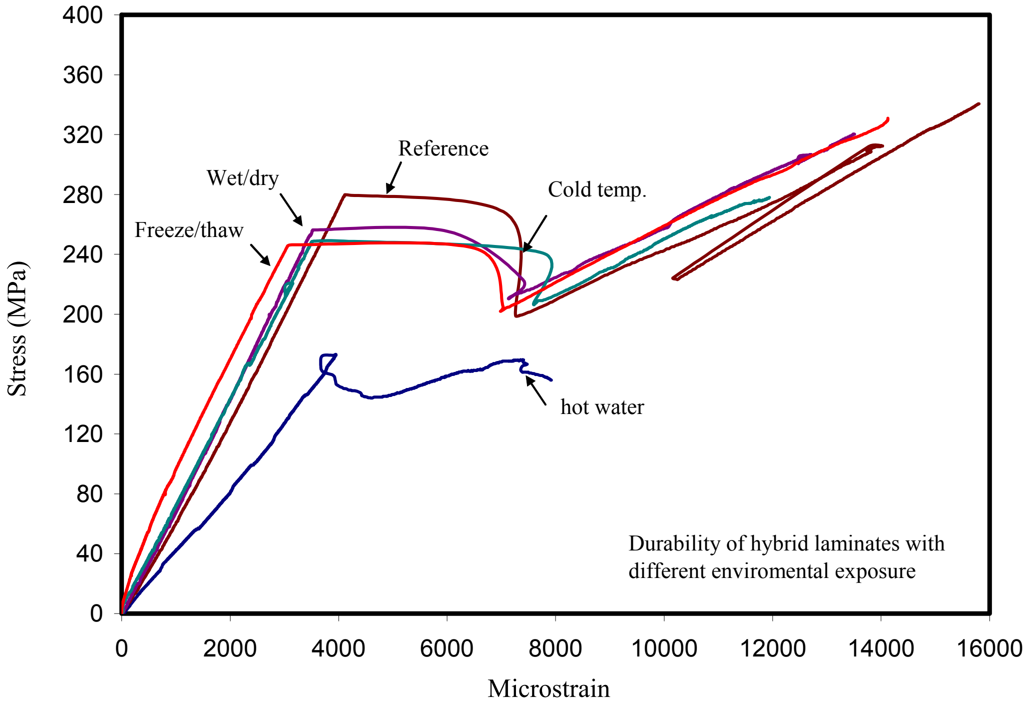

**Fig. 4.26: Tensile behaviour of hybrid laminates with environmental exposures**

The reference laminate without exposure demonstrated higher carbon fibre fracture strain, first crack strength and ultimate strain. It is noted that modulus of laminate exposed to low temperature was increased but ultimate strain of carbon fibre was decreased. It is possible that the low temperature caused degradation of the fibre and matrix inducing more brittleness of hybrid composite. Laminates exposed to high temperature and moisture aging experienced severe damage with significant reduction in strength, ductility and stiffness.

Figure 4.26 shows that even though the strength and modulus of laminate in hot water was reduced, its carbon fracture strain was still around 4000 με. It is because carbon fibre has much more resistance to harsh environment and the performance loss is mainly caused by degradation of epoxy or the interface of bond.

**Table 4.4: Tensile test results for hybrid FRP laminates with durability exposure**

| Samples | Durability exposure | Carbon fracture | | Ultimate | | Modulus (MPa) | |
|---|---|---|---|---|---|---|---|
| | | Strain (με) | Stress (MPa) | Strain (με) | Stress (MPa) | E1 | E2 |
| CH2 | Reference | 4114 | 280 | 15806 | 341 | 68060 | 21574 |
| CH3 | cold temp. | 3511 | 249 | 11941 | 278 | 70835 | 23281 |
| CH4 | freeze/thaw | 3135 | 246 | 15681 | 363 | 78609 | 23149 |
| CH5 | hot temp. | 3914 | 173 | 7409 | 168 | 44200 | - |
| CH6 | wet/dry | 3522 | 256 | 14712 | 336 | 72771 | 22838 |

### 4.5.3 Durability of wet-bond

After durability exposure, wet-bond and dry-bond, samples of each group were evaluated by pullout tests. All samples failed by total debonding except those which experiencing high temperature and moisture, which failed by hybrid laminates fracture instead. As discussed before, there are two key loads to compare bond quality of wet-bond and dry-bond, the first crack load and peak load. Experimental results are summarized in Table 4.5 for wet-bond samples and Table 4.6 for dry-bond samples.

#### (1) Comparison of wet-bond durability

Figure 4.27 shows average value of first crack load and peak load of wet-bond samples. All wet-bond samples started with initial debonding, and some of them followed by carbon fibre fracture. Comparing their initial debonding load, group B3 (continuous low temperature exposure) was the best one and group B6 (wet/dry cycles) was the lowest one. Samples of B5 (continuous hot water) and B2 (reference) started to debond at almost the same load level. It is apparent that for all wet-bond samples, peak load is much higher than first crack load. It was different from previous research about dry-bond without environmental exposure and using only one type of material, in which it was suggested that debonding propagation was non-steady state and its crack load was very close to peak load.

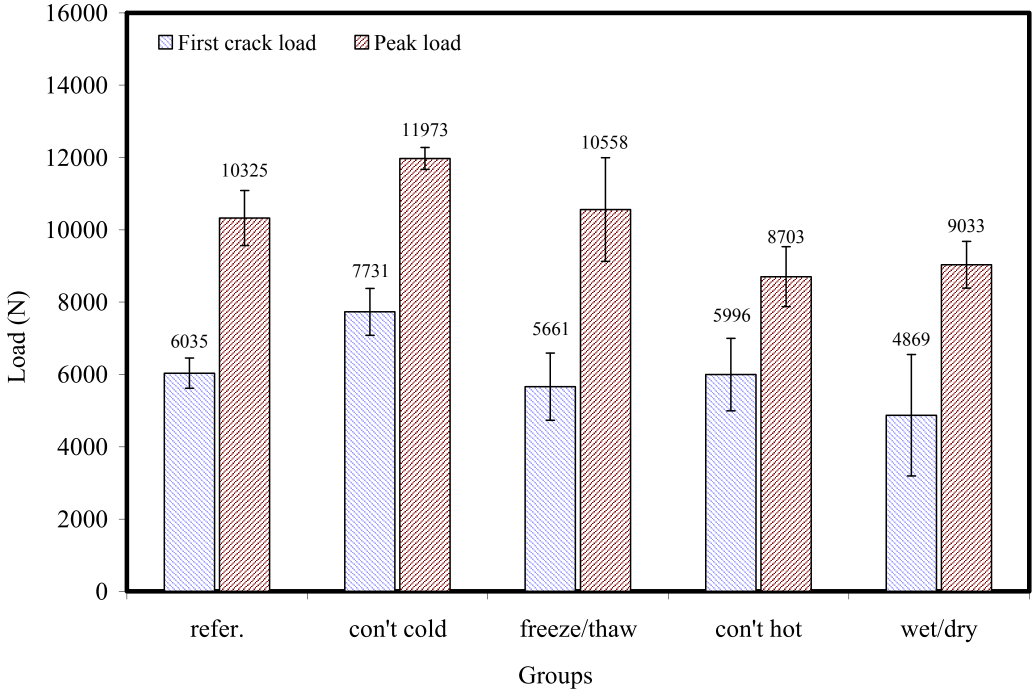

**Fig. 4.27: First crack load and peak load of wet-bond**

Comparison of peak load among groups indicates that low temperature environment can enhance bond strength slightly (15% increase in B3) and 100 freeze thaw cycles exposure has no significant influence on bond quality (2% increase in B4). However after 50 wet/dry cycles at room temperature (B6), wet-bond strength was reduced by 12.5%. The big difference between initial debonding strength and overall bond strength for each group implies that although weak bond between concrete and laminate is responsible for early initial debonding, mechanical interlock between epoxy adhesive and aggregates provides a frictional bond to reach a high ultimate load. For continuous hot water exposure group (B5), the peak stress at pull-out test was 193 MPa exceeding the tensile strength of FRP laminate 173 MPa (Table 4.4) at the same exposure conditions. For this group, it is hard to evaluate the bond quality because laminate failed instead of debonding. Peak loads shown in Figure 4.27 for group B5 implied the deteriorated hybrid laminates failure.

**Table 4.5: Pull-out results of wet-bond samples**

| Samples | | First crack load (N) | | Peak load (N) | | Carbon fracture point | Failure mode |
|---|---|---|---|---|---|---|---|
| | | | Av. | | Av. | | |
| B2 (refer.) | W1 | 6200 | 6035±417 | 11102 | 10325±760 | -20 mm | 2 |
| | W2 | 5463 | | 9294 | | NF | 3 |
| | W3 | 6443 | | 10580 | | NF | 3 |
| B3 (low temp.) | W1 | 6832 | 7731±647 | 12352 | 11973±300 | 65 mm | 2 |
| | W2 | 8329 | | 11619 | | 0 mm | 2 |
| | W3 | 8031 | | 11949 | | 0 &<br>40 mm | 2 |
| B4 (freeze/thaw) | W1 | 4391 | 5661±929 | 8712 | 10558±1432 | NF | 3 |
| | W2 | 6004 | | 12201 | | 4 mm | 2 |
| | W3 | 6587 | | 10762 | | 2 mm | 2 |
| B5 (hot water) | W1 | 4577 | 5996±1004 | 8517 | 8703±830 | 15 mm | 2 |
| | W2 | 6710 | | 7792 | | 5 mm | 2 |
| | W3 | 6701 | | 9799 | | 20 mm | 2 |
| B6 (wet/dry) | W1 | 3678 | 4869±1682 | 8326 | 9033±646 | NF | 3 |
| | W2 | 7247 | | 9887 | | NF | 3 |
| | W3 | 3681 | | 8885 | | NF | 3 |

*Note: NF = no carbon fracture; First crack load can be the load causing carbon fibre fracture or bond fracture; carbon fracture position is the distance from load end, positive inside bond and negative outside bond.

### (2) Comparison with dry-bond durability

Experimental results for dry-bond samples of each group are shown in Figure 4.28 and Table 4.6. Figure 4.28 shows average first crack load and peak load of dry-bond samples. It is noticed that for reference group, initial load is very close to peak load, and it starts with carbon fibre fracture. On the contrary, dry-bond samples with environmental exposure fail by initial debonding, which indicates that exposure causes deterioration of bond. The peak load of samples with 100 freeze/thaw cycles is approximately equal to reference group, while samples from continuous low temperature and wet-dry cycle exhibit lower ultimate. As for wet-bond, samples exposed to high temperature and moisture are induced by fracture of hybrid laminates instead of full debonding.

Figure 4.28 also shows that the difference between peak load and first crack load of dry-bond is smaller than corresponding wet-bond, except for group B6 (wet/dry cycles). It was likely attributed to stronger adhesive strength, once debonding occur, potential bond strength can’t compare with the interlock action in wet-bond.

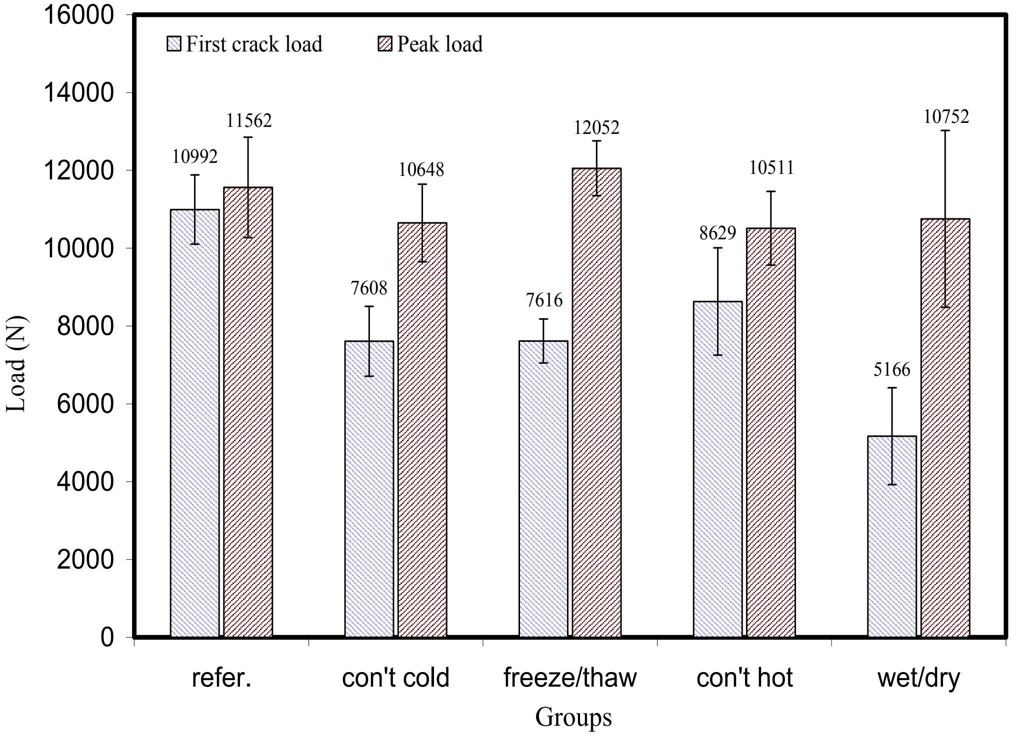

**Fig. 4.28: First crack load and peak load of dry-bond**

For group B6 exposed to wet/dry cycles, repeating absorption and desorption caused expansion and contraction cycles of the laminate and epoxy generating pseudo-fatigue load, especially at pre-notch point where initial debonding started. As for wet-bond, samples in group B5 aged in hot water failed by fracture of hybrid laminates instead of full debonding because high temperature combined with moisture caused significant degradation of hybrid laminates, which failed before bond strength could be reached.

**Table 4.6: Pull out result of dry-bond samples**

| Samples No. | | First crack load (N) | | Peak load (N) | | Carbon fracture point | Failure Mode |
|---|---|---|---|---|---|---|---|
| | | | Av. | | Av. | | |
| B2 (refer.) | D1 | 9607 | 10992±887 | 9709 | 11562±1291 | 0 mm | 1 |
| | D2 | 11395 | | 12499 | | 0 mm | 1 |
| | D3 | 10940 | | 11037 | | 0 mm | 1 |
| | D4 | 12025 | | 13003 | | 0 mm | 1 |
| B3 (low temp.) | D1 | 7633 | 7608±897 | 9639 | 10648±999 | 15 mm | 2 |
| | D2 | 6497 | | 10298 | | NF | 3 |
| | D3 | 8695 | | 12009 | | 17 & 70 mm | 2 |
| B4 (freeze/thaw) | D1 | 7055 | 7616±566 | 12485 | 12052±707 | 10 mm | 2 |
| | D2 | 8391 | | 12615 | | 40 mm | 2 |
| | D3 | 7401 | | 11055 | | 22 & 95 mm | 2 |
| B5 (hot water) | D1 | 7105 | 8629±1380 | 9446 | 10511±949 | -1 mm | 1 |
| | D2 | 10447 | | 11751 | | 0 mm | 2 |
| | D3 | 8335 | | 10336 | | 5 mm | 2 |
| B6 (wet/dry) | D1 | 3511 | 5166±1245 | 7542 | 10752±2271 | 20 mm | 2 |
| | D2 | 5471 | | 12262 | | 43 mm | 2 |
| | D3 | 6515 | | 12451 | | 0 mm | 2 |

### (3). Comparison of bond durability between wet-bond and dry-bond

A comparison of wet-bond with dry-bond in terms of first crack load, peak load, and their corresponding ratio is represented in Figure 4.29 for first crack load and Figure 4.30 for peak load. The ratio of wet-bond to dry-bond is given in Table 4.7. Durability comparison between wet-bond and dry-bond for each group is discussed.

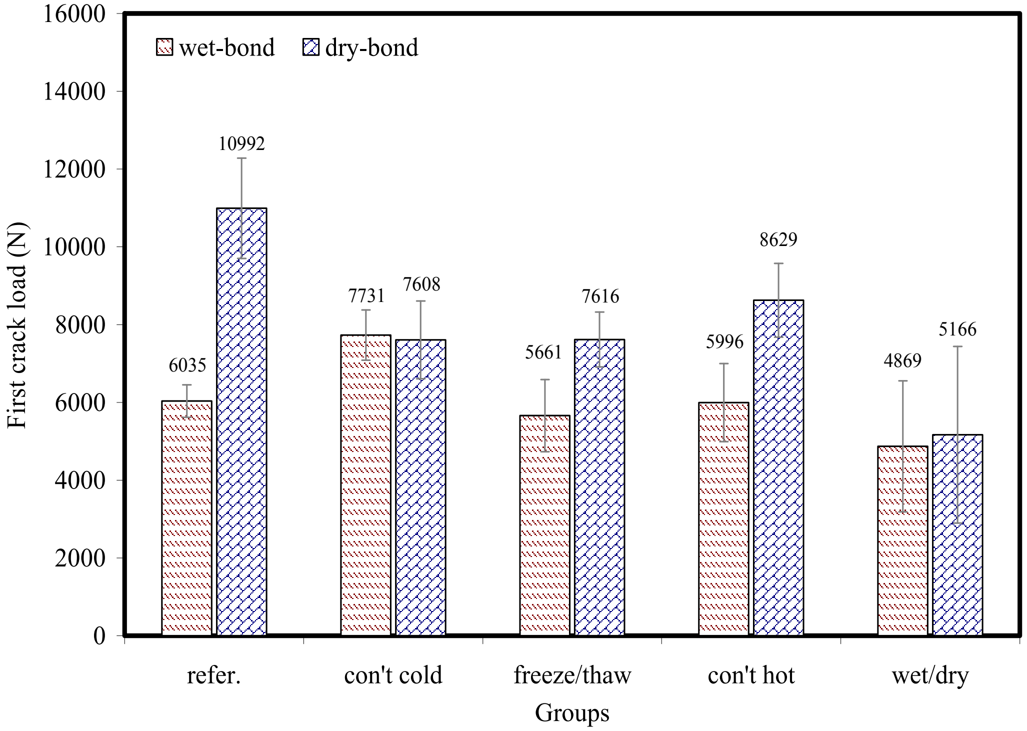

**Fig. 4.29: Bond durability of first crack load**

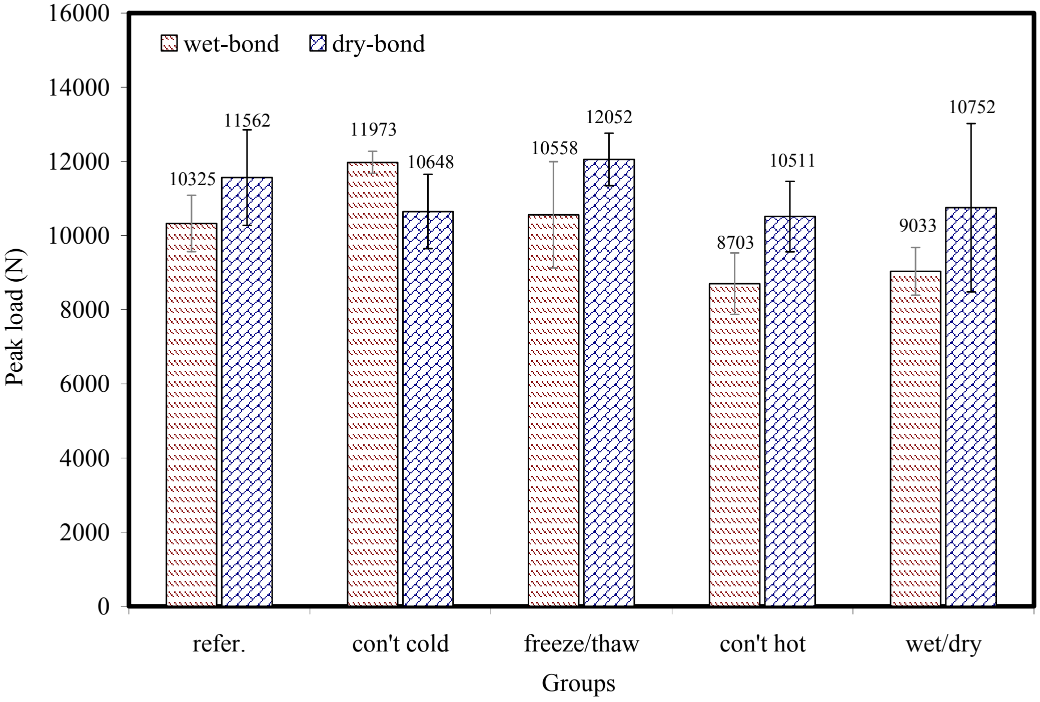

**Fig. 4.30: Bond durability of peak load**

### i) Reference group without durability exposure (group B2)

Based on previous discussion on reference group, first crack of wet-bond was caused by initial debonding, while that of dry-bond was caused by carbon fibre fracture. As shown in Table 4.7, the first crack load of wet-bond was 55% of that of dry-bond and their difference was the most significant. However, the difference was reduced to 89% when the peak load was reached. Without environmental exposure, results of reference group demonstrated that although interfacial adhesive bond strength of wet-bond is smaller than dry-bond, its bond strength was compensated by contribution of interlock mechanism later.

### ii) Continuous low temperature exposure (group B3)

Exposed to continuous low temperature of -25$^{o}$C in dry air, on the contrary to reference group, initial debonding load of wet-bond and dry-bond is comparable, ultimate peak load of wet-bond is stronger than dry-bond. Because of micro-cracks in concrete caused by low temperature, tensile strength of concrete substrate was degraded and concrete substrate was easier to crack; for wet-bond, penetrated epoxy adhesive direct interaction with aggregates helped establish interlock action. During debonding propagation stage, concrete substrate eventually failed by crack in dry-bond. In wet-bond samples, interlocked adhesive and aggregates were still holding caused larger increase of bond strength.

### iii) Freeze/thaw cycles exposure (group B4)

For 100 freeze/thaw cycles exposure group, temperature changed from + 4$^{o}$C to –17.7$^{o}$C during which samples were immersed in water with bond plane facing down. Table 4.7 shows first crack load of wet-bond is 26% lower than dry-bond but the difference decreases to 12% for peak load comparison. It is because adhesive layer of wet-bond is rather porous and could absorb more water, after freeze/thaw cycles exposure, adhesive bond between concrete and epoxy was weaker than dry-bond, but interlock mechanism provides good interact contribution to peak load.

### v) Continuous hot water exposure (group B5)

With 25 days continuous +35$^{o}$C hot water immersion, first crack load of both bond samples reached in a mode of initial debonding and ended with laminates fracture. It is very hard to estimate real bond strength for this group because experiments showed that failure was cause by fracture of laminates. Continuous hot water results in significant degradation of matrix and its bond with glass fibre, which is responsible for substantial reduction of modulus of hybrid laminates. Compared bond strength, degradation of laminates was worse and the full bond strength of wet-bond and dry-bond could not be obtained. For initial debonding load comparison only, it is probably the serrated surface of wet-bond got more water absorption causing smaller debonding load than dry-bond.

### iv) Wet /dry cycle exposure (group B6)

After 50 wet/dry cycles exposure, initial debonding strength of wet-bond was proximately equal to dry-bond. Repeated drying in air for 4 hours and immerged in water for 8 hours per cycle at room temperature caused bond interface degradation by water absorption of epoxy adhesive and moisture evaporation. As discussed before, interlock mechanism played an important role leading to peak load increase greatly at the end. It is noted that there is little cement attached on the fracture bond interface of wet-bond, suggesting a weak adhesive bond between the adhesive and concrete.

Table 4.7 shows the ratio of wet-bond to dry-bond for first crack load is smaller than that for peak load. It illustrates that although porosity of epoxy adhesive along bond interface may cause weak adhesive bond strength in wet-bond, interlock action between adhesive and aggregates could contribute to ultimate bond strength. After initial debonding, interlock mechanism in wet-bond makes its bond strength more comparable with dry-bond. In addition, Table 4.7 shows that the ratio of first crack load of wet-bond to dry-bond for B2 group is the lowest one, which is possibly due to the fact that dry-bond of B2 has highest first crack load.

**Table 4. 7: Comparison of wet-bond and dry-bond**

| Groups | Durability exposure | Wet-bond : dry-bond | |
|---|---|---|---|
| | | First crack Load (N) | Peak Load (N) |
| B2 | — | 55% | 89% |
| B3 | Cont. cold | 102% | 112% |
| B4 | Freeze/thaw | 74% | 88% |
| B5 | Hot water | 70% | 83% |
| B6 | Wet/dry | 94% | 84% |

### 4.5.4 Durability of epoxy adhesive

The weak adhesive bond in wet-bond is possibly caused by the degradation of epoxy adhesive. Therefore, it is necessary to examine the durability of epoxy adhesive. Degree of curing (DOC) is the ratio of examined sample over the same epoxy cured under ideal condition in Differential Scanning Calorimeters (DSC) machine. DSC equipment measures temperatures and heat flows associated with thermal transitions in a material. Glass transition temperature (Tg) is the temperature where the polymer goes from a hard, glassy like state to a rubber like state. The higher Tg, the better resistance to moisture and temperature. In this project, DOC and Tg of epoxy adhesive cured with and without moisture were tested. Two sets of fresh mixed epoxies were cured in air and in water respectively for one week after which specimens were tested in DSC to obtain their DOC and Tg.

Experimental results are shown in Table 4.8. It seems that epoxies cured in water and cured in air have the same DOC, which means the presence of moisture has no effect on degree of curing for this kind of epoxy. But glass transition temperature is 10% higher for water cured epoxy than air cured one, which means the thermal stability of epoxy cured in water is even better than epoxy cured in air. It is known that Tg of epoxy is sensitive to its historical heat in curing, higher temperature environment causes higher Tg value. Epoxy cured in water has slightly higher Tg. It may be attributed to the heat initially created during the polymerization and later preserved by water.

**Table 4.8: Properties of epoxy cured with and without moisture**

| Curing condition | Tg ($^{o}$C) | DOC (%) |
|---|---|---|
| Water cure | 39.14 | 93.52 |
| Air cure | 35.63 | 93.56 |

Although experimental results showed that DOC and Tg of epoxy adhesive cured with presence of moisture were comparable with those cured in air, the surface examination by microscope suggested that wet-cured epoxy contains more air bubbles. Figure 4.31 compare the micrographs of surface of epoxy cured in water and air. It is clear that epoxy cured in water had distributed air bubbles of about 0.2 mm in diameter on the surface; while for the epoxy cured in air, it is clean and flat. The area of air bubbles is about 15% of total surface, which suggests the contact area of adhesive and concrete was reduced by 15%. The phenomena was also observed by other researchers in their water uptake tests; that excess water during the curing stage evaporated after curing, leaving more free volume which contributes to a greater moisture absorption for the resin (Hoa, 2004).

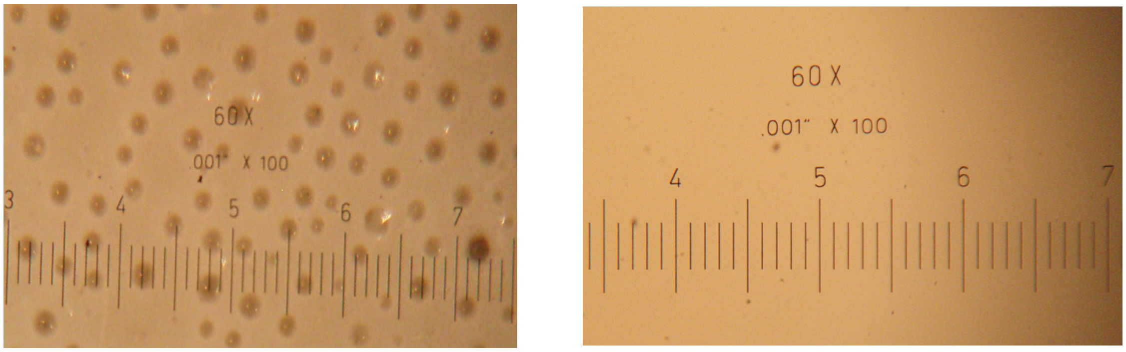

**(a) surface of epoxy cured in water** **(b) surface of epoxy cured in dry air**

**Fig. 4.31: Surface of epoxy cured in water and dry air**

After pullout test, epoxy adhesives were detached from fracture surface of laminate and evaluated for their DOC (degree of curing) and Tg (glass transition temperature) respectively. Results are displayed in Figure 4.32 and Figure 4.33.

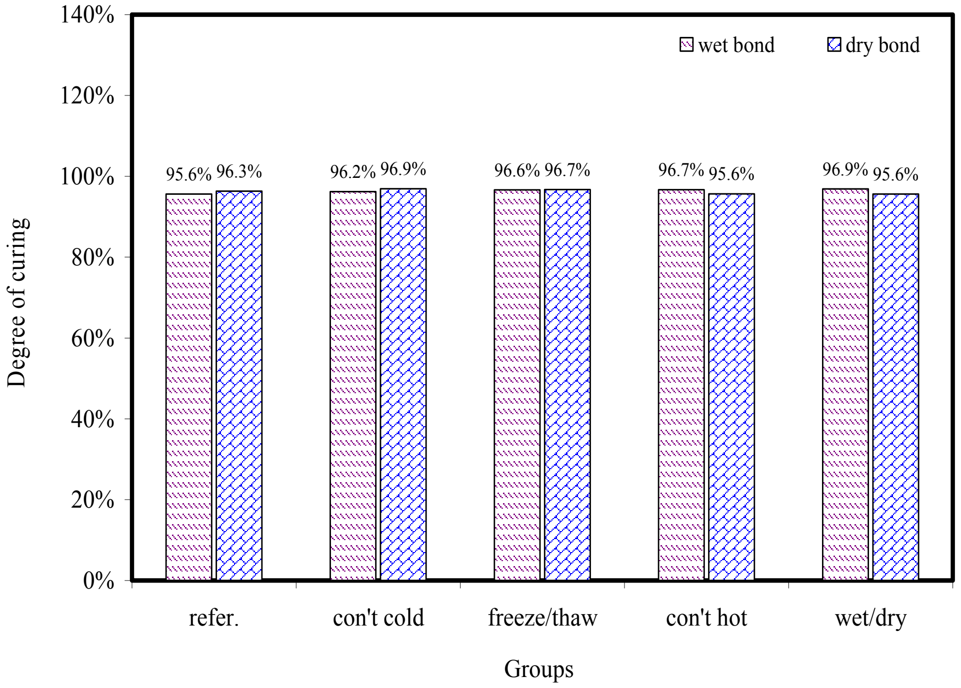

**Fig. 4.32: DOC of epoxy adhesive collected from fracture surface**

Figure 4.32 shows that epoxy adhesives for both wet-bond and dry-bond were not completely cured but their degrees of cure were very close. It is indicative that the influence of wet-bond and the exposure to severe environments does not seem to be significant on DOC. In addition, the DOC of epoxy for both types of bond after pullout test was even higher than that of curing test (Table 4.8). It is because the sample for neat resin was cured only one week but samples from pullout tests have been kept for over one month before casting.

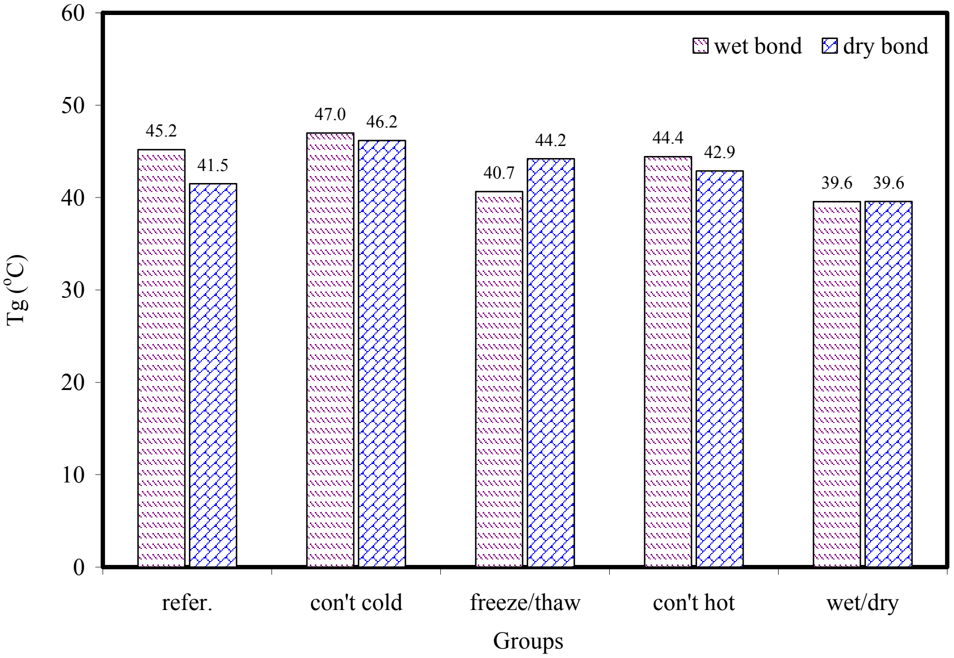

**Fig. 4.33: Tg of epoxy adhesive collected from fracture surface**

Figure 4.33 shows that epoxies cured with fresh concrete also seem to have higher Tg than that of dry-bond after durability exposures. It illustrates that the long term thermal stability of epoxy adhesive of wet-bond was comparable to that of dry-bond. It is possible the heat generated by hydration of concrete provide a higher temperature for epoxy during curing. Evaluation of epoxy proves that the presence of moisture in curing of epoxy does not affect DOC and Tg, but indirectly the air bubbles produced may reduce the bond strength in wet-bond.

The debonded interface of epoxy adhesive also examined after pullout test. Microscopic observation revealed similar phenomena as seem by neat resin that there existed air bubbles in wet-bond adhesive layer, although the amount of air bubbles was significantly reduced (Figure 4.34 a).

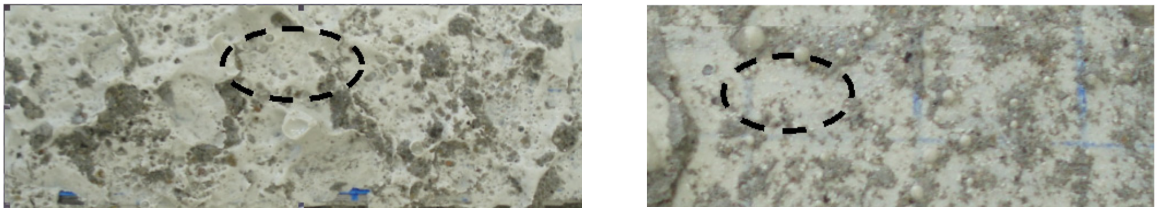

**(a) typical bond interface of wet-bond** **(d) typical bond interface of dry-bond**

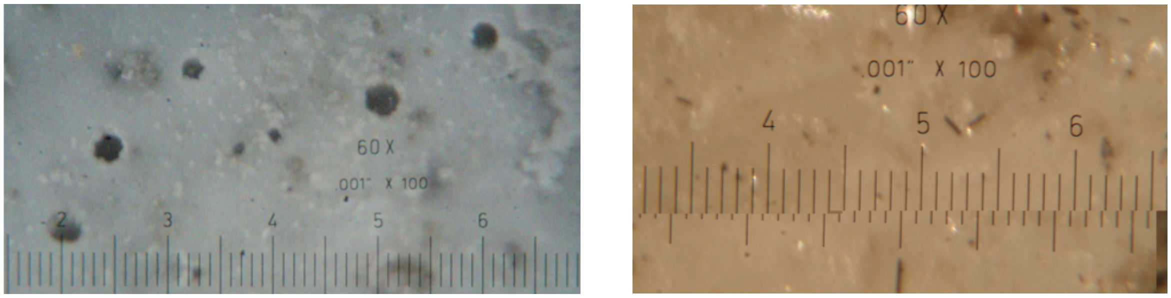

**(c) enlarged adhesive interface of wet-bond** **(d) enlarged adhesive interface of dry-bond**

**Fig. 4.34: Interface of epoxy adhesive for wet-bond and dry-bond**

## 4.6 Conclusions

In conclusion, the comparison of initial crack loads and peak loads demonstrates that bond mechanisms of wet-bond and dry-bond are different. The porous epoxy adhesive surface in wet-bond is responsible for relatively weak adhesive bond but interlock action provided additional mechanical bond strength for wet-bond. Combined with hybrid composite, the bond of FRP to concrete has much more complicated behaviour than single material. Carbon fibre fracture and initial debonding are predominant factors to classify different failure stages. Three failure modes are observed in pullout test and conclusions can be made as following:

- For the reference group, FRP laminate doesn't experience any degradation. Carbon fibre fracture is dominant in dry-bond (failure Mode I) while debonding is the cause of wet-bond failure (failure Mode III), which implies that strength of dry-bond is higher than wet-bond without environmental exposure.

- Comparison of tensile test of hybrid laminates in Figure 4.26 shows that the modulus and strength of laminate are not affected by wet/dry cycles. But water absorption and desorption of porous adhesive generated pseudo-fatigue and is responsible for wet-bond debonding failure after 50 wet/dry cycles in Mode III.
- Most wet-bond and dry-bond samples subjected to environmental exposures starts with initial debonding followed by carbon fibre fracture, which is Mode II. Bond deterioration differs by various durability conditions. Based on previous discussion, low temperature causes more brittleness of hybrid composite and epoxy adhesive, leading to debonding before carbon fibre fracture.
- For dry-bond, the degradation of bond is worse than that of laminate due to environmental exposure and its failure mode changed from Mode I (carbon fracture first) to Mode II (initial debonding occurs first). On the contrary, wet-bond mainly depends on physical interlock action between adhesive and aggregate, which are less affected by durability conditions comparing adhesive bond. Moreover, deterioration of laminate causes carbon fibre fracture happens during the propagation of debonding, especially for samples with continuous hot water immersion. In most wet-bond, laminates get more effected by exposure and Mode II becomes the main failure mode.
- Although wet-bond is not as strong as dry-bond in most conditions, but durability investigation results demonstrate that wet-bond is comparable to dry-bond with low temperature exposure. In cold area, wet-bond technology could be a good alternative to dry-bond.

# Chapter 5 Analytical Modeling

Based on the understanding of structural performance of hybrid materials and its bond to concrete, an analytical model is developed in this chapter to simulate the pullout behaviour of hybrid laminate bonded to concrete by either wet-bond or dry-bond method.

## 5.1 Modelling of hybrid FRP laminate in tension

Figure 5.1 is a typical load-strain curve of hybrid laminate in tension. There are three main stages during the process, linear elastic deformation, carbon fibre fracture and glass fibre elongation followed by load drop and reloading until glass fibre failure.

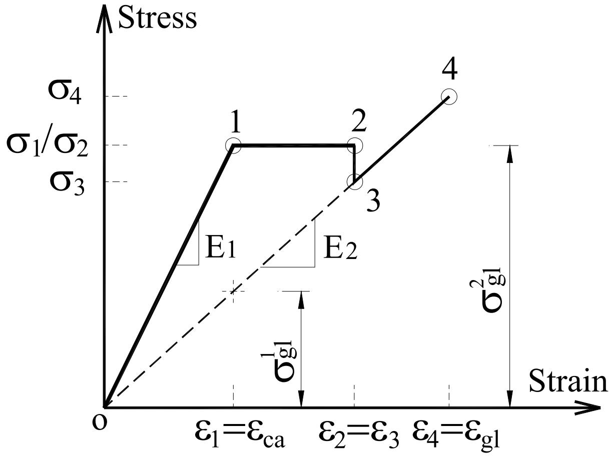

**Fig. 5.1: Typical tensile load-strain curve of hybrid laminate**

Note: $\sigma^1_{gl}$ = tensile stress in glass fibre when $\varepsilon_1 = \varepsilon_{ca}$ (carbon fracture)
$\sigma^2_{gl}$ = tensile stress in glass fibre after carbon fracture

### (1) Linear elastic deformation

The linear elastic stage follows the rule of mixture. The first crack load $P_1$ happens when the strains of laminate $\varepsilon_1$ reach the carbon fibre ultimate strain $\varepsilon_1 = \varepsilon_{ca}$.

$$P_1 = t_1 \times b \times E_1 \times \varepsilon_{ca} \tag{5.1}$$

The tensile stress of the hybrid laminate at carbon fibre fracture, $\sigma_1$, is:

$$\sigma_1 = E_1 \times \varepsilon_{ca} \tag{5.2}$$

The tensile stress of the glass fibre at carbon fibre fracture, $\sigma_{gl}{}^1$, is:

$$\sigma_{gl}{}^1 = E_2 \times \varepsilon_{ca} \tag{5.3}$$

where:

$E_{ca}$, $E_{gl}$, $E_{ma}$ = the modulus of carbon, glass fibre and epoxy matrix (Table 3.2)

$t_{ca}$, $t_{gl}$, $t_{ma}$ = the thickness of carbon, glass fibre and epoxy matrix (Table 3.2)

$t_{ca} = 1 \times 0.143$ mm $=0.143$ mm

$t_{gl} = 4 \times 0.118$ mm $= 0.472$ mm

$t_l$ = thickness of laminate, control to 1.8 mm

$t_{ma}$ = total thickness of epoxy matrix in laminate = $1.8 - t_{ca} - t_{gl} = 1.185$ mm

b = width of laminate, 25 mm

$E_1 = (E_{ca} \times t_{ca} + E_{gl} \times t_{gl} + E_{ma} \times t_{ma}) / t_1 = 65874$ MPa

$E_2 = (E_{gl} \times t_{gl} + E_{ma} \times t_{ma}) / t_2 = 28616$ MPa

$\varepsilon_{ca} = 4000\ \mu\varepsilon$ (experimental data in Table 4.1)

Superscript of $\sigma_{gl}{}^1$ refers to corresponding load point number in schematic of failure mode.

**(2) Carbon fibre fracture and glass fibre elongation**

Once carbon fibre fracture occurs, the load carried by the carbon is suddenly transferred to the glass fibre causing instantaneous elongation of the glass fibre. The tensile stress in the glass fibre after carbon fracture, $\sigma_{gl}{}^2$, is:

$$\sigma_{gl}{}^2 = \frac{P_1}{t_2 b} = \frac{\varepsilon_{ca} E_1 t_1 b}{t_2 b} = \varepsilon_{ca} E_1 \frac{t_1}{t_2} \tag{5.4}$$

where: $t_2$ = thickness of laminate after carbon fracture = $t_{gl} + 4/5 \times t_{ma} = 1.42$ mm (thickness of glass fibre and the matrix)

The difference of glass fibre stress before and after carbon fibre fracture is (Figure 5.1):

$$\Delta\sigma_{gl} = \sigma_{gl}{}^{2} - \sigma_{gl}{}^{1} = \varepsilon_{ca} \cdot (E_1 \frac{t_1}{t_2} - E_2) \tag{5.5}$$

A schematic of carbon fracture is given in Figure 5.2. The elongation of glass fibre caused by load transfer can be expressed as:

$$\Delta\varepsilon_{gl} = \frac{\Delta\sigma_{gl}}{E_1} = \varepsilon_{ca} \cdot (\frac{t_1}{t_2} - \frac{E_2}{E_1}) \tag{5.6}$$

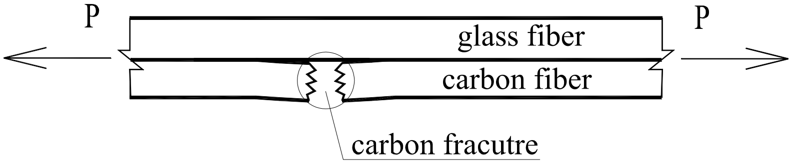

**Fig. 5.2: Typical failure mode of hybrid laminate**

The total strain of glass fibre after elongation is:

$$\varepsilon_2 = \varepsilon_{ca} + \Delta\varepsilon_{gl} = \varepsilon_{ca} \cdot (\frac{t_1}{t_2} - \frac{E_2}{E_1} + 1) \tag{5.7}$$

The tensile force after load drop becomes:

$$P_3 = \varepsilon_3 \cdot E_2 \cdot t_2 \cdot b = \varepsilon_2 \cdot E_2 \cdot t_2 \cdot b \tag{5.8}$$

### (3) Reloading until glass fibre failure

After carbon fibre fracture, glass fibre carries all pullout force gradually and deforms to ultimate strain of glass fibre $\varepsilon_4 = \varepsilon_{gl}$:

$$P_4 - P_3 = (\varepsilon_{gl} - \varepsilon_3) \times E_2 \cdot t_2 \cdot b \tag{5.9}$$

Substituting Eq. 5.8 in Eq. 5.9 leads to:

$$P_4 = \varepsilon_{gl} \cdot E_2 \cdot t_2 \cdot b \tag{5.10}$$

where: $\varepsilon_{gl}$ = 15800 $\mu\varepsilon$ (experimental data in Table 4.1)

The behaviour of hybrid laminates can be analytically predicted using ultimate strains of carbon and glass fibres as input data. Table 4.1 shows the average experimental ultimate strain of carbon fibre is 4000 με and of glass fibre is 15800 με in hybrid composite. Analytical prediction for every stage of hybrid behaviour is compared to uni-axial tensile tests in Figure 5.3 and Table 5.1.

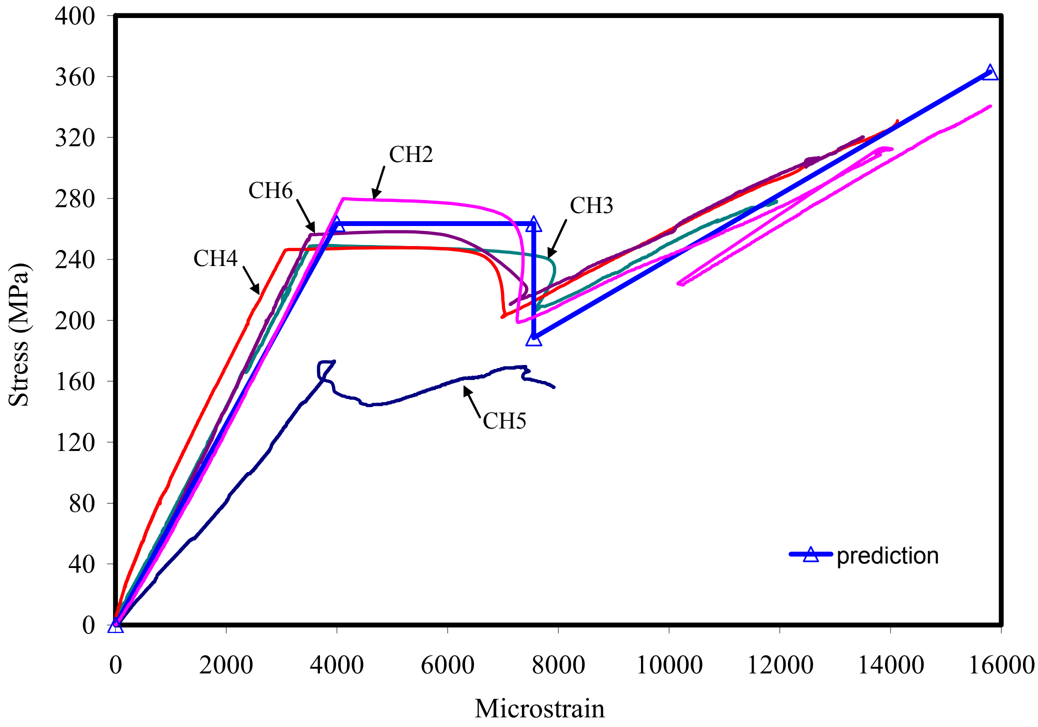

**Fig. 5.3: Comparison of numerical analysis and tensile test**

The behaviour of hybrid laminate without (CH2) or with environmental exposure (CH3~CH6) is well predicted by the numerical model, especially for glass fibre elongation and temporary load drop. It is noted that the modulus of the laminate exposed to low temperature was increased, but the ultimate strain of the carbon fibre was decreased. It is possible that low temperature causes degradation of fibre and matrix inducing more brittleness of hybrid composite. Sample CH6 with hot water exposure was seriously damaged and was therefore not comparable with numerical model.

**Table 5.7 Prediction of hybrid behaviour**

| Point | Analytical Prediction | | Experimental result | | | | | | | |
|---|---|---|---|---|---|---|---|---|---|---|
| | | | CH2 | | CH3 | | CH4 | | CH6 | |
| | σ (MPa) | ε (με) | σ (MPa) | ε (με) | σ (MPa) | ε (με) | σ (MPa) | ε (με) | σ (MPa) | ε (με) |
| 1 | 264 | 4000 | 280 | 4114 | 249 | 3511 | 246 | 3137 | 256 | 3522 |
| 2 | 264 | 7555 | 267 | 7087 | 241 | 7764 | 244 | 6520 | 255 | 6007 |
| 3 | 189 | 7555 | 200 | 7381 | 211 | 7861 | 202 | 6981 | 211 | 7133 |
| 4 | 363 | 15800 | 341 | 15806 | 278 | 11941 | 363 | 15681 | 336 | 14712 |

## 5.2 Behaviour of hybrid laminate bonded with concrete

### 5.2.1 Bond stress distribution

Bond stress as a shear stress between concrete and FRP laminate is non-linearly distributed along bond area (Neale et al., 1999). Figure 5.4 shows the schematic of equilibrium of single lap pullout sample, including bond stress $\tau(x)$.

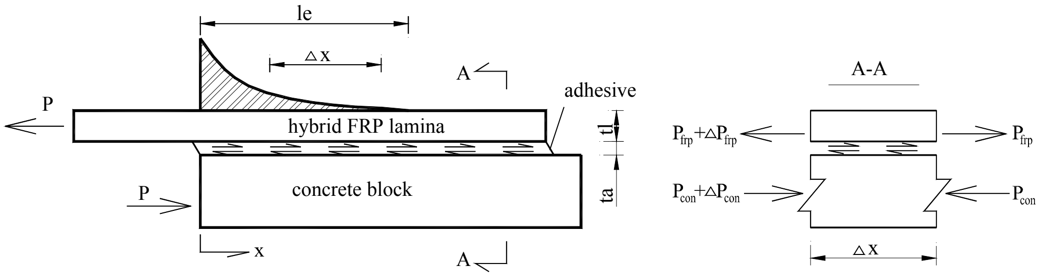

**(a) Equilibrium of pullout sample**

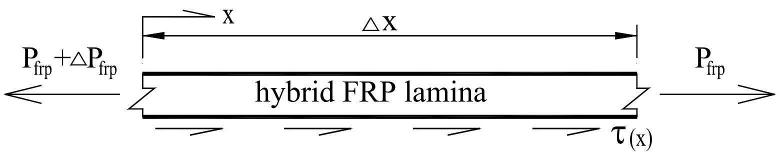

**(b) Equilibrium of hybrid FRP lamina**

**Fig. 5.4: Schematic of pullout test sample**

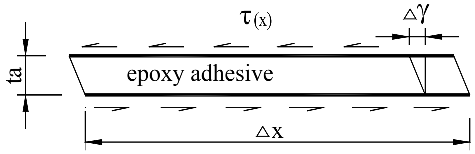

**(c) Equilibrium of adhesive**

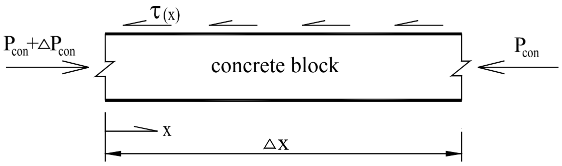

**(d) Equilibrium of concrete block**

**Fig. 5.4 (cont.): Schematic of pullout test sample**

The shear stress distribution is derived based on shear lag theory (Neal et al 1999) and material's elastic properties (Fig. 5.4 a):

For FRP laminate (Fig. 5.4 b):

$$\Delta P_{frp} = b \times \Delta x \times \tau(x) = A_{frp} \times \Delta f_{frp}(x)$$

$$\lim_{\Delta x \to 0} \Delta P_{frp} = b \times dx \times \tau(x) = A_{frp} \times df_{frp}(x)$$

$$\tau(x) = \frac{A_{frp}}{b} \cdot \frac{df_{frp}(x)}{dx} \tag{5.11}$$

And, for concrete (Fig. 5.4 d):

$$\Delta P_{con} = b \times \Delta x \times \tau(x) = A_{con} \times \Delta f_{con}(x)$$

$$\lim_{\Delta x \to 0} \Delta P_{con} = b \times dx \times \tau(x) = A_{con} \times df_{con}(x)$$

$$\tau(x) = \frac{A_{con}}{b} \cdot \frac{df_{con}(x)}{dx} \tag{5.12}$$

And, for adhesive (Fig. 5.4 c):

$$\tau(x) = G_{adh} \times \gamma(x)$$

$$d\tau(x) = G_{adh} \times d\gamma(x) \tag{5.13}$$

The deformation of FRP and concrete:

$$\varepsilon_{frp}(x) = f_{frp}(x) / E_{frp} \tag{5.14}$$

$$\varepsilon_{con}(x) = f_{con}(x) / E_{con} \tag{5.15}$$

Where: $A_{frp}$, $f_{frp}$, $\varepsilon_{frp}$ and $A_{con}$, $f_{con}$, $\varepsilon_{con}$ are the cross section area, tensile stress, tensile strain of hybrid laminates and concrete respectively; $t_{adh}$, $G_{adh}$ and $\gamma(x)$ are the thickness, shear modulus and shear strain of adhesive. $P_{frp}$ and $P_{con}$ are the forces carried by FRP and concrete respectively. Under the tensile force and shear force, laminate and concrete deform in opposite direction, their relative displacement is the sum of their deformation and can be expressed as:

$$ds = \left\{ \left| \varepsilon_{frp}(x) \right| + \left| \varepsilon_{con}(x) \right| \right\} \times dx = t_{adh} \cdot d\gamma(x) \tag{5.16}$$

Substituting Equations 5.13, 5.14 and 5.15 into Equation 5.16, we get:

$$f_{frp}(x) / E_{frp} + f_{con}(x) / E_{con} = \frac{t_{adh}}{G_{adh}} \times \frac{d\tau(x)}{dx} \tag{5.17}$$

Differentiating both sides of Equation 5.17 and combining Equations 5.11 and 5.12, get:

$$\frac{d^2\tau(x)}{dx^2} = \lambda^2 \tau(x) \tag{5.18}$$

with

$$\lambda^2 = \frac{G_{adh}}{t_{adh}} \cdot \frac{1}{t_{frp} E_{frp}} \cdot \left(1 + \frac{E_{frp} A_{frp}}{E_{con} A_{con}}\right) \tag{5.19}$$

Where, $t_{frp}$ is the thickness of laminate and the solution for Equation 5.18 is:

$$\tau(x) = M \cosh(\lambda x) + N \sinh(\lambda x) \tag{5.20}$$

Where, M and N are the parameters that can be found using boundary conditions (Figure 5.4a):

$$\text{at } x = 0, \; \varepsilon_{frp} = \frac{P}{A_{frp} E_{frp}} \text{ and } \varepsilon_{con} = \frac{P}{A_{con} E_{con}}$$

$$\text{at } x = le, \qquad \varepsilon_{frp} = \varepsilon_{con} = 0$$

Herein, $l_e$ is the effective length, which can be determined from Equation 2.1 (Chen and Teng 2001), which is:

$$l_e = \sqrt{E_{frp} t_{frp} / \sqrt{f_{con}'}} \tag{5.21}$$

Using boundary conditions, the parameters M and N are found to be: (detailed derivation is given in appendix B)

$$M = -\frac{P}{b} \cdot \frac{\lambda}{\tanh(\lambda l_e)} \tag{5.22}$$

$$N = \lambda \frac{P}{b} \tag{5.23}$$

Substituting Equations 5.22, 5.23 in Equation 5.20, yields bond stress expression:

$$\tau(x) = \frac{P\lambda}{b} \cdot \left[ -\frac{1}{\tanh(\lambda l_e)} \cosh(\lambda x) + \sinh(\lambda x) \right] \tag{5.24}$$

Integrating Equation 5.11, tensile stress distribution of hybrid laminate within effective length can be expressed as (detail in appendix B):

$$f_{frp}(x) = \frac{P}{b \cdot t_{frp}} \cdot \frac{\sinh[\lambda(l_e - x)]}{\sinh(\lambda l_e)} \tag{5.25}$$

$$\varepsilon_{frp}(x) = \frac{P}{b \cdot t_{frp} \cdot E_{frp}} \cdot \frac{\sinh[\lambda(l_e - x)]}{\sinh(\lambda l_e)} \tag{5.26}$$

### 5.2.2 Interfacial fracture energy

Based on bond fracture mechanics, interfacial energy $G_f$ is defined as the area under bond stress-slip curve, which is expressed as (Dai and Ueda, 2003):

$$G_f = \int_0^{le} \tau(x) ds \tag{5.27}$$

Interfacial slip is the displacement difference between FRP laminate and concrete, which can be obtained by Equation 5.16, combining Equation 5.13 and 5.16, we have:

$$ds = \frac{t_{adh}}{G_{adh}} d\tau(x) \tag{5.28}$$

Differentiating Equation 5.20 to get:

$$d\tau(x) = [M \cdot \lambda \cdot \sinh(\lambda x) + N \cdot \lambda \cdot \cosh(\lambda x)] \cdot dx \tag{5.29}$$

Substituting Equations 5.22, 5.23, 5.28, and 5.29 into Equation 5.27, considering boundary conditions at x = $l_e$ and x = 0, the interfacial energy $G_f$ can be expressed as (detail in appendix B):

$$G_f = \frac{1}{2} \cdot \frac{P^2}{b^2 \cdot E_{frp} \cdot t_{frp}} \cdot (1 + \frac{E_{frp} A_{frp}}{E_{con} A_{con}}) \tag{5.30}$$

### 5.2.3 Effect of effective length on bond stress distribution

Since effective length can have different expression (Teng et al., 2001), its effect on bond stress distribution is examined. In Equation 5.24, $l_e$ is involved in the term $\tanh(\lambda l_e)$, which remains constant 1 when $l_e$ is larger than about 40 mm as given in Table 5.2 (λ is constantly determined by material properties, Eq.5.19). Because all effective lengths from different expressions are larger than 40mm, under a given load, their stress distribution curves are independent on effective length because of the characteristic of hyperbolic function.

**Table 5.8: Effect of effective length on tanh(λle) ( ta = 1.0mm, λ = 0.159 )**

| le | 10.0 | 20.0 | 30.0 | 40.0 | 50.0 | 60.0 |
|---|---|---|---|---|---|---|
| tanh (λle) | 0.9201 | 0.9965 | 0.9999 | 1.00 | 1.00 | 1.00 |

Figure 5.5 compares bond stress distributions for different effective lengths (Equations 5.23) under various load level. It shows the bond stress distribution was nearly identical for different effective length, after which bond stress approximately remained zero.

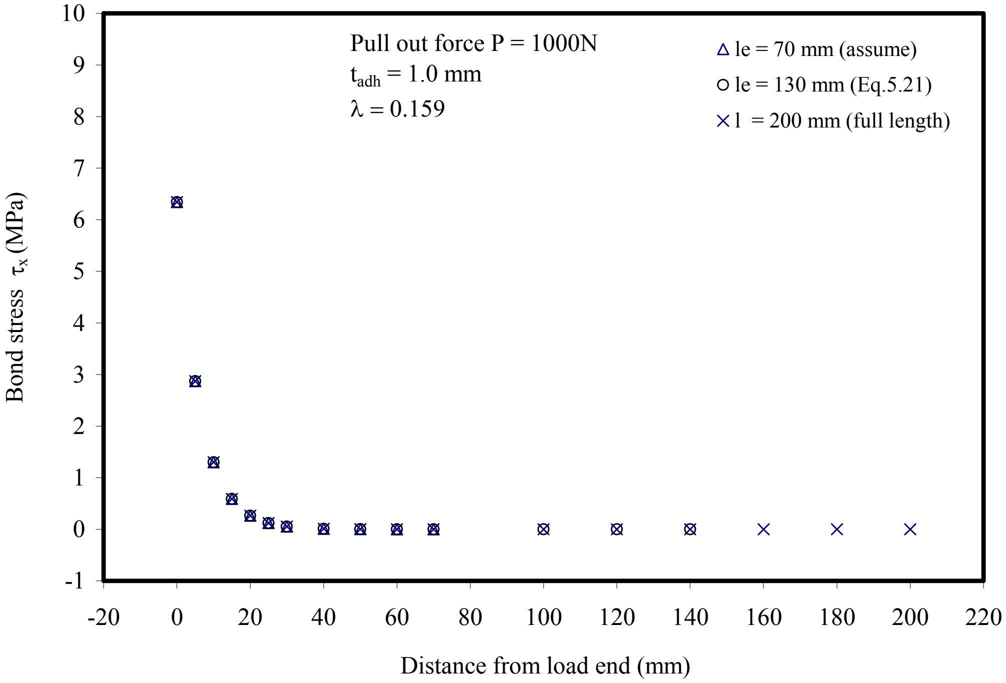

**(a) P=1000 N**

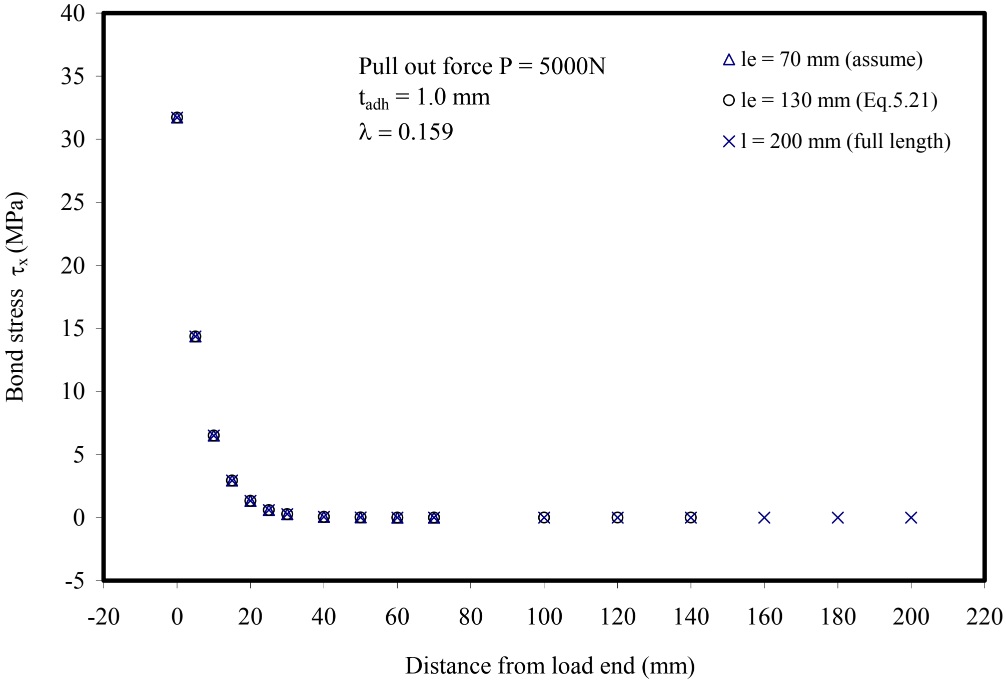

**(b) P=5000N**

**Fig. 5.5: Comparison bond stress distribution for different bond length**

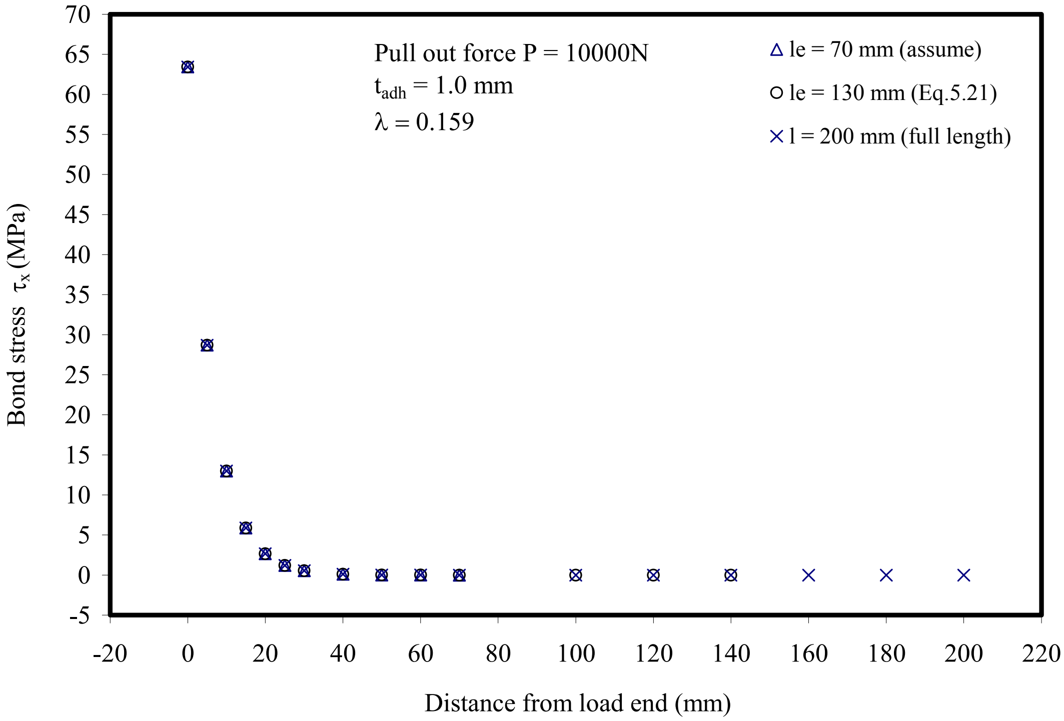

**(c) P=10000N**

**Fig. 5.5 (cont.): Comparison bond stress distribution for different bond length**

### 5.2.4 Effect of adhesive thickness on bond strain

The influence of adhesive thickness on bond stress is represented by parameter λ in Equation 5.24. The dependence of bond stress on adhesive thickness is shown in Figure 5.6. It is found that bond stress becomes smaller if adhesive layer is thicker. At load end, the thinnest joint (ta =0.5 mm) has the highest bond stress while the thickest one has the smallest. When the curves reach to about 8 mm away from load end, the trend changes in a reverse manner, in which thicker joints distribute bond stress more evenly.

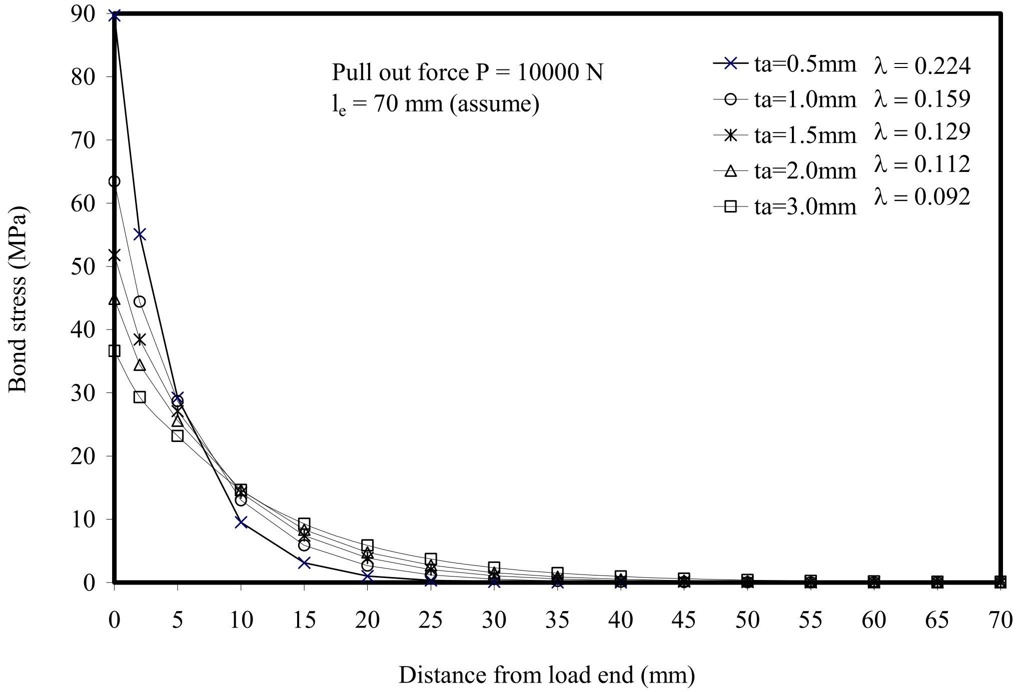

**Fig. 5.6: Effect of joint thickness on bond stress**

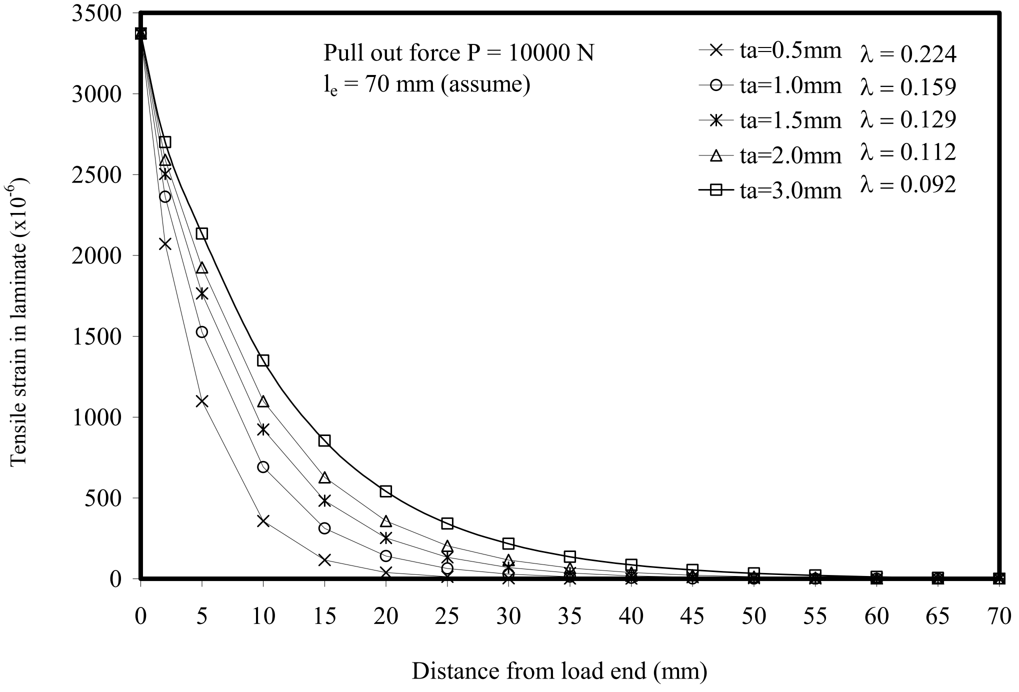

**Fig. 5.7: Effect of adhesive thickness on tensile stress of laminate**

Figure 5.7 shows the effect of adhesive thickness on tensile stress distribution in FRP laminate based on Equation 5.26. It displays tensile stress of laminate are more uniform distribution if adhesive is thicker. Wet-bond has thicker epoxy adhesive than dry-bond (Table 4.3), and the effect of thickness of adhesive layer was supported experimentally by comparing strain distribution of laminates along bond area for typical wet-bond (B2W2) and dry-bond (B2D4) samples in Figure 5.8. It is noted that at very early loading stage (P≤2kN), tensile strain distributions of laminate for both type of bonds are approximately identical. But starting from 4 kN, their difference became obvious indicating wet-bond had more uniform distribution than dry-bond. When load reached 6 kN, sudden increase in strain at 40 mm of wet-bond indicates initial debonding occurred and propagated to 40 mm, while the strain of 80 mm still remain zero showing it was well bonded with concrete. At higher 8 kN, strain at 80 mm of wet-bond rose up but that of dry-bond remain at zero, which distinguishes the earlier adhesive crack of wet-bond.

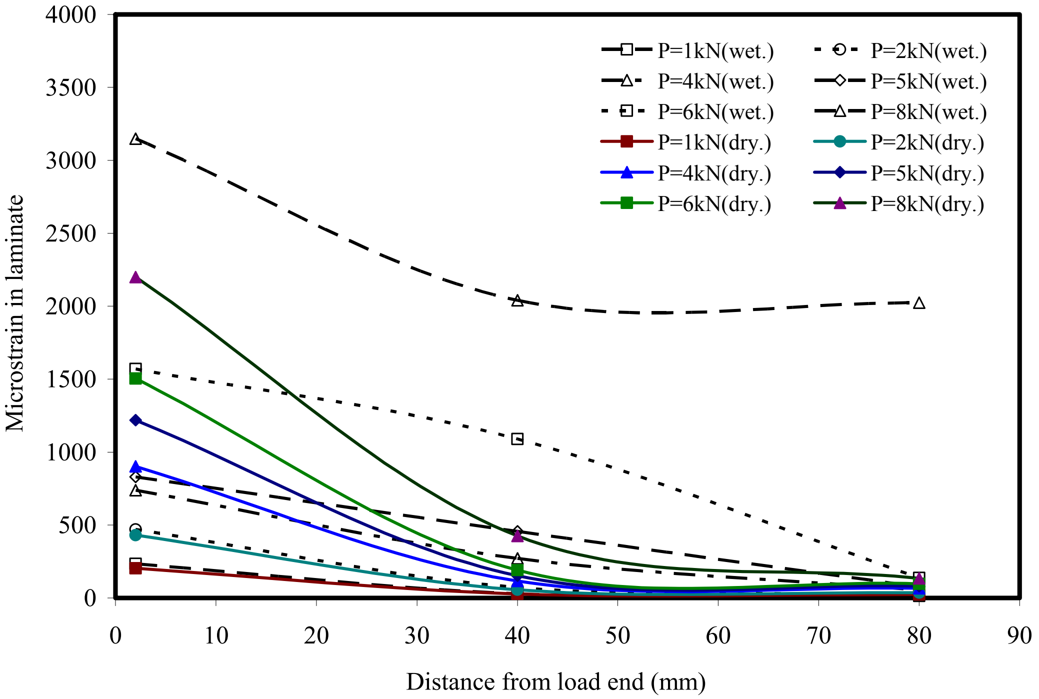

**Fig. 5.8: Comparison of tensile strain distribution between wet-bond and dry-bond**

As in the previous discussion, once debonding occurs, the debonded laminate deforms like coupon undergoing tensile force only and the tensile strain along debonded laminate should be very close. Figure 5.8 shows there are strain difference between 2 mm and 40 mm, but not for strain between 40 mm and 80 mm. It is probably that under 8 kN, along debonded laminate, interlock action contributed to the friction between laminate and aggregate, which prevent laminate from freely deformation. But at load end (2 mm), there was less aggregates that can provide the friction where debonded laminate stretch without constrain.

### 5.2.5 Comparison of analytical and experimental results

The analytical bond stress or tensile strain distribution is valid for laminate bonded to concrete either for wet-bond or dry-bond. The difference in thickness of adhesive layer was involved in the parameter λ. In Figure 5.9, comparison between analytically predicted tensile strain of FRP laminate and experimental results is given. It shows that for wet-bond in Fig. 5.9a, the model prediction agrees well with experiments before initial debonding occurs, after which deformation of laminate was affect by tensile force and interlock friction and the distribution is not suitable for debonded laminate. Compared with wet-bond, tensile strain distribution of laminate also follows the analytical modeling well for dry-bond. Figure 5.9 b shows that even at high load level, laminate still bonded to concrete. The small deviation of experimental data and theoretical curve at 40 mm of dry-bond under 6kN and 8kN is likely because that experimentally at high load, there was micro-crack of concrete substrate that could reduce the bond capability.

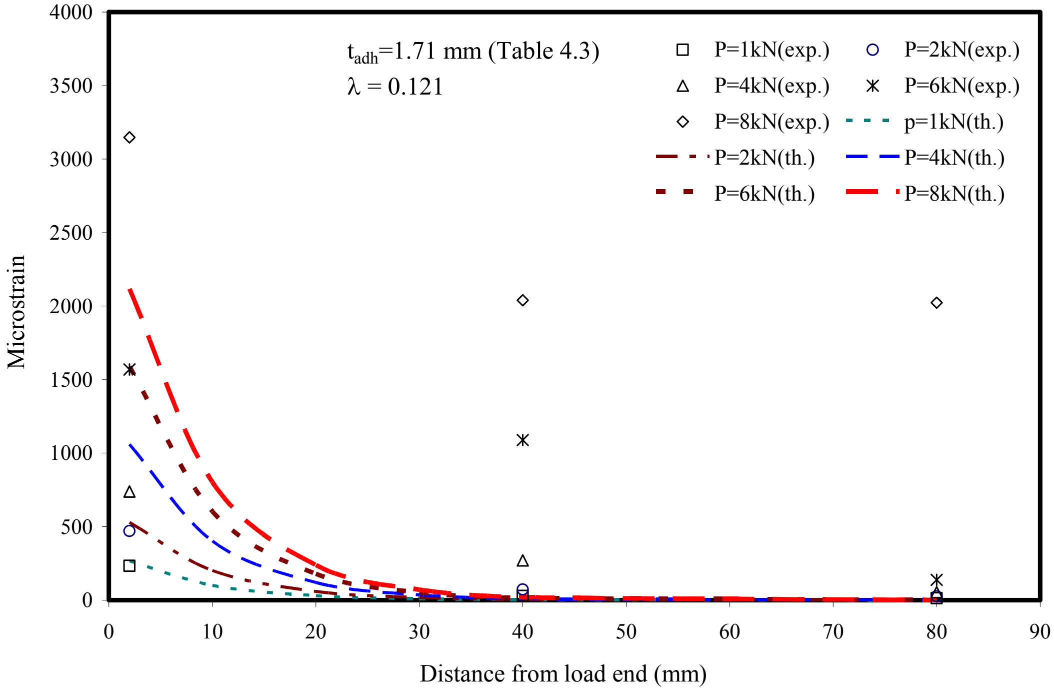

**(a) wet-bond**

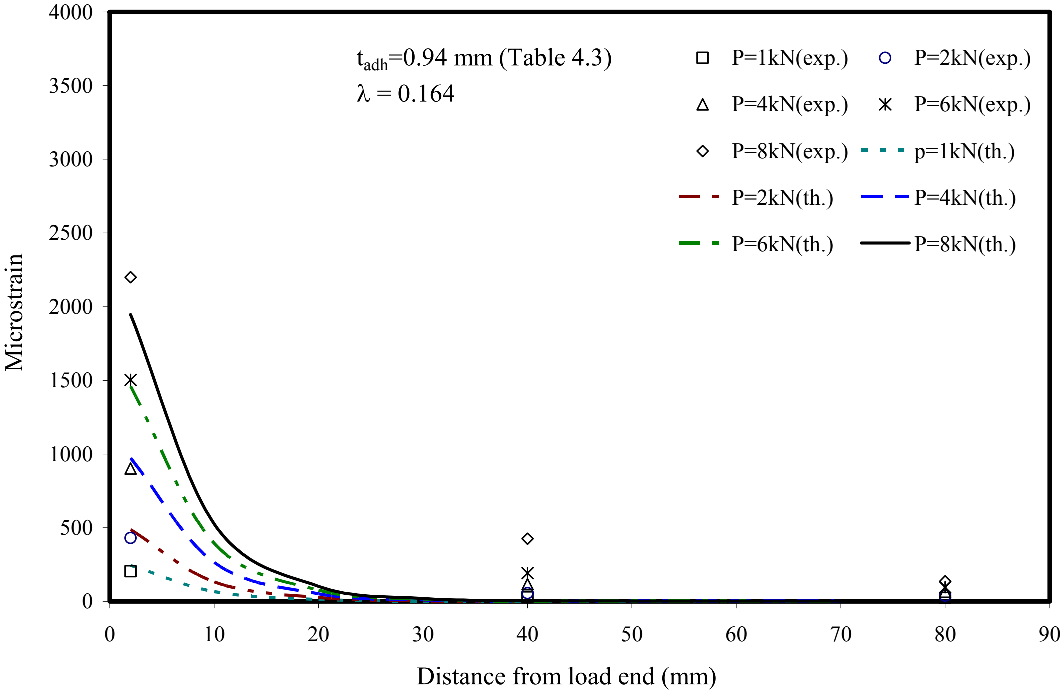

**(b) dry-bond**

**Fig. 5.9: Comparison of experimental and numerical strain distribution**

## 5.2.6 Debonding process simulation

### 5.2.6.1 Failure Mode I

The schematic of failure Mode I is shown in Figure 5.10. The simulation of the failure process is described in flow chart in Figure 5.11. Carbon fibre fractures around 4000$\mu\varepsilon$ outside bond area while the strain of bonded laminate is much smaller. The tensile strain of laminate at load end (2 mm) is determined by Equation 5.25 and compared with experimental result in Figure 5.12. During the following process, glass fibre elongation and reloading is the typical behaviour of hybrid materials. A calculated example is shown in Appendix C.

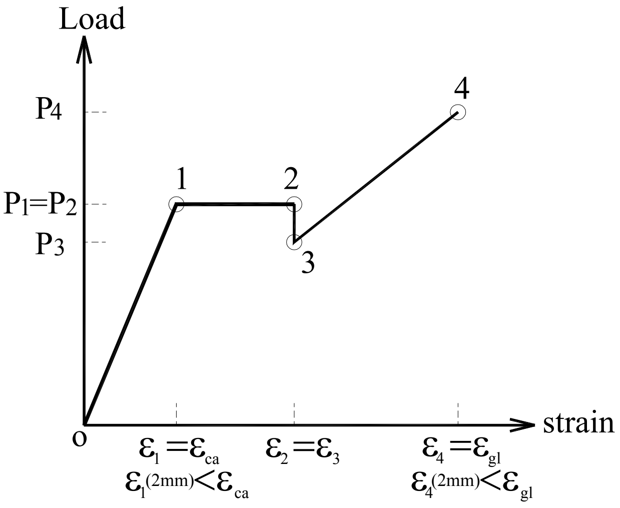

**Fig. 5.10: Schematic description of failure Mode I**

In Figure 5.10, the strains ($\varepsilon_1$~ $\varepsilon_4$) at key points are at the plane of carbon fibre fracture, which is different from the strain at 2 mm ($\varepsilon_{1(2mm)}$ ~ $\varepsilon_{4(2mm)}$) within bonded area. Because in Mode I, carbon cracking always happens before initial debonding, where strain at 2 mm still follow bond stress distribution. After carbon fractures, glass elongation and initial debonding, laminate at 2 mm is not bonded to concrete anymore, strain of laminate is accumulated during reloading stage by Rule of Mixture.

Linear elastic deformation to carbon fibre fracture

$$P_1 = t_1 \times b \times E_1 \times \varepsilon_{ca} \qquad \text{Eq.5.1}$$

↓

Strain of laminate at 2 mm from load end

$$\varepsilon_{frp}{}^{1}(2mm) = \frac{P_1}{b \cdot t_1 \cdot E_1} \cdot \frac{\sinh\left[\lambda(l_e - 2)\right]}{\sinh(\lambda l_e)} \qquad \text{Eq.5.26}$$

↓

Glass fibre elongation

$$\Delta\varepsilon_{gl} = \varepsilon_{ca} \cdot \left(\frac{t_1}{t_2} - \frac{E_2}{E_1}\right) \qquad \text{Eq. 5.6}$$

↓

After elongation, the strain of laminate at 2 mm point

$$\varepsilon_{frp}{}^{2}(2mm) = \varepsilon_{frp}{}^{1}(2mm) + \Delta\varepsilon_{gl}$$

↓

Strain at carbon crack point after elongation

$$\varepsilon_2 = \varepsilon_{ca} + \Delta\varepsilon_{gl} \qquad \text{Eq.5.7}$$

↓

Load drop to $P_3$, $\varepsilon_2 = \varepsilon_3$

$$P_3 = \varepsilon_2 \cdot E_2 \cdot t_2 \cdot b \qquad \text{Eq.5.8}$$

↓

$$P_4 = 0.427\beta_{frp}\beta_L\sqrt{f_c'}b_{frp}L_e \qquad \text{Eq.2.1}$$

↓

Strain at 2mm increase with reloading

$$\varepsilon_{frp}{}^{4}(2mm) = (P_4 - P_3)/(E_2 \cdot t_2 \cdot b) + \varepsilon_{frp}{}^{2}(2mm) \qquad \text{Eq.5.9}$$

**Fig. 5.11: Flow chart of prediction for Mode I**

It is noted that, because the ultimate strain of glass fibre was never reached in pullout test, the peak load is determined by empirical Equation 2.1. The prediction of failure process of Mode I (2 mm) is given in Figure 5.11 and its comparison with experimental results shown in Figure 5.12 and Table 5.3.

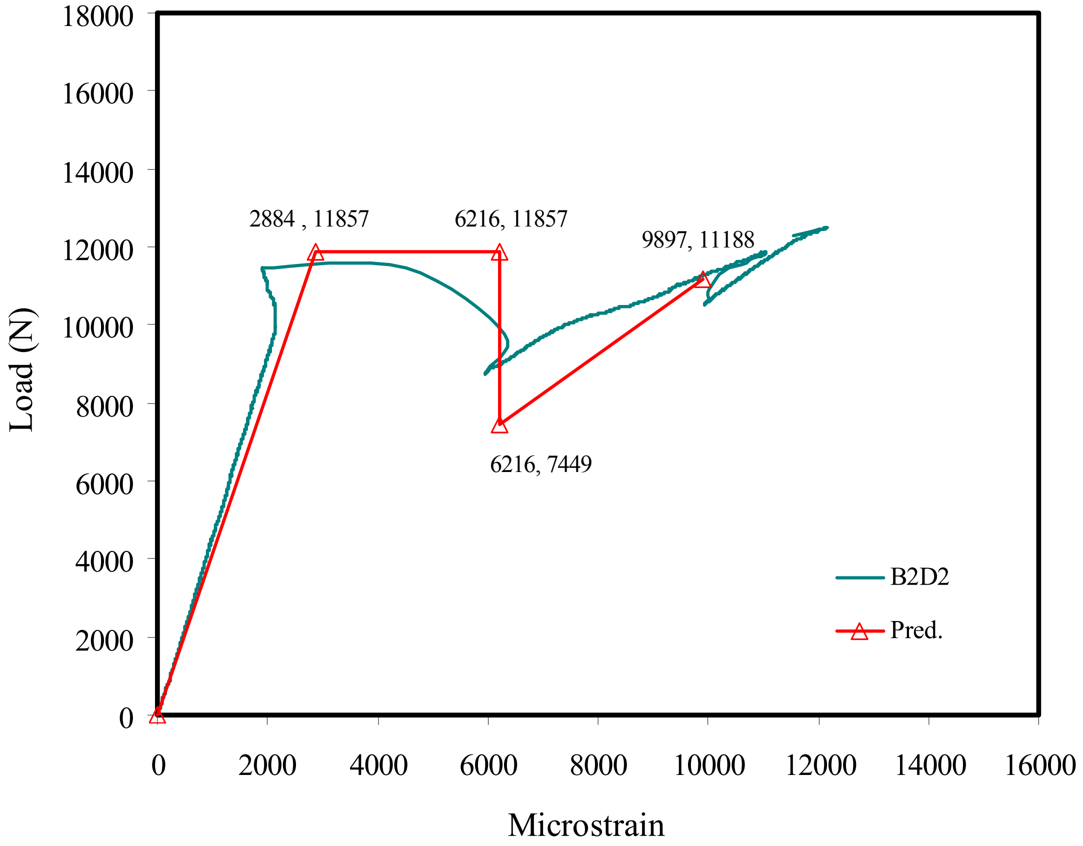

**Fig. 5.12: Comparison of experiment and analytical prediction for failure Mode I**

### 5.2.6.2 Failure Mode II

The flow chart for prediction failure Mode II is given in Figure 5.14, almost all samples of wet-bond and dry-bond with environmental exposure failed in Mode II except hot water aging and wet-bond sample of 50 cycles wet/dry exposure. Based on Table 4.5 and Table 4.6, the ratio of initial debonding load to peak load is summarized in Table 5.1, which tells that initial debonding is approximately 54~71% of peak load in this case. In failure Mode II, initial debonding happens first and is followed by a carbon fibre fracture. So, strain of laminate reaches ultimate strain of 4000με at carbon fracture. Based on the model, the strain at 2 mm before initial debonding can be calculated. Predicted failure process of Mode II is compared with typical sample in Figure 5.15. The input data includes ultimate strain of carbon fibre and ultimate pullout force $P_4$ estimated by Equation 2.1 and the ratio from Table 5.3.

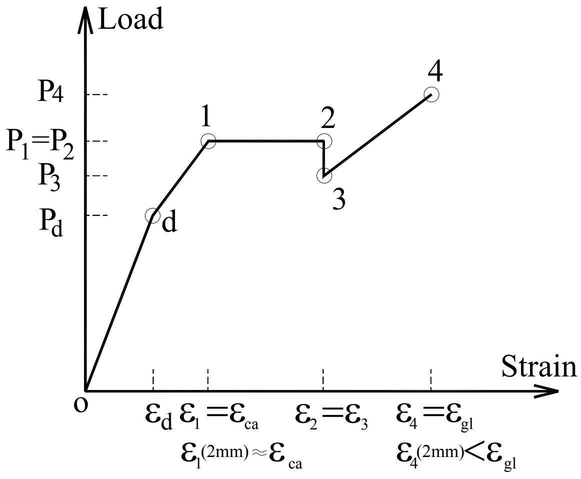

**Fig. 5.13: Schematic description of failure Mode II**

In Figure 5.13, the strain ($\varepsilon_1$~ $\varepsilon_4$) represents the strain at 2 mm point from loaded end. In Mode II, carbon cracking always happen after initial debonding, before which laminate tensile strain at 2 mm point still follow bond stress distribution and it could be predicted by corresponding initial debonding load, after which laminate is separated from concrete, it deforms freely under tensile force like coupon. When carbon fibre cracks, the strain of 2mm could reach ultimate strain of carbon (4000με) and follows the process of typical hybrid composite. As in Mode I, the ultimate strain of glass fibre is never reached in pullout test, the peak load is determined by empirical Equation 2.1. The prediction of failure process of Mode II (2 mm) is given in Figure 5.11 and its comparison with experimental result is shown in Figure 5.15 and in Table 5.3.

Initial debonding load is approximately 60% of peak load

$$P_4 = 0.427\beta_{frp}\beta_L\sqrt{f_c'}b_{frp}L_e \qquad \text{Eq.2.1}$$

$$P_d = 60\%P_4$$

↓

Strain at 2 mm when initial debonding occur

$$\varepsilon_{frp}{}^{d}(2mm) = \frac{P_d}{b \cdot t_1 \cdot E_1} \cdot \frac{\sinh[\lambda(l_e - 2)]}{\sinh(\lambda l_e)} \qquad \text{Eq.5.26}$$

↓

Debonded laminate deformed to carbon fracture

$$\varepsilon_{frp}{}^{1}(2\text{ mm}) = \varepsilon_{ca}$$

$$P_2 = t_1 \times b \times E_1 \times \varepsilon_{ca} \qquad \text{Eq.5.1}$$

↓

Glass fibre elongation

$$\Delta\varepsilon_{gl} = \varepsilon_{ca} \cdot (\frac{t_1}{t_2} - \frac{E_2}{E_1}) \qquad \text{Eq. 5.6}$$

↓

After elongation, the strain of laminate at 2 mm

$$\varepsilon_{frp}{}^{2}(2mm) = \varepsilon_2 = \varepsilon_{ca} + \Delta\varepsilon_{gl} \qquad \text{Eq.5.7}$$

↓

Load drop to $P_3$, $\varepsilon_2 = \varepsilon_3$

$$P_3 = \varepsilon_2 \cdot E_2 \cdot t_2 \cdot b \qquad \text{Eq.5.8}$$

↓

Strain at 2 mm increase with reloading

$$\varepsilon_{frp}{}^{4}(2mm) = (P_4 - P_3)/(E_2 \cdot t_2 \cdot b) + \varepsilon_{frp}{}^{2}(2mm) \qquad \text{Eq.5.9}$$

**Fig. 5.14: Flow chart of prediction for Mode II**

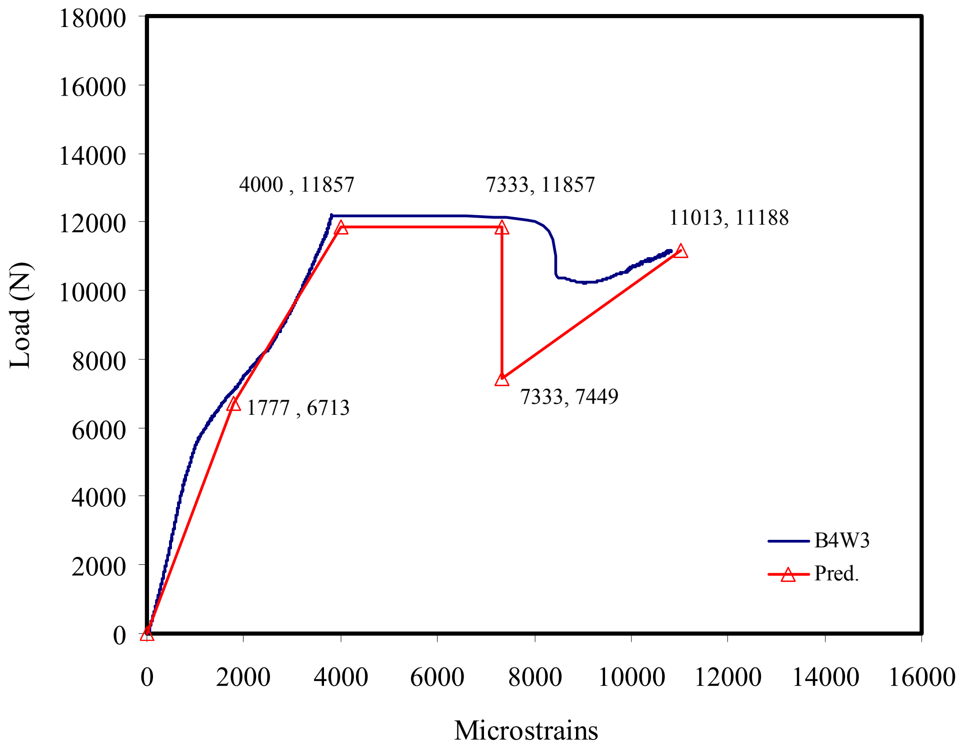

**Fig. 5.15: Comparison of experiment and analytical prediction for failure Mode II**

Table 5.3 shows the initial debonding loads are around 50% to 70% of peak loads in most samples with various environmental conditions. For dry-bond in group B2, initial debonding follow carbon fracture, which is as high as 95% of peak load.

**Table 5.9: Initial debonding load (IDL) and peak load (PL)**

| Groups | Wet-bond | | | Dry-bond | | |
|---|---|---|---|---|---|---|
| | IDL (N) | PL (N) | IDL/PL | IDL (N) | PL (N) | IDL/PL |
| B2 | 6035 | 10325 | 58% | 10992 | 11562 | 95% |
| B3 | 7731 | 11973 | 65% | 7608 | 10648 | 71% |
| B4 | 5661 | 10558 | 54% | 7616 | 12052 | 63% |
| B5 | 5996 | LF | NA | 8629 | LF | NA |
| B6 | 4869 | 9033 | 54% | 5166 | 10752 | 48% |

Note: The data in table 5.3 come from experiment
IDL = initial debonding load; PL = peak load;
LF = laminate failure; NA = not available

### 5.2.6.3 Failure Mode III

Since there is no carbon fracture involved in Mode III, failure is only caused by debonding. The ultimate pullout force is lower than in Mode I and Mode II. Because of the weak bond, carbon can not reach its ultimate fracture strain. From Table 4.5, the peak load of wet-bond belonging to failure Mode III is about 10000 N, of which the initial debonding happens around 55%~60%. It is worth to mention that ultimate bond strength by Equation 2.1 is not suitable for this case and the input peak load is obtained from experimental result. Based on modeling, the strain at 2 mm before initial debonding can be calculated, and predicted bond behaviour is compared with typical sample of Mode III in Figure 5.18 (Detail in appendix C). The flow chart of prediction steps is given in Figure 5.17. In this case, since Pd and P4 are based on experimental results and empirical equation, theoretical prediction is mainly for strain distribution.

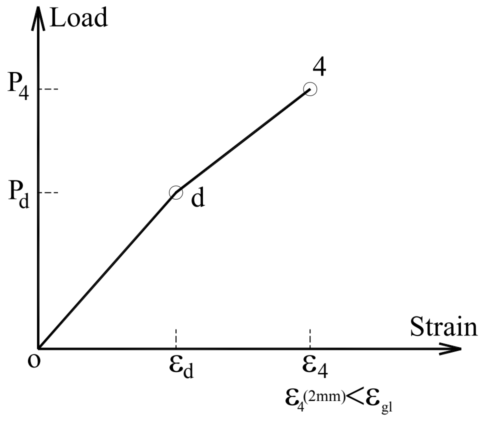

**Fig. 5.16: Schematic description of failure Mode III**

Initial debonding load is approximately 55% of peak load, the average peak load $P_4$ of Mode III is around 10kN from experiment result (Table 5.3)

$$P_d = 55\% P_4$$

↓

Strain at 2 mm when initial debonding occurs

$$\varepsilon_{frp}^{\ d}(2mm) = \frac{P_d}{b \cdot t_1 \cdot E_1} \cdot \frac{\sinh[\lambda(l_e - 2)]}{\sinh(\lambda l_e)} \qquad \text{Eq.5.26}$$

↓

Strain at 2 mm increases during debonding propagation

$$\varepsilon_{frp}^{\ 4}(2mm) = \frac{P_4}{b \cdot t_1 \cdot E_1}$$

**Fig. 5.17: Flow chart of prediction for Mode III**

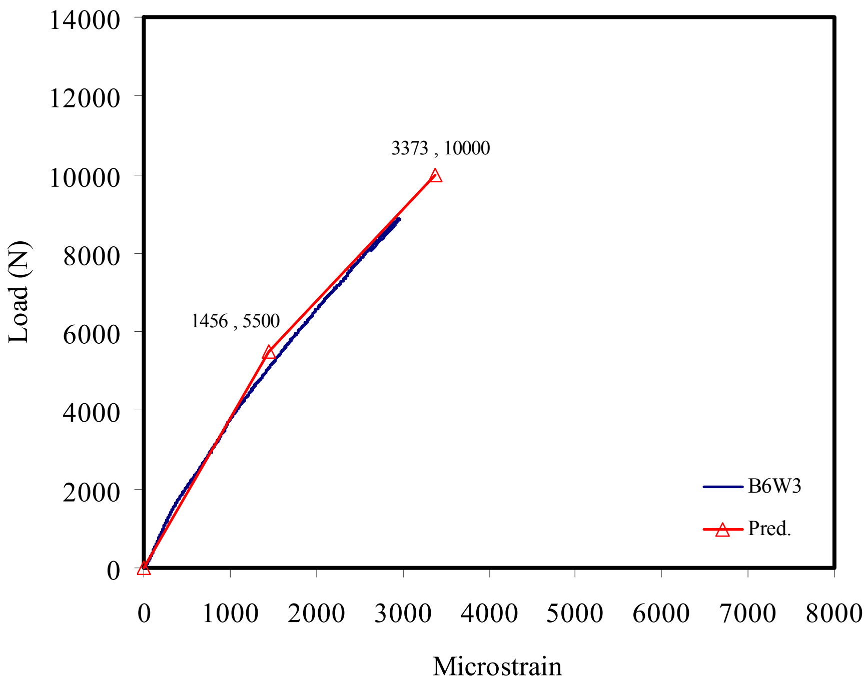

**Fig. 5.18: Comparison of experiment and analytical prediction for failure Mode III**

### 5.2.7 Interfacial fracture energy

Above discussion suggests that behaviour of hybrid composite-to-concrete sample has two important parts, one is carbon fibre fracture and the other is bond cracking. It is clear that carbon fibre fracture always happens outside bond area, which is an independent process to bond. As a criterion to qualify bond strength, interfacial fracture energy is decided by maximum pullout load. Interfacial energy of all samples for wet-bond and dry-bond is summarized in Table 5.4 (Equation 5.30). It shows that the dry-bond after freeze-thaw cycle has the highest interface energy and wet-bond with continuous cold exposure is the next, followed by the dry-bond without any environmental conditions. Compared with dry-bond in same group, interfacial energy of wet-bond samples is 26.5% higher for continuous cold temperature exposure, while it is 30%~20% less in other conditions. It seems wet-bond technique can work well in cold region.

**Table 5.10: Interfacial fracture energy comparison**

| Group | Durability exposure | Fracture energy (N/mm) | | |
|---|---|---|---|---|
| | | Wet-bond | Dry-bond | Wet-bond /dry-bond |
| B2 (refer.) | - | 0.731 | 0.916 | 79.8% |
| B3 (low temp.) | Cold temp. | 0.983 | 0.777 | 126.5% |
| B4 (freeze/thaw) | Freeze/thaw | 0.764 | 0.995 | 76.8% |
| B5 (hot water) | Hot water | Laminate failure | | |
| B6 (wet/dry) | Wet/dry | 0.559 | 0.792 | 70.6% |

## 5.3 Conclusions

Depending on the occurring sequence of carbon fibre fracture and initial debonding, three failure modes are simulated. Typical samples are compared with analytical analysis and the results are of close. The following conclusions are drawn:

- Behaviour of hybrid FRP material is well predicted by analytical simulation. Ultimate strains of carbon and glass fibre in hybrid composite are the control parameters. Glass fibre elongation and temporary load drop are determined by modeling in quantity, which has not been done by previous research.
- Because ultimate strain of glass fibre has never reached in pullout test, peak load was determined by empirical Equation 2.1, which shows that empirical predicted bond strength is very close to average experimental results.
- In failure Mode I and Mode II, carbon fibre fracture always occurs outside bond area or in debonded zone. Glass elongation and load drop is attributed to the hybrid behaviour, which can be simulated by simple modeling.
- After initial debonding, the tensile strain distribution in debonded zone can be predicted by rule of mixture in tension.
- Based on interfacial fracture energy comparison, except for low temperature exposure, wet-bond interfacial fracture energy is lower than dry-bond by 20% to 30%.

# Chapter 6 Conclusions and Recommendation

## 6.1 Conclusions

Bond behaviour of hybrid FRP laminate to cast-in-place concrete were investigated. Wet-bond and dry-bond samples were compared in terms of their bond performance, bond mechanism and durability capacity. Analysis of three main failure modes was conducted. The following conclusions can be drawn:

1) Compared to single material, the behaviour of hybrid composite is more complicated. Its tensile failure normally includes three different stages: linear elastic deformation, carbon fibre fracture and glass fibre elongation, and load drop until glass fibre fracture. The whole process can be predicted numerically.

2) Bond mechanism of wet-bond is different from dry-bond. Although both bonds have adhesive bond strength and interlock strength, wet-bond is dominated more by mechanical interlock between aggregate and adhesive, which results in earlier initial debonding in wet-bond than in dry-bond.

3) Three failure modes were observed for hybrid composite bonded with concrete. Carbon fibre fracture and initial debonding are predominant to classify different failure stages. Dry-bond with no environmental exposure is characterized by carbon fracture first followed by debonding, while wet-bond and dry-bond samples after environmental exposures experience debonding initiation followed by carbon fibre fracture. Wet-bond without environmental exposure fails in debonding only.

4) Environmental condition has effect on bond quality. Compared with dry-bond, the

durability of wet-bond is enhanced in continuous cold temperature but decreased in other conditions.

5) Based on interfacial energy criterion, dry-bond after freeze-thaw cycles is the best and wet-bond with continuous cold exposure the second, followed by dry-bond without any environmental conditions. It is likely that wet-bond technique is particularly suited to cold region applications.

6) Water entrapped in adhesive has no influence on DOC and Tg of epoxy, but it introduces significant porosity at adhesive interface, which weakens adhesive bond strength of wet-bond. The final wet-bond strength is nevertheless compensated by interlock mechanism.

7) High temperature and moisture induced much more deterioration of hybrid laminate than that of bond, which cause hybrid laminate failure instead of bond failure.

## 6.2 Recommendation for future work

1) Initial debonding in this project was identified by video and load-strain curve. But it was not very clear for some samples and a better method to identify initial debonding should be developed.

2) Four different environmental exposures were tested, but for hot water condition group it was difficult to evaluate bond strength because laminate failed first. More durability conditions and longer exposure time should be designed for comprehensive examination of wet-bond durability.

3) Investigation into different epoxy systems as adhesive and as hybrid laminate matrix should be conducted.

4) Porosity of epoxy adhesive surface caused by moisture has great influence on bond interface, low water to cement ratio for wet-bond should be preferred and investigation is needed to determine the optimal water-cement ratio.

5) Investigation into fatigue capacity of wet-bond is necessary.

6) More work should be done to reduce porosity of epoxy adhesive surface and increase the wet-bond quality.

7) Further study should be done about the feasibility of using wet-bond technique in the field for full sized specimens.

# References

Anstice, P. D., Beaumont, P. W. R. (1983). “Direct observation of the failure and toughness of hybrid composites”, *Journal of materials science letters*, 617-622.

Achintha, P.M.M., and Burgoyne, C.J., (2006) “Fracture mechanics of plate debonding”, *The Tenth East Asia-Pacific Conference on Structural Engineering and Construction*, Bangkok, Thailand.

Abanilla, M.A., Li, Y. and Karbhari, V.M. (2005). “Durability characterization of wet layup graphite/epoxy composites used in external strengthening”, *Composites Part B: Engineering,* Volume 37, Issues 2-3, 200-212.

Belarbi, A., Chandrashekhara, K. and Watkins, S.E. (1996). “Smart composite rebar with enhanced ductility”. *Proc. 11th Conference, engineering mechanics, American society of civil engineers*, New York, N.Y. 788-791.

Brosens, K., Van G. D. (1998). “Plate end shear design for external CFRP laminates”, Proceedings of FRAMCOS-3. *Freiburg, Germany: Aedificatio Publisher,* pp.1793-1804.

Burgueno, R., Davol, A., Zhao, L., Seible, F., and Vistasp M. K. (2004). “ Flexural behavior of hybrid fibre-reinforced polymer/concrete beam/slab bridge component”, *ACI structural journal,* V. 101, n 2, March, 228-236.

Bakis, C.E., Nanni, A., Terosky, J.A, Koehler, S.W., (2001). “Self-monitoring, pseudo-ductile, hybrid FRP reinforcement rods for concrete applications”, *Composites science and technology*, 61, 815-823.

Bayasi, Z. and Kaiser, H. (2003). “Flexural behaviour of composite concrete slabs using carbon fibre laminate decks.” *ACI materials journal,* V. 100, n 4, July, 274-279.

Barbero, E.J. (1999). “Introduction to composite material design”, *Philadelphia, Department of mechanical & aerospace engineering*, West Virginia University, of PA: Taylor and Francis, c1999.

Bizindavyi, L., and Neale, K.W. (1999). “Transfer lengths and bond strengths for composites bonded to concrete”, *Journal of composites for construction*, Nov.1999, 153.

Blaschko, M. (1997). "Strengthening with CFRP." *Münchner Massivbau Seminar*, TU

München (in German).

Canadian council for public-private partnerships, “Infrastructure investment deficit”, from http://www.pppcouncil.ca/issues_infraDeficit.asp.

Ching A. and Büyüköztürk, O. (2006). “Peel and Shear Fracture Characterization of debonding in FRP Plated Concrete Affected by Moisture”, *Journal of composites for construction* © ASCE, 35-47.

Chajes, M.J. Finch, W.W., Januszka, T.F. and Thomson, T.A. (1996). “Bond and force franfer of composite material plates bonded to concrete”, *ACI Struct.J.*,93(2), 208-217.

Chen, J. F. and Teng, J.G. (2001). “Anchorage strength models for FRP and steel plates bonded to concrete”, *Journal of Structural Engineering*, Vol. 127, No. 7.

Chajes, M.J., Thomson, T.A. and Farschman, C.A. (1995). “Durability of concrete beams externally reinforced with composite fabrics”, *Construction and building materials* Vol.9, No.3, 141-148.

Chou, T.W. and Kelly, A. (1980). “Mechanical properties of composites”, *Master. Sci.*,10, 229-59.

Dai, J. G., and Ueda, T. (2003). "Local bond stress slip relations for FRP sheets-concrete interfaces." *Proc., 6th Int. Symp. on FRP Reinforcement for Concrete Structures*, National Univ. of Singapore, Singapore, 143–152.

Dutta, P.K. and Hui, D. (1996). “Low-temperature and freeze-thaw durability of thick composites”, Composites Part B: Engineering, Volume 27, Number 3, 371-379.

Foster, S.J., Khomwan, N. and Smith, S.T. (2005). “Determination of bond stress versus slip for externally bonded FRP from standardized bond strength tests”, *Proceedings of international symposium on bond behaviour of FRP in structures,* 85-90.

Grace, N.F., Ragheb, W.F., and Abdel-Sayed G. (2004). "Strengthening of Cantilever and Continuous Beams Using New Triaxially Braided Ductile Fabric," *ACI Structural Journal* Vol. 101, No. 2, 237-244.

Green, M. F., Bisby, L. A., Beaudoin, Y. and Labossiere, P. (2005). “Effect of freeze-thaw cycles on the bond durability between fibre reinforced polymer plate reinforcement and concrete”, *Journal of Composite for Construction*, Volume 9, Issue 4, 348-359.

Harris, H. G.., Somboonsong, W., and Ko, F.K. (1998). “New ductile hybrid FRP reinforcing bar for concrete structures”, *Journal of composites for construction*, 28-37.

Hall, J. E. and Mottram, J.T. (1998). "Combined FRP Reinforcement and Permanent Formwork for Concrete Members", *Journal of Composites for Construction*, Vol. 2, No. 2, 78-86.

Haque, A., Mahmood, S., Walker, L. and Jeelani, S. (1991). "Moisture and temperature induced Degradation in Tensile properties of Kevlar-Graphite/Epoxy Hybrid Composites", *Journal of Reinforced plastics and composites,* Volume 10, 132.

Kirk,J.N., Munro, M. and Beaumont, P.W.R. (1978). "The fracture energy of hybrid carbon and glass fiber composites", *Journal of materials science,* Volume 13, 2197-2204.

Karbhari, V.M., and zhao, L. (1998). "Issues related to composite plating and environmental exposure effects on composite – concrete interface in external strengthening", *Composite Structure*, 40(3-4), 293-304.

Kajorncheaoounngam, S., Gupta, R.K. and GangaRao, H.V.S. (2002). "Effect of aging environment on degradation of glass-reinforced epoxy", *Journal of composites for construction*, Feb., 61-68.

Karbhari, V.M. and Zhao, L. (1997). "Issues related to composite plating and environmental exposure effects on composite-concrete interface in external strengthening", *Composite Structures*, Volume 40, 293-304(12).

Lu, X.Z., Teng, J.G., Ye, L.P. and Jiang, J.J.(2005). "Bond-slip models for FRP sheets/plates bonded to concrete", *Engineering structures,* 27, 920-937.

Lopez-Anido, R., Michael, A.P. and Sandford, T.C. (2004). "Freeze-thaw resistance of fiber-reinforced polymer composites adhesive bonds with underwater curing epoxy", *Journal of materials in civil engineering*, May, 283.

Leung, C.K.Y. and Pan, J.L. (2005). "Effect of concrete composition on FRP/concrete bond capacity", *Proceedings of the international symposium on bond behaviour of FRP in structures,* BBFS 2005, 69-76.

Maeda, T., Asano, Y., Sato, Y., Ueda, T., and Kakuta, Y. (1997). "A study on bond mechanism of carbon fiber sheet." *Proc., 3rd Int. Symp. of Non-Metallic (FRP) Reinforcement for Concrete Structures*, Japan Concrete Institute (JCI), Tokyo (1), 279–286.

Maria A. A., Yan L. and Vistasp, M. K. (2006). "Durability characterization of wet layup graphite/epoxy composites used in external strengthening", *Composites, Part B: engineering*, 37, 200-212.

Mufi, A.A., Newhook, J.P. and Tadros, G. (1996). "Deformability versus ductility in concrete beams with FRP reinforcement" *Advanced composite materials in bridges and structures*, Montreal, Canada. 189-199.

Mukhopadhyaya, O., Swamy, R.N. and Lynsdale, C.J. (1998). "Influence of aggressive exposure conditions on the behavior of adhesive bonded concrete-GFRP joints", *Construction and Build*, Mater 12, 427-446.

Manders, P.W. and Bader, M.G. (1981). "The strength of hybrid glass/carbon fiber composites", *Journal of materials science*, 16, 2233-2245.

Nanni, A., Henneke, M.J. and Okamoto, T.(1994). "Tensile properties of hybrid rods for concrete reinforcement", *Construction and Building Materials*. 8(1), 27-34.

Pellegrino, C., Boschetto, G., Timazzi, D. and Modena, C. (2005). “Progress on understanding bond behaviour in RC elements strengthened with FRP”, *Proceedings of the international symposium on bond behaviour of FRP in structures,* BBFS, 63-68.

Petrie, E. M.(2006). “Epoxy adhesive formulations”, New York: McGraw-Hill, c2006, ISBN, 978 0071 45544 2.

Park, R. and Paulay, T. (1976). “Reinforced Concrete Structures”.

Qiao, P.Z. and Xu, Y.W. (2004). “Effects of freeze-thaw and wet-dry conditionings on the mode-I fracture”, *Earth and Space*, 601-608.

Qu, Z., Lu, X.Z. and Ye, L.P.(2005). “Size effect of shear contribution of externally bonded FRP U-jackets for RC beams”, *Proceedings of International Symposium on Bond Behaviour of FRP in Structures (BBFS 2005),* 371-380.

Razaqpur A.G. and Ali, M.M.(1996). “A new concept for achieving ductility in FRP-reinforced concrete”, *Proc. First Int. Conf. on Compos*, Univ. of Arizona, Tucson, Ariz, 401-413.

Sato, N., Kurauchi, T. and Kamigaito, O. (1986). “Fracture mechanism of unidirectional carbon-fibre reinforced epoxy resin composite”, *Journal of materials science,* V21, 1005-1010.

Stefanidis, S., Mai, Y.W. and Cotterell, B. (1985). “The specific work of fracture of carbon/Kevlar hybrid fibre composites”, *Journal of materials science letters,* Volume 4, 1033-1035.

Shao, Y., Wu, Z.S. and Zhu, H.T. (2005). "FRP-concrete composite beams using wet-bond technology", *Annual Conference of Japan-SAMPE*, Tokyo, December, CDROM.

Shao, Y., Wu, Z. S. and Bian, J. (2005). "Wet-bonding between FRP laminates and cast-in-place concrete", *Proceedings of the International Symposium on Bond Behaviour of FRP in Structures* (BBFS), 91-96.

Taljsten, B. (1997). "Defining anchor lengths of steel and CFRP plates bonded to concrete", *Int. J. Adhesives*, 17(4), 319-327.

Toutanji, H.A. and Ortiz, G. (2001). "The effect of surface preparation on the bond interface between FRP sheets and concrete members", *Composite Structure,* 53, 457-462.

Toutanji, H.A. and Gomez, W. (1997). "Durability characteristics of concrete beams externally bonded with FRP composite sheets", *Cement and Concrete Composites*, Volume 19, Number 4, 351-358.

V. Tamuzs and R. Tepfers, (1996). "Ductility of hybrid fiber composite reinforcement FRP for concrete", *Fiber Composites in Infrastructure, Proc. 1st International Conference on Composites in Infrastructure*, University of Arizona, Tuscon (AZ), 109–122.

Wu, H.C., Fu, G.k., Gibson, R.F., Yan, A., Warnemuende, K., and Anumandla, V. (2006). "Durability of FRP composite bridge deck materials under freeze-thaw and low temperature conditions", *Journal of bridge engineering*, 443-451.

Wu, L.X., Hoa, S. V., Tan, M. and That, T. (2004). "Effects of Water on the Curing and Properties of epoxy adhesive used for bonding FRP composite sheet to concrete", *Journal* *of Applied Polymer Science*, Vol. 92, 2261–2268.

Wu, Z.S., Yuan, H., Yoshizawa, H. and Kanakudo, T. (2001). "Experimental/analytical study on interfacial fracture energy and fracture propagation along FRP-concrete interface", *Fracture mechanics for concrete materials*, ACI SP 201-8, 133-152.

Wu, Z.S., Yuan, H. and Niu, H.(2002). "Stress transfer and fracture propagation in different kinds of adhesive joints", *Journal of engineering mechanics*, Volume 128, Issue 5, 562-573.

Wu, Z., Shao, Y., Iwashita, K. and Sakamoto, K. (2007) "Strengthening of preloaded RC beams using hybrid carbon sheets", ASCE Journal of Composites for Construction, 11(3) p. 299-307.

Wu,H.C., Fu,G.K., Gibson,R.F., Yan,A., Warnemuende, K. and Anumandla, V.(2006). "Durability of FRP Composite Bridge Deck Materials under Freeze-Thaw and Low Temperature Conditions", *J. Bridge Engrg.*, Volume 11, Issue 4, 443-451.

Yuan, H., Teng, J.G., Seracino, R., Wu, Z.S. and Yao, J., (2004). "Full-rang behaviour of FRP-to-concrete bonded joints", *Journal of engineering structures*, 26, 553-565.

Zhang, B.R. and Benmokrane, B. (2002). "Pullout Bond Properties of Fiber-Reinforced Polymer Tendons to Grout", *Journal of materials in civil engineering*, 399.

# Appendix A: Test data and graphs

## Table A.1 Experimental results

| Samples | | Initial debond | | Carbon crack | | Peak load | | carbon crack position | Failure mode |
|---|---|---|---|---|---|---|---|---|---|
| No. | | Strain | Load (N) | Strain | Load (N) | Strain | Load | | |
| B2 | W1 | 889 | 6200 | 2089 | 9025 | 4771 | 11102 | -20mm | 2 |
| | W2 | 1263 | 5463 | -- | -- | 3384 | 9294 | -- | 3 |
| | W3 | 2526 | 6443 | -- | -- | 4342 | 10580 | -- | 3 |
| | D1 | 2486 | 9607 | 2412 | 9708 | 2413 | 9709 | 0mm | 1 |
| | D2 | 2124 | 11395 | 2098 | 11395 | 12144 | 12499 | 0mm | 1 |
| | D3 | 2000 | 10940 | 2000 | 10940 | 2923 | 11037 | 0mm | 1 |
| | D4 | 3340 | 12025 | 3340 | 12027 | 2956 | 13003 | 0mm | 1 |
| B3 | W1 | 1903 | 6832 | 4406 | 12352 | 4406 | 12352 | 65 & 120mm | 2 |
| | W2 | 5200 | 8329 | 2283 | 9612 | 11674 | 11619 | 0mm | 2 |
| | W3 | 2169 | 8031 | 2609 | 9823 | 13501 | 11949 | 0 & 40mm | 2 |
| | D1 | 2982 | 7633 | 3972 | 9503 | 4168 | 9639 | not obvious | 2 |
| | D2 | 1821 | 6497 | -- | -- | 3676 | 10298 | -- | 3 |
| | D3 | 1956 | 8695 | 2628 | 9541 | 10000 | 12009 | 17 & 70mm | 2 |
| B4 | W1 | 1585 | 4391 | -- | -- | 3242 | 8712 | -- | 3 |
| | W2 | 1205 | 6004 | 3821 | 12179 | 3820 | 12201 | 4mm | 2 |
| | W3 | 2815 | 6587 | 4001 | 12193 | 4001 | 12193 | 2mm | 2 |
| | D1 | 2673 | 7055 | 4443 | 10726 | 12590 | 12485 | 10mm | 2 |
| | D2 | 2408 | 8391 | 2103 | 11451 | 3560 | 12615 | 40mm | 2 |
| | D3 | 2935 | 7401 | 4825 | 10923 | 4893 | 11055 | 22 & 95mm | 2 |
| B5 | W1 | 1345 | 4577 | 4118 | 8293 | 7950 | 8517 | 15mm | 2 |
| | W2 | -- | 6904 | -- | 7766 | -- | 7792 | 5mm | 2 |
| | W3 | 1973 | 6701 | 3233 | 9798 | 3224 | 9799 | 20mm | 2 |
| | D1 | 2776 | 7105 | 2211 | 7073 | 4489 | 9446 | not obvious | 1 |
| | D2 | 3172 | 10447 | 3393 | 11733 | 3386 | 11751 | 0mm | 2 |
| | D3 | 2108 | 8335 | 2108 | 8430 | 9422 | 10336 | 5mm | 2 |
| B6 | W1 | 1199 | 3678 | -- | -- | 2375 | 8326 | -- | 3 |
| | W2 | 2043 | 7247 | -- | -- | 4041 | 9887 | -- | 3 |
| | W3 | 952 | 3681 | -- | -- | 2948 | 8885 | -- | 3 |
| | D1 | 671 | 3511 | -- | -- | 4211 | 7542 | 20 mm | 2 |
| | D2 | 688 | 5471 | 2400 | 7485 | 4050 | 12262 | 43 mm | 2 |
| | D3 | 1797 | 6515 | 3534 | 9473 | 11801 | 12451 | 0mm | 2 |

## Figure A.1~A.20: Load-strain, load-slip curves of pullout test

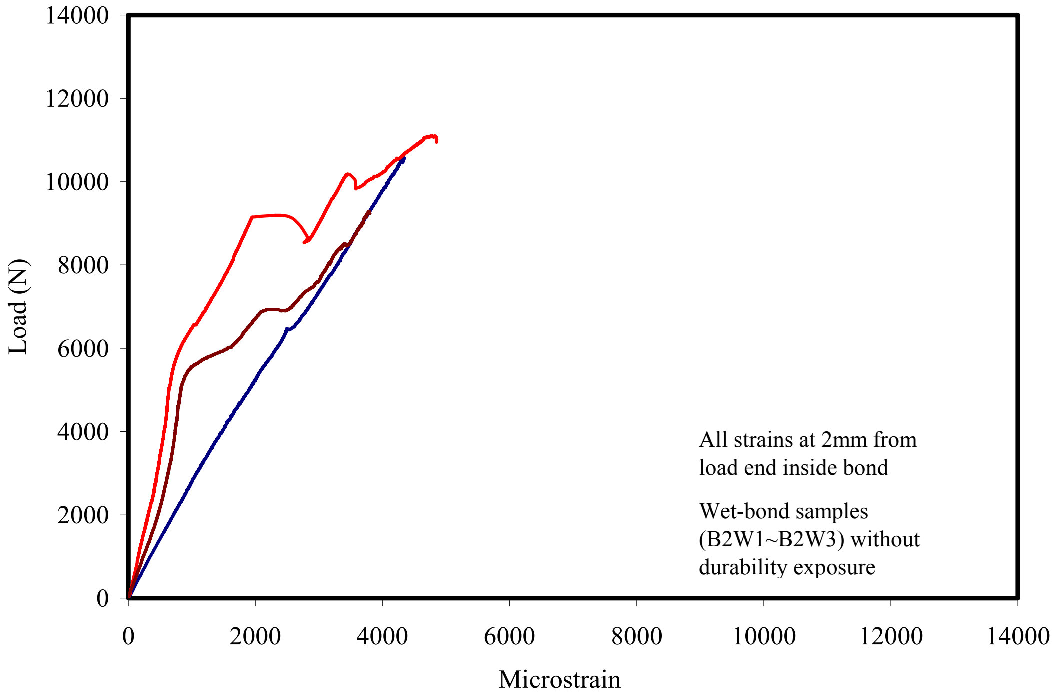

**Fig.A.1: Load-strain relation of wet-bond without exposure (B2)**

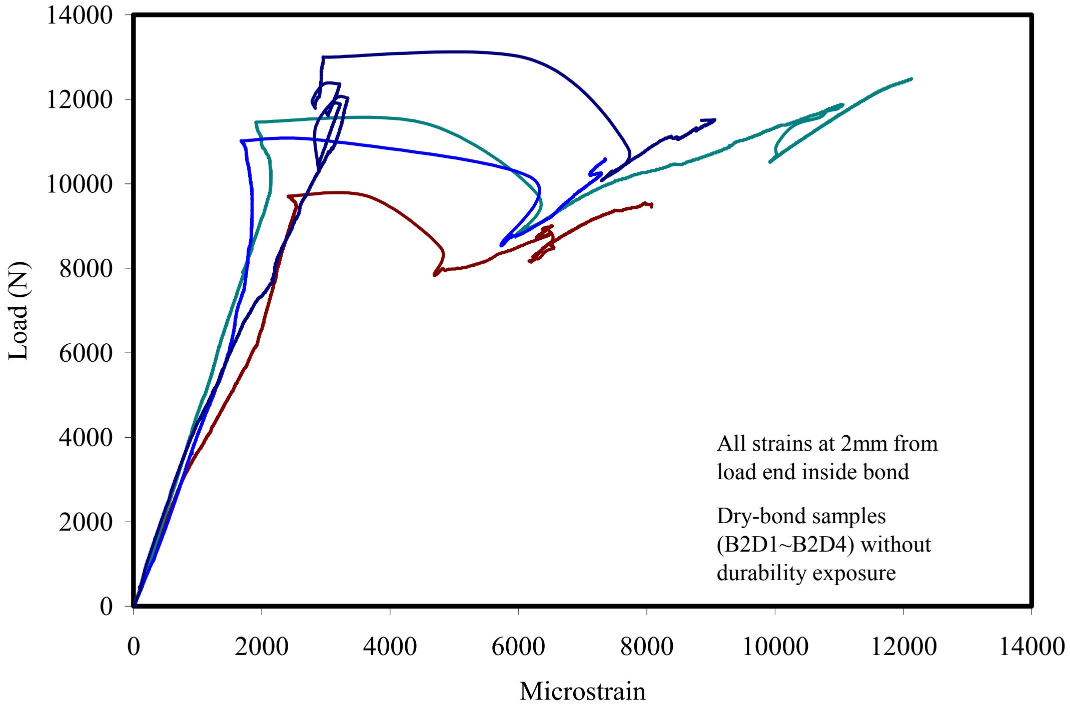

**Fig.A.2: Load-strain relation of dry-bond without exposure (B2)**

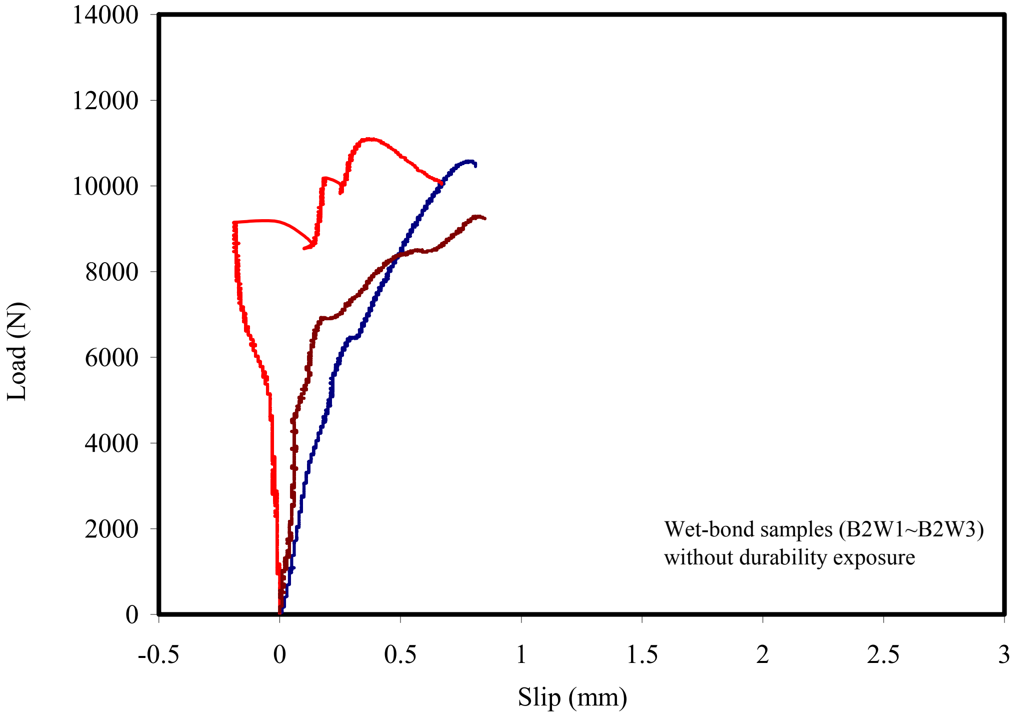

Fig.A.3: Load-slip relation of wet-bond without exposure (B2)

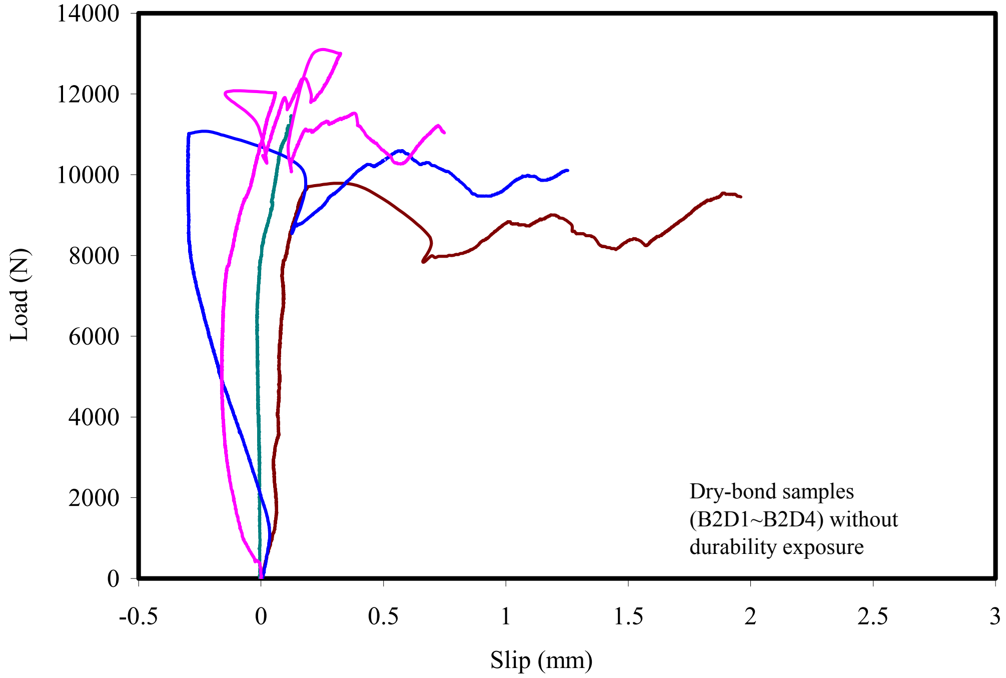

Fig.A.4: Load-slip relation of dry-bond without exposure (B2)

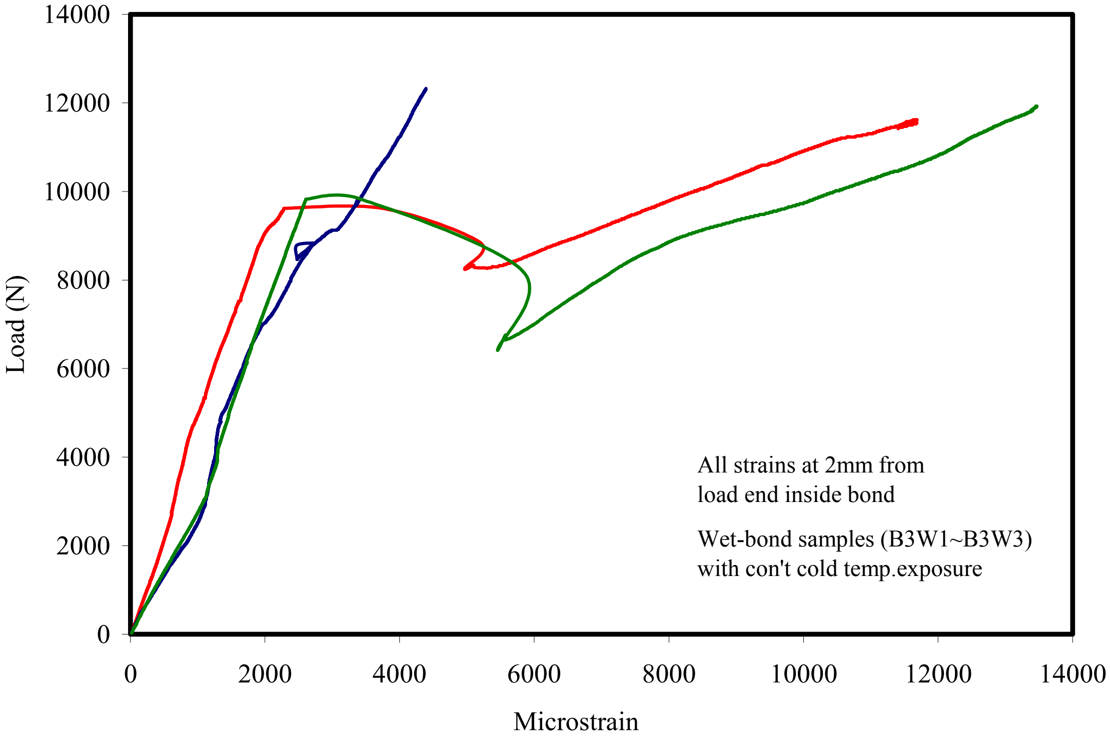

Fig.A.5: Load-strain relation of wet-bond with low temp. exposure (B3)

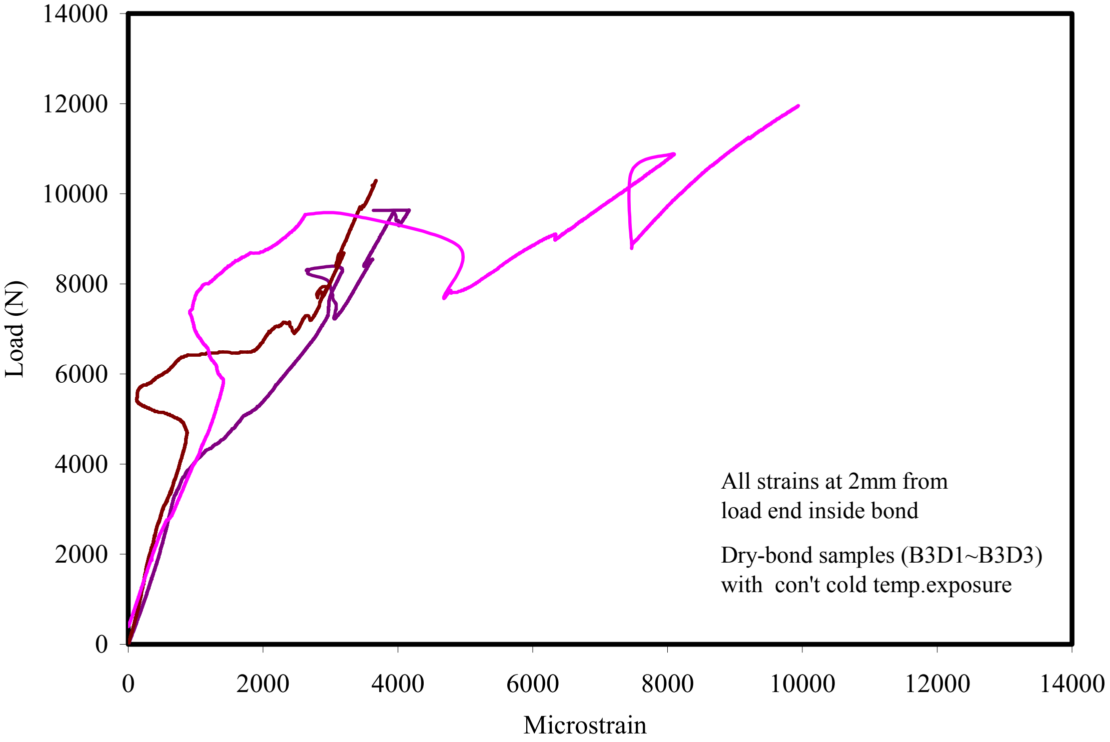

Fig.A.6: Load-strain relation of dry-bond with low temp. exposure (B3)

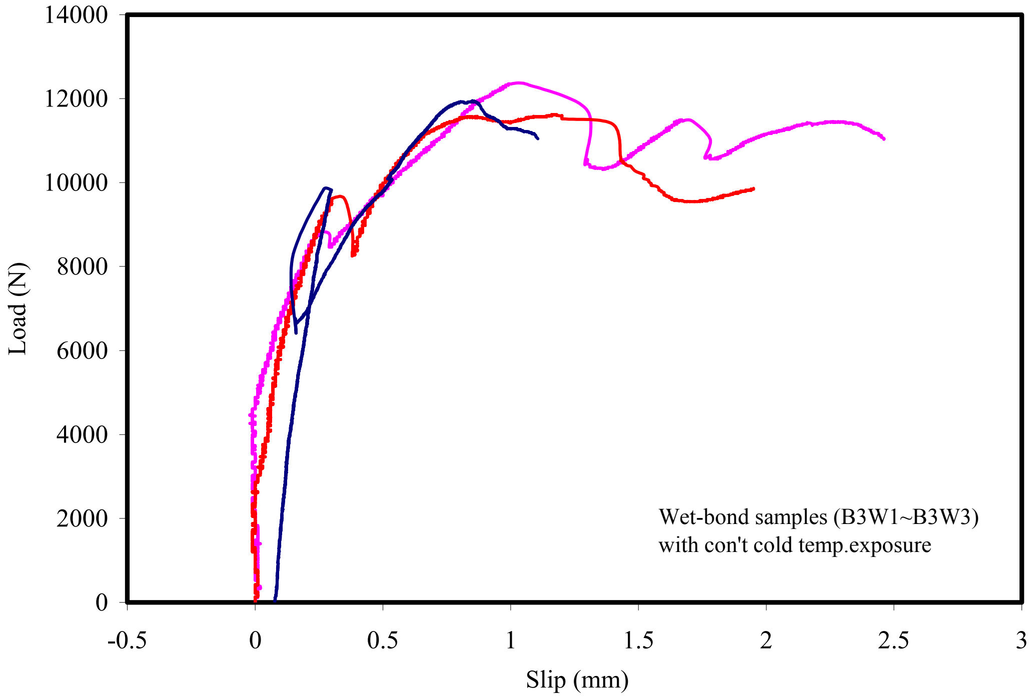

**Fig.A.7: Load-slip relation of wet-bond with low temp. exposure (B3)**

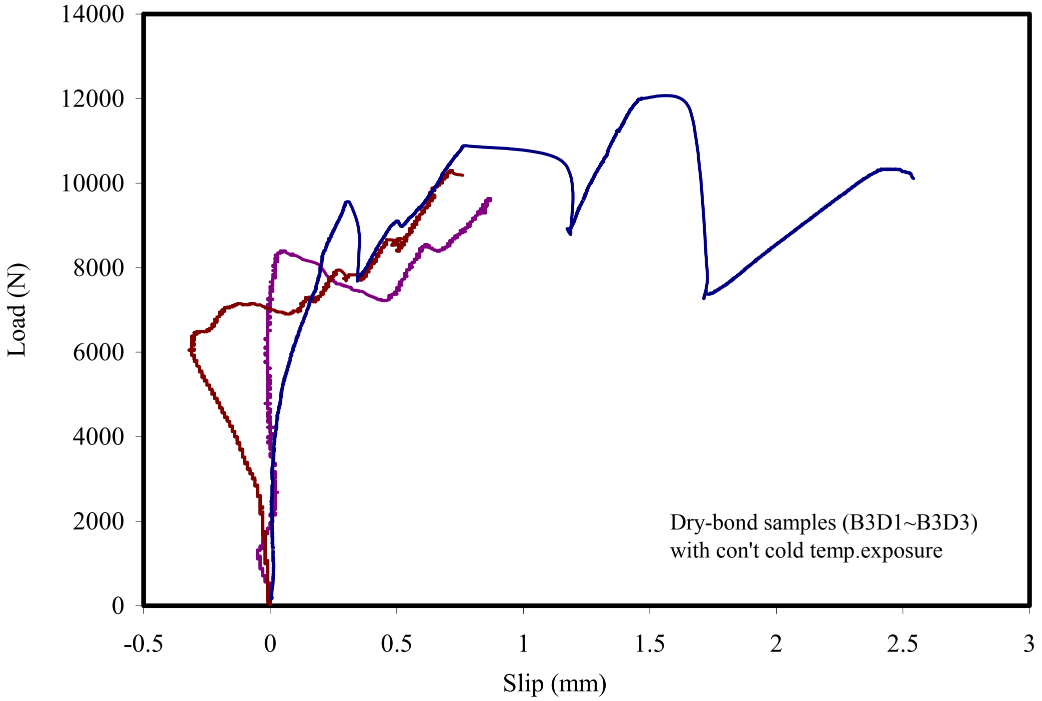

**Fig.A.8: Load-slip relation of dry-bond for low temp. exposure (B3)**

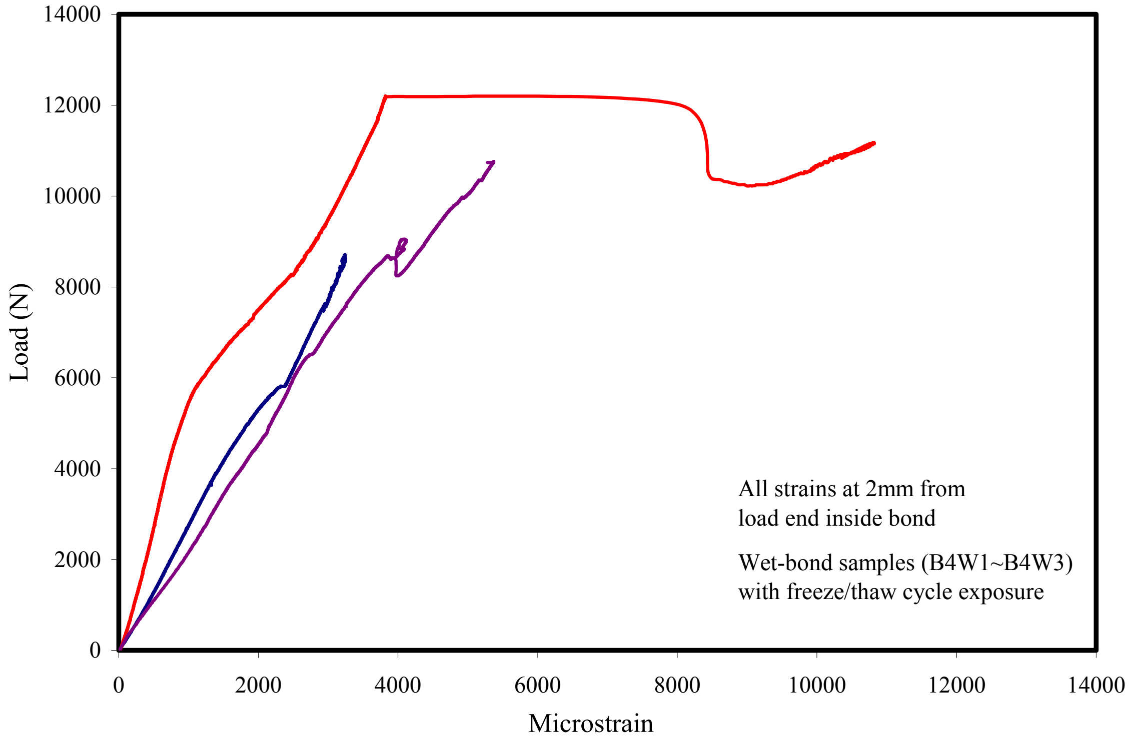

Fig.A.9: Load-strain relation of wet-bond with freeze/thaw cycle exposure (B4)

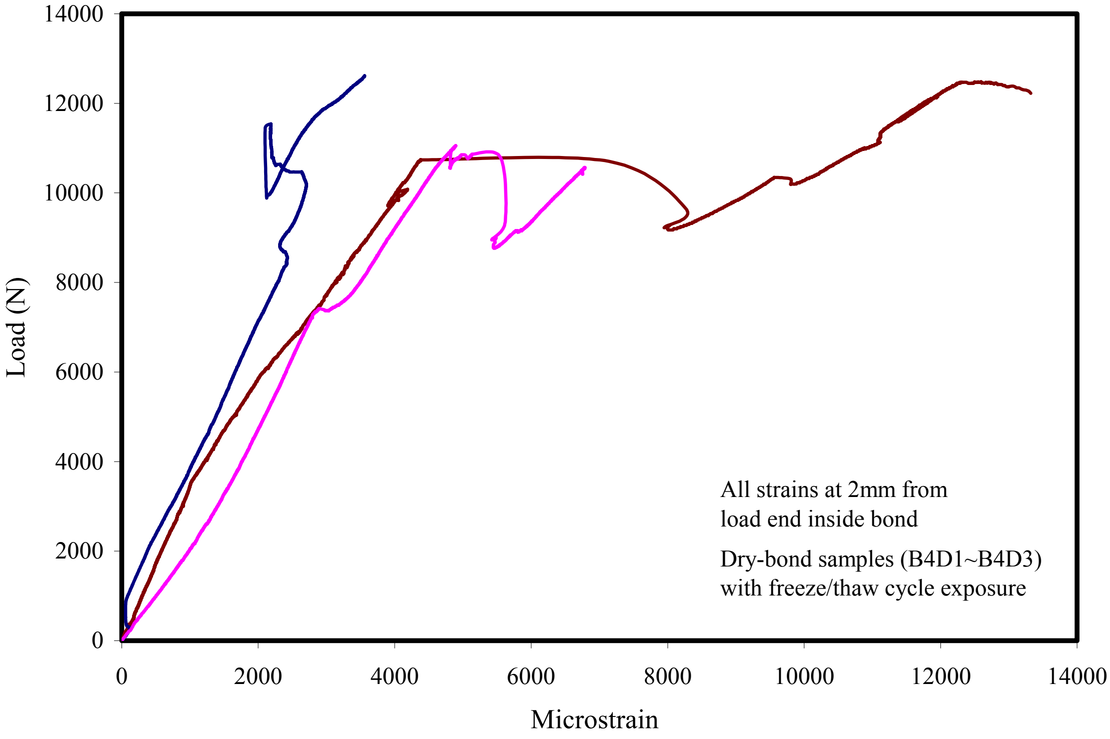

Fig.A.10: Load-strain relation of dry-bond with freeze/thaw cycle exposure (B4)

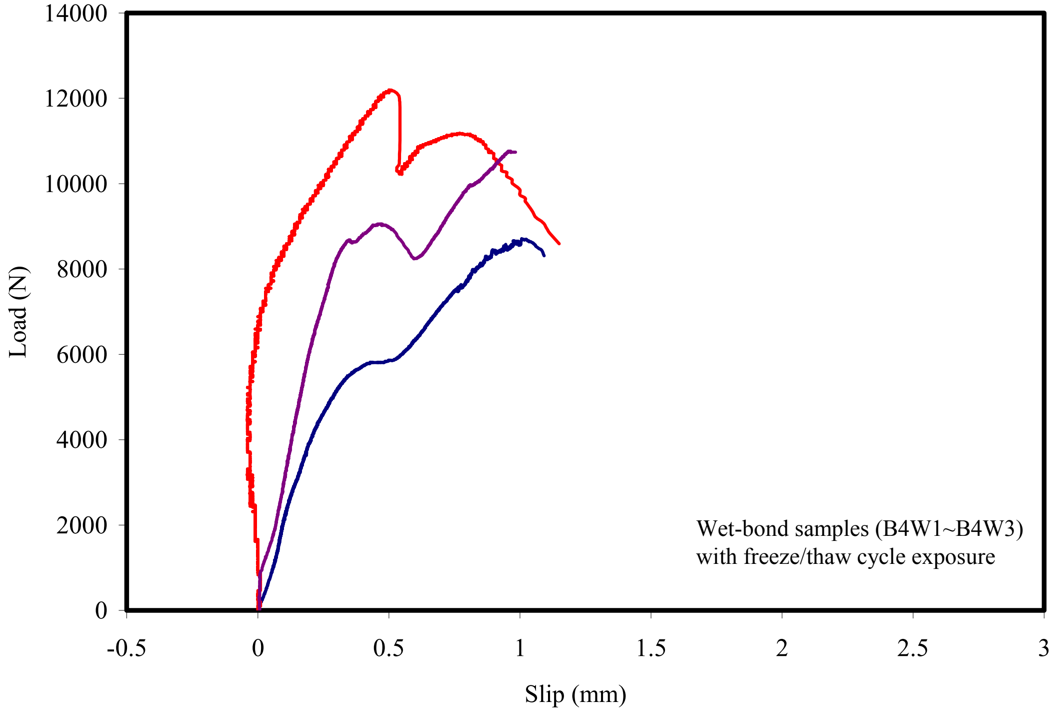

Fig.A.11: Load-slip relation of wet-bond with freeze/thaw cycle exposure (B4)

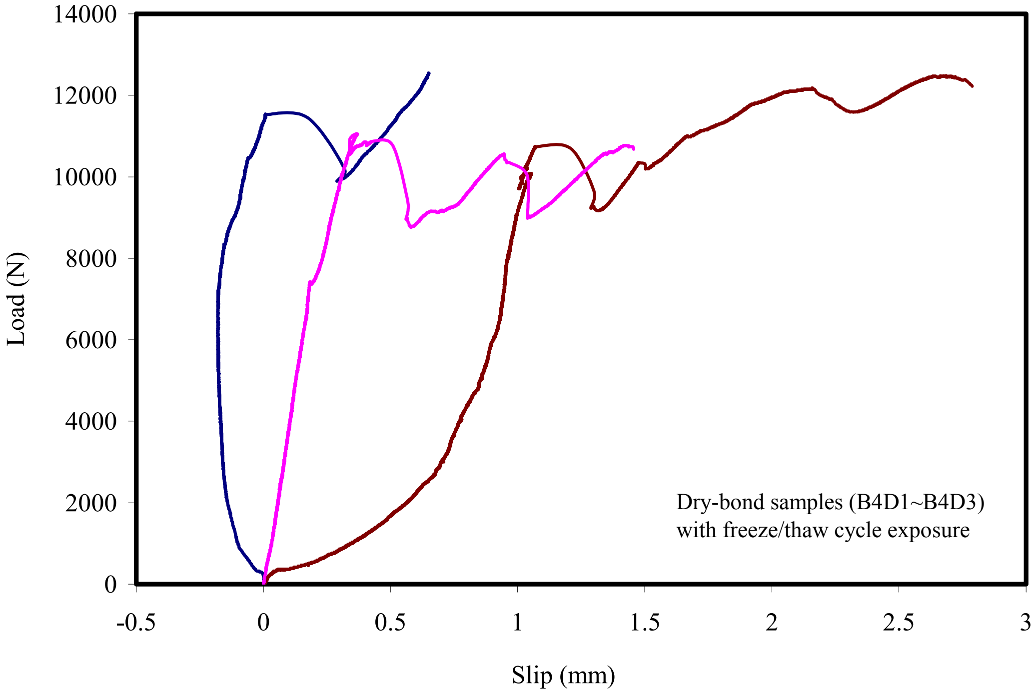

Fig.A.12: Load-slip relation of dry-bond with freeze/thaw cycle exposure (B4)

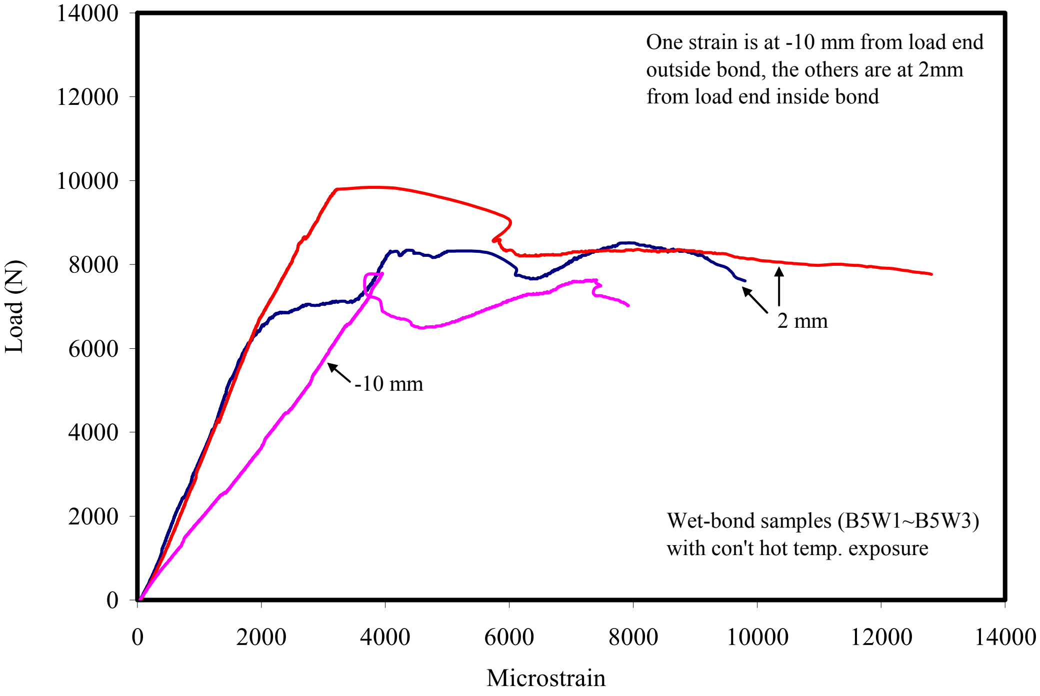

Fig.A.13: Load-strain relation of wet-bond with hot water exposure (B5)

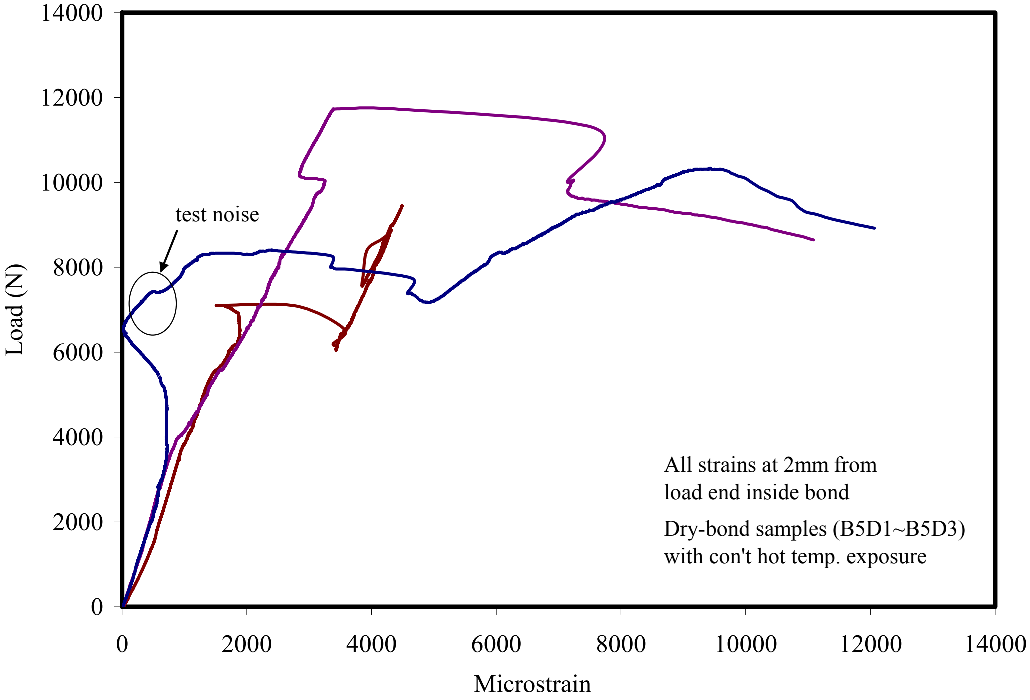

Fig.A.14: Load-strain relation of dry-bond for hot water exposure (B5)

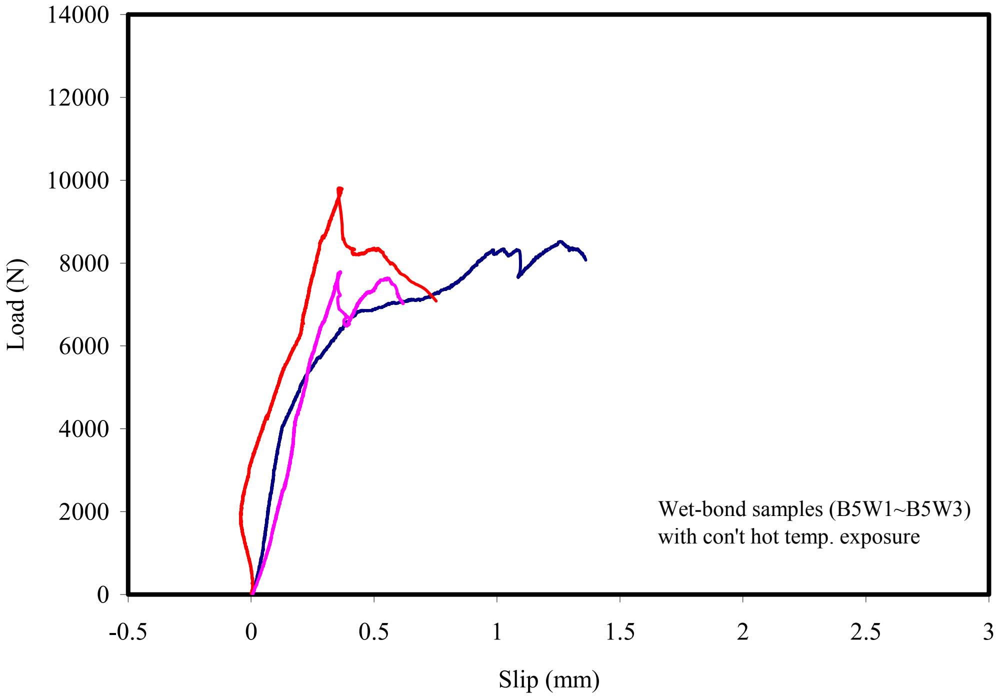

Fig.A.15: Load-slip relation of wet-bond with hot water exposure (B5)

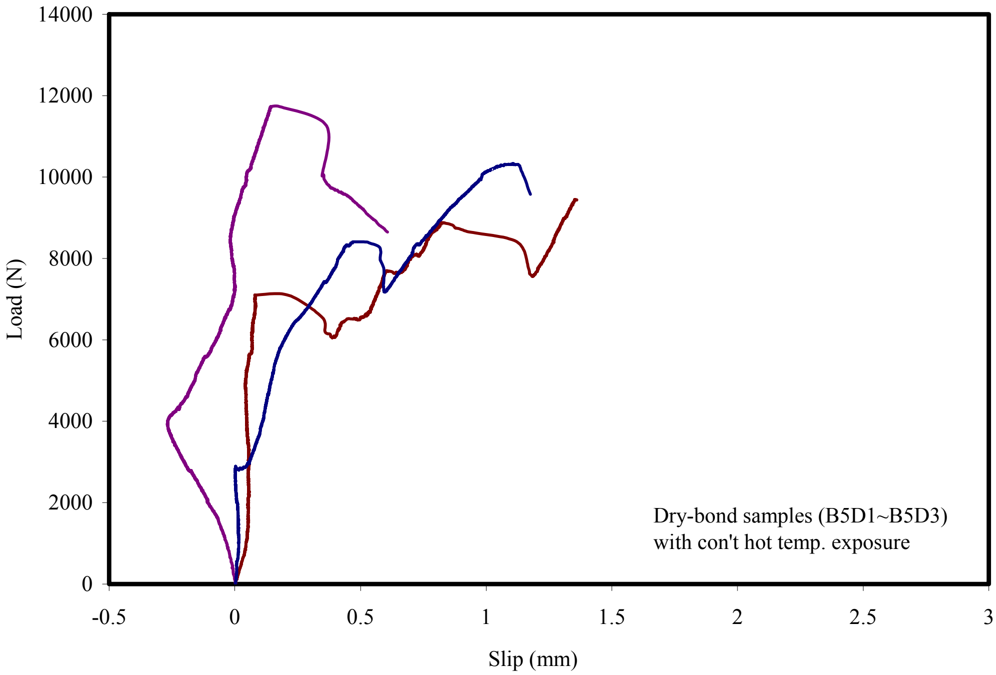

Fig.A.16: Load-slip relation of dry-bond with hot water exposure (B5)

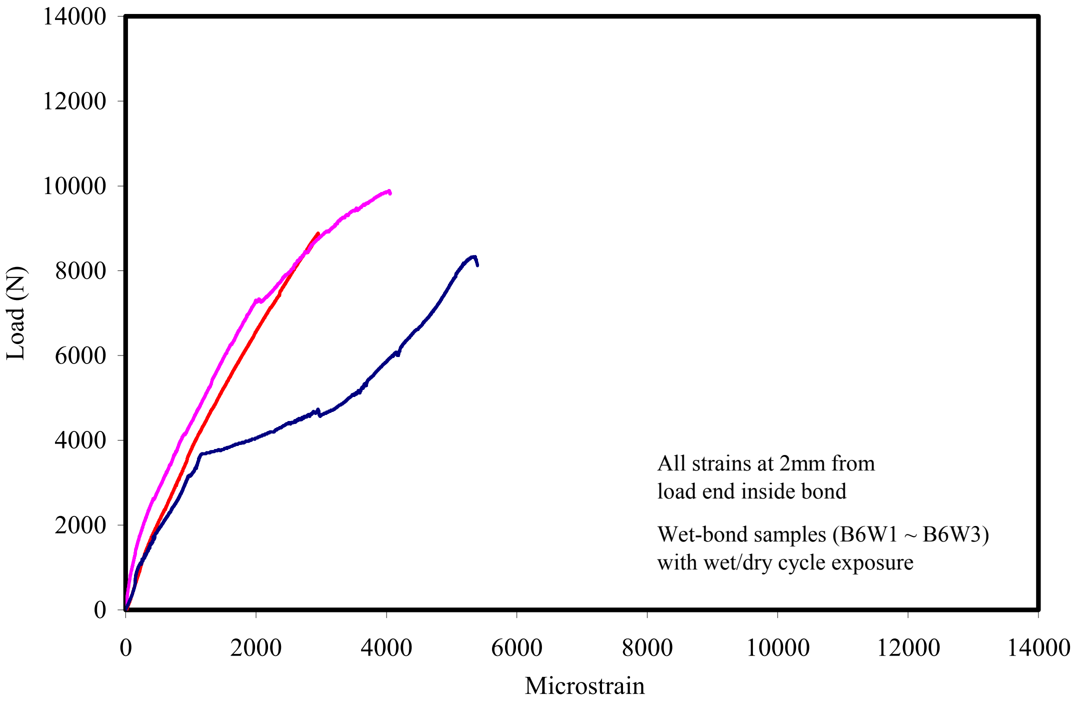

**Fig.A.17: Load-strain relation of wet-bond with wet/dry cycle exposure (B6)**

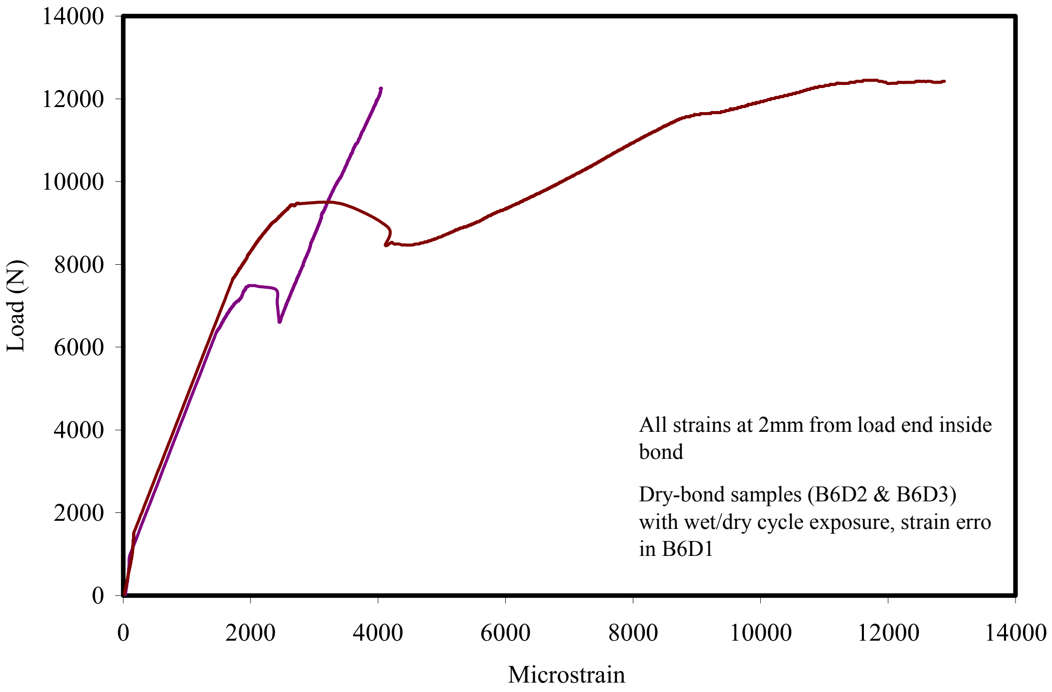

**Fig.A.18: Load-strain relation of dry-bond with wet/dry cycle exposure (B6)**

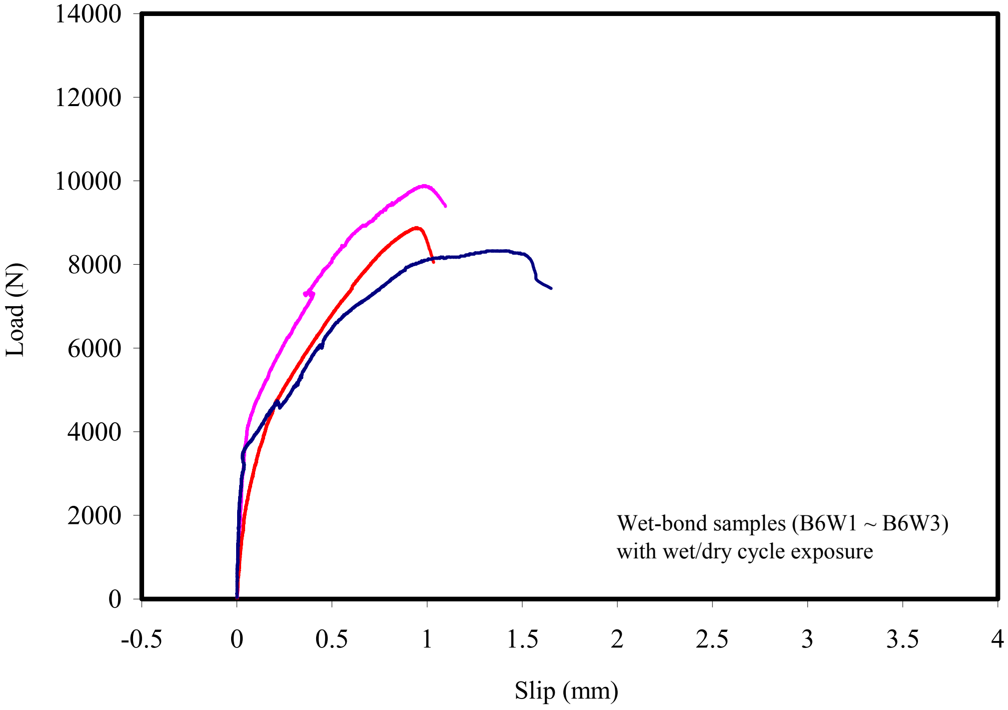

Fig.A.19: Load-slip relation of wet-bond with wet/dry cycle exposure (B6)

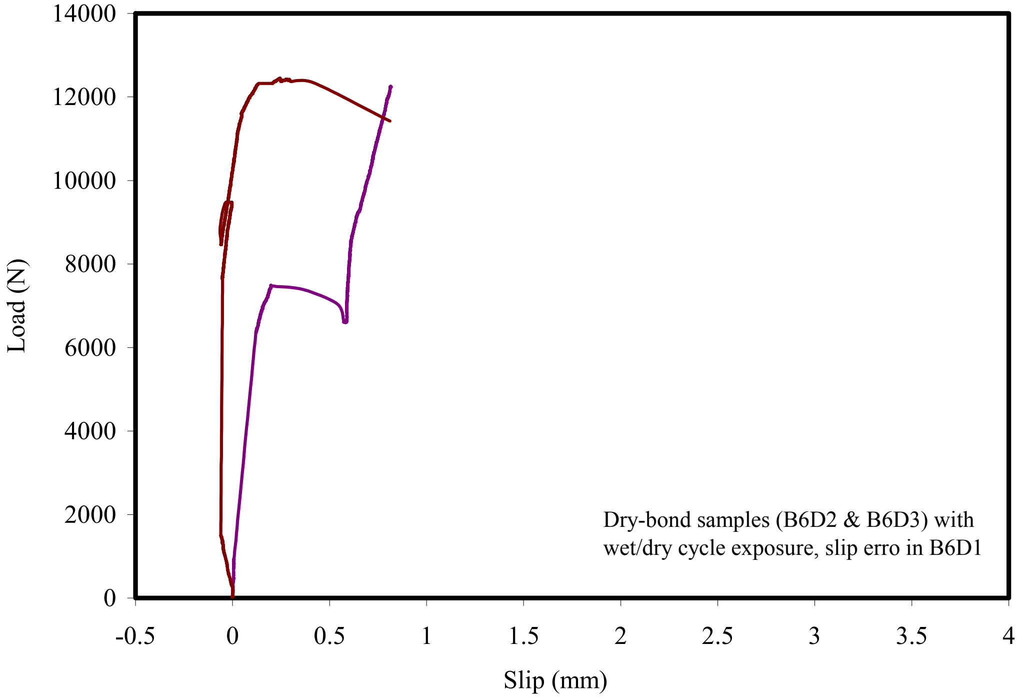

Fig.A.20: Load-slip relation of dry-bond for wet/dry cycle exposure group (B6)

# Appendix B: Equations' Derivation

## 1. Derivation of parameters M and N:

The relative slip between concrete and laminates is:

$$f_{frp}(x)/E_{frp}+f_{con}(x)/E_{con}=\frac{t_{adh}}{G_{adh}}\times\frac{d\tau(x)}{dx} \tag{5.17}$$

The bond stress is given in Equation 20 in chapter 5:

$$\tau(x)=M\cosh(\lambda x)+N\sinh(\lambda x) \tag{5.20}$$

**The boundary condition is:**

$$\text{at } x=0,\ \varepsilon_{frp}=\frac{P}{A_{frp}E_{frp}} \text{ and } \varepsilon_{con}=\frac{P}{A_{con}E_{con}}$$

$$\text{at } x=le,\qquad \varepsilon_{frp}=\varepsilon_{con}=0$$

Apply the boundary condition x =0 into Equation 5.17 get:

$$\frac{P}{A_{frp}E_{frp}}+\frac{P}{A_{con}E_{con}}=\frac{t_{adh}}{G_{adh}}\times\frac{d\tau(0)}{dx} \tag{B-1}$$

differentiate Equation 20, get:

$$\frac{d\tau(x)}{dx}=M\lambda\sinh(\lambda x)+N\lambda\cosh(\lambda x) \tag{B-2}$$

$$\text{at x = 0, } \frac{d\tau(0)}{dx}=N\lambda \tag{B-3}$$

substitute Eq. B-3 into Eq. B-1, get:

$$N=\frac{G_{adh}}{t_{adh}}\times(\frac{1}{A_{frp}E_{frp}}+\frac{1}{A_{con}E_{con}})\times\frac{P}{\lambda} \tag{B-4}$$

substitute Eq. 5.19 in chapter 5 into Eq. B-4, get N expressed as:

$$\lambda^2=\frac{G_{adh}}{t_{adh}}\cdot\frac{1}{t_{frp}E_{frp}}\cdot(1+\frac{E_{frp}A_{frp}}{E_{con}A_{con}}) \tag{5.19}$$

$$N = \frac{P}{b_l} \cdot \lambda \tag{B-5}$$

Apply boundary condition x = le and into Eq. 5.17 get:

$$\frac{d\tau(le)}{dx} = 0 \tag{B-6}$$

substitute Eq. B-6 into Eq. B-2, find M as:

$$M\lambda \sinh(\lambda x) + N\lambda \cosh(\lambda x) = 0$$

$$M = -N / \tanh(\lambda \cdot le) = -\frac{P \cdot \lambda}{b} / \tanh(\lambda \cdot le) \tag{B-7}$$

**2. Derivation of tensile stress of laminate**

From equilibrium of specimens:

$$\tau(x) = \frac{A_{frp}}{b} \cdot \frac{df_{frp}(x)}{dx} \tag{11}$$

Substituting M and N to Eq.11, get:

$$\frac{df_{frp}(x)}{dx} = \frac{P \cdot \lambda}{t_{frp} b} [-\frac{\cosh(\lambda x)}{\tanh(\lambda \cdot le)} + \sinh(\lambda x)] \tag{B-8}$$

Integrate Eq.B-8, get the tensile stress of laminate:

$$\begin{aligned} f_{frp}(x) &= \frac{P \cdot \lambda}{t_{frp} b} \int [-\frac{\cosh(\lambda x)}{\tanh(\lambda \cdot le)} + \sinh(\lambda x)] \\ &= \frac{P}{t_{frp} b} \frac{\sinh[\lambda(le - x)]}{\sinh(\lambda \cdot le)} \end{aligned} \tag{B-9}$$

**3. Derivation of interfacial fracture energy**

$$d\tau(x) = G_{adh} \times d\gamma(x) \tag{13}$$

$$ds = \lfloor \varepsilon_{frp}(x) + \varepsilon_{con}(x) \rfloor \times dx = t_{adh} \cdot d\gamma(x) \tag{16}$$

Based on Equation 13 and 16 in chapter 5, get:

$$ds = \frac{t_{adh}}{G_{adh}} \cdot d\tau(x) \tag{B-10}$$

Substitute Equations B-10 and 13 into Eq 28 in chapter 5, the interfacial energy is founded as:

$$G_f = \frac{t_{adh}}{G_{adh}} \int \tau(x) d\tau(x) \tag{B-11}$$

Because effective bond length is constant depending on material properties and the same to bond area is constant too. So, the interfacial fracture energy of a bond can take is relative its effective length:

Substitute Equations B-2 and B-10 into Eq B-11, the interfacial energy is founded as:

$$\begin{aligned} G_f &= \frac{t_{adh}}{G_{adh}} \int_0^{le} [M\cosh(\lambda x) + N\sinh(\lambda x)][M\lambda\sinh(\lambda x) + N\lambda\cosh(\lambda x)]dx \\ &= \frac{1}{4} \cdot \frac{t_{adh}}{G_{adh}} \int_0^{le} [(M^2 + N^2)\cosh(2\lambda x) + 2MN \cdot \sinh(2\lambda x)] \\ &= \frac{1}{2} \cdot \frac{t_{adh}}{G_{adh}} \cdot \left\{ (M^2 + N^2)\sin^2 h(\lambda \cdot le) + 2MN \cdot \sinh(\lambda le) \cdot \cosh(\lambda \cdot le) \right\} \end{aligned} \tag{B-12}$$

Substitute Equation B-5 and B-7 to replace M and N, get:

$$\begin{aligned} G_f &= \frac{1}{2} \cdot \frac{t_{adh}}{G_{adh}} \cdot \frac{P^2}{b^2} \cdot \lambda^2 \\ &= \frac{1}{2} \cdot \frac{P^2}{b^2 \cdot E_{frp} \cdot t_{frp}} \cdot (1 + \frac{E_{frp} A_{frp}}{E_{con} A_{con}}) \end{aligned} \tag{B-13}$$

# Appendix C: Analytical Samples

Following calculations are examples for different failure modes, all symbols and equations are the same as in chapter five, comparison of numerical analysis and typical experimental result is shown in Chapter Five.

**Table C.1 Material properties**

| $E_{ca}$ | $t_{ca}$ | $E_{gl}$ | $t_{gl}$ | $E_{ma}$ | $t_{ma}$ | $t_1$ | $t_2$ | $b_{frp}$ | $B_{con}$ | $E_{con}$ | fc' | $G_{adh}$ |
|---|---|---|---|---|---|---|---|---|---|---|---|---|
| MPa | mm | MPa | mm | MPa | mm | mm | mm | mm | mm | MPa | MPa | MPa |
| 540000 | 0.143 | 80000 | 0.118 | 3032 | 1.185 | 1.8 | 1.42 | 25 | 75 | 33373 | 55 | 3032 |

Find:

$$E_1 = E_{ca} \times \frac{t_{ca}}{t_1} + E_{gl} \times \frac{t_{gl}}{t_1} + E_{ma} \times \frac{t_{ma}}{t_1} = 65873.8\ MPa$$

$$E_2 = E_{gl} \times \frac{t_{gl}}{t_1} + E_{ma} \times \frac{t_{ma}}{t_1} = 28615.7\ MPa$$

$$le = \sqrt{\frac{E_{frp} t_{frp}}{\sqrt{f_{con}'}}} = \sqrt{\frac{65873.8 \times 1.8}{\sqrt{55}}} = 126.4\ mm$$

$$\beta_{frp} = \sqrt{\frac{2 - b_{frp} / b_{con}}{1 + b_{frp} / b_{con}}} = \sqrt{\frac{2 - 25/75}{1 + 25/75}} = 1.118\ ; \quad \beta_L = 1\ (L > L_e)$$

$$P_4 = P_u = 0.427 \beta_{frp} \beta_L \sqrt{f_c'} b_{frp} l_e = 0.427 \times 1.118 \times 1 \times \sqrt{55} \times 25 \times 126.4 = 11188\ N$$

$t_{adh}$ = 0.94 mm (dry-bond); $t_{adh}$ =1.71 mm (wet-bond)

$$\begin{aligned} \lambda^2 &= \frac{G_{adh}}{t_{adh}} \cdot \frac{1}{t_1 E_1} \cdot \left(1 + \frac{E_1 A_{frp}}{E_{con} A_{con}}\right) \\ &= \frac{3032}{0.94} \cdot \frac{1}{1.8 \times 65873.8} \cdot \left(1 + \frac{65873.8 \times 25 \times 1.8}{33373 \times 75 \times 75}\right) \Rightarrow \lambda = 0.164\ (dry - bond) \\ &= \frac{3032}{1.71} \cdot \frac{1}{1.8 \times 65873.8} \cdot \left(1 + \frac{65873.8 \times 25 \times 1.8}{33373 \times 75 \times 75}\right) \Rightarrow \lambda = 0.121\ (wet - bond) \end{aligned}$$

**1) Example for failure mode I (B2D2)**

(1) Linear elastic deformation to carbon fibre fracture (Eq. 5.1):

$$P_1 = t_1 \times b \times E_1 \times \varepsilon_{ca} = 1.8 \times 25 \times 65873 \times 4000 \times 10^{-6} = 11857\ N$$

(2). Strain of laminate at 2 mm from load end is (Eq. 5.26):

$$\begin{aligned}\varepsilon_{frp}{}^{1}(2mm) &= \frac{P_1}{b \cdot t_1 \cdot E_1} \cdot \frac{\sinh[\lambda(l_e - 2)]}{\sinh(\lambda l_e)} \\ &= \frac{11857}{25 \times 1.8 \times 65873} \cdot \frac{\sinh[0.164 \times (126-2)]}{\sinh(0.164 \times 126)} = 2884 \times 10^{-6}\end{aligned}$$

where: superscript of $\varepsilon_{frp}{}^{1}(2mm)$ refer to corresponding point number in schematic of failure Mode I

(3). Glass fibre elongation (Eq. 5.6):

$$\Delta\varepsilon_{gl} = \varepsilon_{ca} \cdot (\frac{t_1}{t_2} - \frac{E_2}{E_1}) = 4000 \times (\frac{1.8}{1.42} - \frac{28615.7}{65873.8}) = 3332 \times 10^{-6}$$

(4). After elongation, the strain of laminate at 2 mm point is:

$$\varepsilon_{frp}{}^{2}(2mm) = \varepsilon_{frp}{}^{1}(2mm) + \Delta\varepsilon_{gl} = 2884 + 3332 = 6216 \times 10^{-6}$$

(5). Strain of laminate at carbon crack point after elongation (Eq. 5.7):

$$\varepsilon_2 = \varepsilon_{ca} + \Delta\varepsilon_{gl} = 4000 + 3332 = 7332 \times 10^{-6}$$

(6). Load drop to $P_3$, $\varepsilon_2 = \varepsilon_3$ (Eq. 5.8):

$$P_3 = \varepsilon_2 \cdot E_2 \cdot t_2 \cdot b = 7332 \times 28615.7 \times 1.42 \times 25 \times 10^{-6} = 7449\,N$$

(7). Carbon fracture induces initial debonding, strain at 2 mm increase with reloading until ultimate debonding (Eq. 5.9):

$$\begin{aligned}\varepsilon_{frp}{}^{4}(2mm) &= (P_4 - P_3)/(E_2 \cdot t_2 \cdot b) + \varepsilon_{frp}{}^{2}(2mm) \\ &= (11188 - 7449)/(1.42 \times 25 \times 28616) + 6216 \\ &= 9897 \times 10^{-6}\end{aligned}$$

**2) Example for failure mode II (B4W3)**

(1). Experimental results show that initial debonding load is approximately 60% of peak load, carbon fibre fracture at:

$$P_d = 60\% \times P_4 = 60\% \times 11188 = 6713\ N$$

(2). Strain of laminate at point 2 mm from load end is (Eq.5.26):

$$\begin{aligned}\varepsilon_{frp}{}^{1}(2mm) &= \frac{P_d}{b \cdot t_1 \cdot E_1} \cdot \frac{\sinh[\lambda(l_e - 2)]}{\sinh(\lambda l_e)} \\ &= \frac{6713}{25 \times 1.8 \times 65873} \cdot \frac{\sinh[0.121 \times (126 - 2)]}{\sinh(0.121 \times 126)} = 1777 \times 10^{-6}\end{aligned}$$

(3). When carbon fibre fracture, debonded laminate at 2 mm deformed to ultimate strain of carbon fibre $\varepsilon_{frp}{}^{1}(2\text{ mm}) = \varepsilon_{ca} = 4000\times10^{-6}$, and the carbon fracture load is:

$$P_2 = t_1 \times b \times E_1 \times \varepsilon_{ca} = 1.8 \times 25 \times 65873 \times 4000 \times 10^{-6} = 11857\ N$$

(4). Elongation of glass fibre (Eq. 5.6 ):

$$\Delta\varepsilon_{gl} = \varepsilon_{ca} \cdot (\frac{t_1}{t_2} - \frac{E_2}{E_1}) = 4000 \times (\frac{1.8}{1.42} - \frac{28615.7}{65873.8}) = 3333 \times 10^{-6}$$

(5). The strain of laminate at 2 mm after glass elongation (Eq. 5.6):

$$\varepsilon_{frp}{}^{2}(2mm) = \varepsilon_2 = \varepsilon_{ca} + \Delta\varepsilon_{gl} = 4000 + 3333 = 7333 \times 10^{-6}$$

(6). Load drop to $P_3$ at $\varepsilon_2 = \varepsilon_3$ (Eq. 5.8) is:

$$P_3 = \varepsilon_2 \cdot E_2 \cdot t_2 \cdot b = 7333 \times 10^{-6} \times 28615.7 \times 1.42 \times 25 = 7449\,N$$

(7). Strain at 2 mm increase with reloading until ultimate debonding (Eq.5.9):

$$\begin{aligned}\varepsilon_{frp}{}^{4}(2mm) &= (P_4 - P_3)/(E_2 \cdot t_2 \cdot b) + \varepsilon_{frp}{}^{2}(2mm) \\ &= (11188 - 7449)/(1.42 \times 25 \times 28616) + 7333 \\ &= 11013 \times 10^{-6}\end{aligned}$$

**3) Example for failure mode III (B6W3)**

(1). Experimental results show that average peak load of mode III is around 10000 N

(Table 4.5), and the initial debonding load ratio is 55% (Table 5.2):

$P_4 = 10000$ N ; $P_d = 55\% \times P_4 = 5500\,N$

(2). Strain of laminate at point 2 mm is (Eq. 5.26):

$$\varepsilon_{frp}{}^{1}(2mm) = \frac{P_d}{b \cdot t_1 \cdot E_1} \cdot \frac{\sinh\left[\lambda(l_e - 2)\right]}{\sinh(\lambda l_e)}$$

$$= \frac{5500}{25 \times 1.8 \times 65873} \cdot \frac{\sinh[0.121 \times (126 - 2)]}{\sinh(0.121 \times 126)} = 1456 \times 10^{-6}$$

(2). When load increase to ultimate load, debonding propagate to free end and the strain at 2 mm point is:

$$\varepsilon_{frp}{}^{4}(2mm) = \frac{P_4}{b \cdot t_1 \cdot E_1} = \frac{10000}{25 \times 1.8 \times 65873} = 3373 \times 10^{-6}$$